

Université Mohamed Khider – Biskra
Faculté des Sciences et de la technologie
Département : Génie électrique.
Ref :.....



جامعة محمد خيضر بسكرة
كلية العلوم و التكنولوجيا
قسم: الهندسة الكهربائية
المرجع:.....

Thèse présentée en vue de l'obtention
Du diplôme de
Doctorat en sciences en : Electronique

Spécialité (Option) : Electronique

**Etude et simulation des propriétés électriques et optiques des
cellules solaires à base de Kësterites.**

Présentée par :
Siham MANSOURI

Soutenue publiquement le : 06/01/2025

Devant le jury composé de :

Pr. Saadoune Achour
Pr. Dehimi Lakhdar
Dr. Beddiaf Zaidi
Dr. Terghini Ouarda

Professeur
Professeur
M.C.A
M.C.A

Président
Rapporteur
Examineur
Examineur

Université de Biskra
Université de Batna 1
Université de Batna 1
Université de Biskra

University of Mohamed Khider Biskra

Faculty of Science and Technology

Departement : Electrical Engineering

Ref :.....



جامعة محمد خيضر بسكرة
كلية العلوم و التكنولوجيا
قسم: الهندسة الكهربائية
المرجع:.....

Thesis submitted in fulfillment of the requirements
for the degree of

Doctorate in Science in: Electronics

Specialty (Option): Electronics

Study and simulation of the electrical and optical properties of Kesterite-based solar cells.

Presented by:

Siham MANSOURI

Publicly supported on: January 06, 2025.

In front of the jury:

Pr. Saadoune Achour
Pr. Dehimi Lakhdar
Dr. Beddiaf Zaidi
Dr. Terghini Ouarda

Professor
Professor
M.C.A
M.C.A

President
Advisor
Examiner
Examiner

University of Biskra
University of Batna1
University of Batna 1
University of Biskra

Acknowledgements

In the name of Allah, the Most Merciful, the Most Compassionate. All praise belongs to Allah, Lord of the worlds, and may prayers and peace be upon Muhammad, His servant and messenger.

First and foremost, praise be to Allah, the Almighty, the Greatest of all, upon whom we ultimately depend for sustenance and guidance. I would like to sincerely thank Allah for giving me the opportunity, determination, and strength to complete my research. His continuous grace and mercy have been with me throughout my life, especially during the period of my research.

I would like to express my deepest gratitude to my advisor, Professor Lakhdar Dehimi, for his incredible patience and encouragement throughout my studies and research. His guidance has been invaluable to me during all phases of my research and the writing of this thesis. I could not have asked for a better advisor and mentor for my doctoral studies.

In addition to my advisor, I would like to thank the rest of my thesis committee: Professor Saadoune Achour, Professor Beddiaf Zaidi, and Dr. Terguini Ouarda for taking time out of their busy schedules to serve on my dissertation committee and provide their valuable input.

Last but not least, I would like to thank my family: my parents, my husband, and my brothers and sister for their spiritual support throughout the writing of this thesis and my life in general.

Abstract

$\text{Cu}_2\text{ZnSnS}_4$ (CZTS) is a quaternary semiconductor in thin film form with a direct band gap ranging from 1.4 to 1.6 eV and a high absorption coefficient of 10^4 cm^{-1} . This absorber film possesses highly beneficial properties and offers a low production cost.

This study investigates the potential enhancement of CZTS-based solar cells using the numerical simulation program SCAPS-1D by utilizing various hole transport layers (HTLs), namely MoOx, CuI, and SnS. Key cell parameters such as CZTS absorber layer thickness, defect density, and acceptor concentration are optimized to increase photon energy absorption and reduce recombination rates. Our findings highlight the exceptional performance of MoOx and CuI as HTLs, achieving a power conversion efficiency of 23.73% and a fill factor of 88%, closely approaching the theoretical limits proposed by Shockley-Queisser. This strategy of tuning band alignment and optimizing global parameters holds promise for enhancing the efficiency of CZTS hetero-junction based solar cells, ushering in a more sustainable era of solar energy conversion.

Additionally, the study examines the structural and electrical characteristics of a Schottky junction composed of an aluminum (Al) electrode, a p-type copper zinc tin sulfide (CZTS) thin film, and a molybdenum (Mo) substrate. Structural characterization was conducted using SEM analysis and EDX spectra, while electrical characterization involved analyzing the current-voltage (I-V) characteristics. The study validates the obtained CZTS solar cell parameters by simulating the I-V characteristic using extracted parameters and comparing them to experimental data. The comparative analysis of experimental and fitted I-V characteristics demonstrates the effectiveness of the GA and Newton Raphson method in parameter extraction. These findings contribute to a broader understanding of solar cell parameter optimization and offer a robust methodology for future applications in the field.

Keywords: CZTS solar cell; HTL candidates; Recombination mechanisms; Optimization; I-V characteristic; Schottky diode; Parameters extraction.

المخلص

(CZTS) $\text{Cu}_2\text{ZnSnS}_4$ هو من أشباه الموصلات رباعية العناصر على شكل فيلم رقيق مع فجوة نطاق مباشرة تتراوح من 1.4 إلى 1.6 eV و معامل امتصاص عالٍ يبلغ 10^4 cm^{-1} . يتميز هذا الفيلم الماص بخصائص مفيدة للغاية ويوفر تكلفة إنتاج منخفضة.

تهدف هذه الدراسة إلى تحسين كفاءة الخلايا الشمسية المعتمدة على مادة CZTS باستخدام برنامج المحاكاة العددية SCAPS-1D، وذلك من خلال دمج طبقات نقل الثغوب (HTLs) المختلفة مثل MoOx ، CuI و SnS . يتم تحسين المعلمات الرئيسية للخلايا مثل سمك الطبقة الماصة CZTS، كثافة العيوب، وتركيز الحاملات لزيادة امتصاص طاقة الفوتونات وتقليل معدلات إعادة التركيب. تبرز نتائج الأداء الاستثنائي لطبقتي MoOx و CuI ك HTLs، حيث تحقق كفاءة تحويل طاقة تصل إلى 23.73% وعامل ملء بنسبة 88%، مقتربة بذلك من الحدود النظرية المقترحة بواسطة نموذج Shockley-Queisser. تحمل هذه الاستراتيجية لضبط توافق النطاق وتحسين المعلمات الإجمالية وعوداً بزيادة كفاءة الخلايا الشمسية المعتمدة على الوصلة غير المتجانسة CZTS، مما يمهد الطريق لعصر أكثر استدامة في تحويل الطاقة الشمسية.

بالإضافة إلى ذلك، تعالج الدراسة الخصائص الهيكلية والكهربائية لوصلة شوتكي تتكون من قطب ألومنيوم (Al)، وفيلم رقيق من النحاس والزنك والكبريت (CZTS) من النوع p، وركيزة من الموليبيدينوم (Mo). تم إجراء التوصيف الهيكلي باستخدام تحليل SEM وEDX، بينما شمل التوصيف الكهربائي تحليل خصائص التيار-الجهد (I-V). تتحقق الدراسة من معلمات الخلية الشمسية CZTS التي تم الحصول عليها عن طريق محاكاة خصائص التيار-الجهد باستخدام المعلمات المستخرجة، ومقارنتها بالبيانات التجريبية. يوضح التحليل المقارن للخصائص التجريبية والمحاكاة لتيار-الجهد فعالية طريقتي GA ونيوتن رافسون في استخراج المعلمات. تساهم هذه النتائج في فهم أعمق لتحسين معلمات الخلايا الشمسية وتقديم منهجية قوية لتطبيقات المستقبل في هذا المجال.

الكلمات المفتاحية: الخلية الشمسية CZTS؛ مرشح HTL؛ آليات إعادة التركيب؛ التحسين؛ الخصائص I-V؛ ديود شوتكي؛ استخراج المعلمات.

Résumé

Le $\text{Cu}_2\text{ZnSnS}_4$ (CZTS) est un semi-conducteur quaternaire sous forme de film mince avec une bande interdite directe allant de 1,4 à 1,6 eV et un coefficient d'absorption élevé de 10^4 cm^{-1} . Ce film absorbeur possède des propriétés très avantageuses et offre un coût de production faible.

Cette étude examine le potentiel d'amélioration des cellules solaires à base de CZTS en utilisant le programme de simulation numérique SCAPS-1D avec différentes couches de transport de trous (HTLs), à savoir MoOx, CuI et SnS. Les paramètres clés des cellules tels que l'épaisseur de la couche absorbeur CZTS, la densité de défauts et la concentration d'accepteurs sont optimisés pour augmenter l'absorption de l'énergie photonique et réduire les taux de recombinaison. Nos résultats mettent en évidence les performances exceptionnelles de MoOx et CuI en tant que HTLs, atteignant un rendement de conversion de puissance de 23,73% et un facteur de remplissage de 88%, se rapprochant des limites théoriques proposées par Shockley-Queisser. Cette stratégie d'ajustement de l'alignement des bandes et d'optimisation des paramètres globaux promet d'améliorer l'efficacité des cellules solaires hétérojonction à base de CZTS, ouvrant la voie à une ère plus durable de conversion d'énergie solaire.

De plus, l'étude examine les caractéristiques structurelles et électriques d'une jonction Schottky composée d'une électrode en aluminium (Al), d'un film mince de cuivre-zinc-étain-sulfure (CZTS) de type p et d'un substrat de molybdène (Mo). La caractérisation structurelle a été réalisée à l'aide d'une analyse SEM et des spectres EDX, tandis que la caractérisation électrique a impliqué l'analyse des caractéristiques courant-tension (I-V). L'étude valide les paramètres des cellules solaires CZTS obtenus en simulant les caractéristiques I-V à l'aide des paramètres extraits et en les comparant aux données expérimentales. L'analyse comparative des caractéristiques expérimentales et ajustées I-V démontre l'efficacité de la méthode GA et l'algorithme de Newton Raphson dans l'extraction des paramètres. Ces résultats contribuent à une compréhension plus large de l'optimisation des paramètres des cellules solaires et offrent une méthodologie robuste pour les applications futures dans le domaine.

Mots-clés : cellule solaire CZTS ; candidats HTL ; mécanismes de recombinaison ; optimisation ; caractéristique I-V ; diode Schottky ; extraction des paramètres.

Table of Contents	page
Abstract	I
ملخص.....	II
Résumé.....	III
Table of Contents.....	IV
List of figures.....	VII
List of tables.....	X
General Introduction	1
References	5
 Chapter 1: Photovoltaic energy and thin film solar cells 	
1.1 Introduction	6
1.2. Physics of Photovoltaic.....	6
1.2.1. Photovoltaic effect.....	6
1.2.2. Solar radiation	7
1.2.3. Principle of working of a photovoltaic cell	8
1.2.4. Physics of p–n junction.....	11
1.2.5. Equivalent circuit of photovoltaic cell.....	12
1.2.6. Photovoltaic Cell Parameters	14
1.2.6.1. Short-circuit current density J_{sc}	15
1.2.6.2. Open-circuit voltage V_{oc}	15
1.2.6.3. Fill Factor FF	16
1.2.6.4. Power Conversion Efficiency PCE.....	16
1.2.7. Generation and Recombination	16
1.2.8 Minority Carrier Lifetime.....	18
1.2.9. Energy Band alignment.....	19
1.3. Photovoltaic cell technologies.....	21
1.3.1 First Generation solar cells.....	22
1.3.2. Second Generation solar cells.....	22
1.3.3. Third Generation solar cells	24
1.4. Advantages, Challenges, and Potential Solutions.....	25
1.5.1. Advantages	25
1.5.2 Challenges.....	26
1.5.3 Potential Solutions.....	27
1.6. Conclusion	27
References.....	28
 Chapter 2: Literature review of CZTS based solar cells 	
2.1 Introduction.....	29
2.2. Advancements in kesterite Solar Cell Technology.....	29
2.3. Properties of CZTS.....	30
2.3.1 The structure of CZTS.....	31

2.3.2 Phases of CZTS.....	32
2.3.3 CZTS Defects.....	34
2.3.4 Band Gap energy.....	38
2.4. Deposition Techniques for CZTS.....	39
2.4.1 Vacuum-based approaches.....	40
2.4.1.1 Evaporation techniques.....	40
2.4.1.2 The Pulsed laser deposition technique (PLD).....	40
2.4.1.3 Sputtering techniques.....	41
2.4.2 Non-vacuum-based approaches.....	42
2.4.2.1 Spray pyrolysis techniques.....	42
2.4.2.2 Electrochemical deposition techniques.....	42
2.4.2.3 Sol–gel deposition technique.....	43
2.5 Design of CZTS solar cell.....	44
2.5.1 Anti-reflecting layer.....	46
2.5.2 The Window layer.....	46
2.5.3 The Buffer layer.....	47
2.5.4. Back contact.....	51
2.6 Interface Buffer /Absorber layer.....	51
2.7 Future perspective of the CZTS solar cell.....	53
2.8 Conclusion.....	53
References.....	54
Chapter 3 : Numerical Modeling by SCAPS 1-D	
3.1. Introduction.....	60
3.2 Basic Equations	61
3.3 SCAPS-1D.....	64
3.3.1 Parameters.....	65
3.3.2 SCAPS-1D front and interface.....	66
3.4. Solar Cell Definition.....	67
3.4.1. Editing a Solar Cell Structure.....	67
3.4.2. Adding device structure layers	68
3.4.3. Contact.....	69
3.4.4. Defects and Recombination.....	70
3.4.5. Interfaces.....	72
3.5.1 Conclusion	73
References	74
Chapter 4: Performances of CZTS TFSC using different HTLs Layer	
4.1 Introduction.....	75
4.2. Modeling framework.....	77
4.2.1 Solar cell structure.....	77
4.2.2. Modeling framework and Material Parameters.....	78

4.3. Results and discussion.....	82
4.3.1 Prediction capabilities of the simulation setup.....	82
4.3.2 Optimization of conventional solar cell.....	83
4.3.2.1 Exploring the Impact of MoS ₂ Thickness and CZTS on Conventional Solar Cell Properties.....	83
4.3.2.2 Effect of CZTS and MoS ₂ Acceptor density on the conventional solar cell characteristics.....	84
4.3.2.3 Impacts of bulk defect density of absorber on PV performances.....	85
4.3.2.4 Impacts of Back contact work function and Temperature on solar cell performances.....	86
4.3.2.5 Impacts of series resistance on cell performances.....	88
4.3.3 HTL candidates' examination.....	89
4.4. Conclusion.....	93
References.....	94
Chapter 5:	
Structural and Electrical Features: A Comparative Parameter Extraction Study of Al/p-CZTS Thin Film Schottky Diodes.	
5. 1. Introduction.....	99
5.2. Experimental setup.....	100
5.3. Structural and electrical properties.....	101
5.3.1. Analysis of CZTS thin film surface morphology.....	101
5.3.2. Elemental analysis of CZTS thin film.....	102
5.3.3. Current–voltage (I–V) characteristics.....	103
5.4. Modeling framework	104
5.4.1. Mathematical model of SBD	105
5.4.2. Objective function of parameter extraction problem	106
5.4.3. Determining the initial parameters values	107
5.5. Results and discussion.....	108
5.5.1. Newton–Raphson method.....	108
5.5.2. Curve fitting models of solar cell characteristics	109
5.5.2.1. Determination of the initials value of η , R_s and I_s	110
5.5.2.2. Determination of R_{sh}	111
5.5.3. Genetic algorithm.....	113
5.6. Comparison between Newton–Raphson method (NRM) and genetic algorithm (GA)method.....	116
5.4. Conclusion.....	119
References.....	120
General Conclusion	123
Appendix A: Genetic Algorithm.....	125
Appendix B: Newton Raphson Method.....	130

<i>List of figures</i>	page
<i>Chapter 1: Overview of Principle Physics of Solar Cells</i>	
Figure.1.1: Solar cell device for transforming solar energy into electricity.....	1
Figure 1.2: Solar irradiance spectrum above atmosphere and at Earth surface.....	8
Figure 1.3: Charge carrier generation by absorption of photons.....	9
Figure 1.4: Simple solar cell model.....	10
Figure 1.5: p–n junction in thermal equilibrium with zero-bias voltage applied.....	11
Figure 1.6: Ideal photovoltaic cell.....	12
Figure 1.7: Photovoltaic cell equivalent circuit.....	13
Figure 1.8: The influence of the series resistance and shunt resistance on the current-voltage (I-V) behavior of the solar cell.....	14
Figure. 1.9: Typical dark and light solar cell current density-voltage characteristics.....	15
Figure I.10: Generation and types of recombination processes.....	18
Figure 1.11: Band structure of a hetero-junction.....	20
Figure 1.12: Two types of barriers: (a) spike-like barrier and (b) cliff-like barrier.....	20
Figure. 1.13: An analysis of the historical, present, and future state of photovoltaic technology.....	21
Figure 1.14: The manufacturing process for standard commercial crystalline silicon solar cells.....	22
Figure 1.15: Thin film Photovoltaic Cell.....	23
Figure 1.16: Organic Photovoltaic Cell "Helia Film".....	24
<i>Chapter 2: Literature review of CZTS based solar cells</i>	
Figure 2.1: Evolution of the number of publications and citations per year for CZTS material till October 2023; search for “Cu ₂ ZnSnS ₄ (CZTS) solar cells”.....	30
Figure 2.2 : a Kesterite, b Stannite and c PMCA structure of the CZTS material based on the different alternating planes.....	32
Figure 2.3: Secondary phase generation in the CZTS material.....	33
Figure 2.4: CZTS quaternary phase diagram containing the known phases.....	33
Figure 2.5: Different levels of defects present in both CIGS and CZTS materials.....	35
Figure 2.6: The energy levels at which intrinsic point defects arise in the band gaps of CZTS.....	36
Figure 2.7: Different defect complexes change CZTS's valence (green) and conduction (blue) bands.....	37
Figure 2.8: a) Typical band-gap and (b) Absorption coefficients of a CZTS thin film.....	39
Figure 2.9: General structure of single-junction thin-Film CZTS solar Cell.....	45
Figure 2.10: Transportation of electrons and holes in thin-film solar cells constructed from CZTS.....	45
Figure 2.11: CZTS thin-film solar cells use Zinc Oxide's crystal structure as a resistive layer.....	47
Figure 2.12: Band-to-band comparison of ZnS and CdS, the best communal buffer layer	

materials, with CZTS.....	49
Figure.2.13 I-V characteristics of simulated CZTS solar cells with varying absorber layer thicknesses.....	50
Figure 2.14: Efficiency analysis of the simulated thin-film CZTS solar cell, considering both external and internal factors.....	50
Figure 2.15: Band alignment of buffer layer in CZTS solar cells compared with and without a spike-like structure in junction CdS/CZTSSe.....	52
Chapter 3: Numerical Modeling by SCAPS 1-D	
Figure 3.1: SCAPS working procedure.....	64
Figure 3.2: SCAPS startup panel: Action panel or main panel.....	66
Figure 3.3: Defining a solar cell structure.....	67
Figure 3.4: Layer properties panel.....	68
Figure 3.5: Contact properties panel.....	70
Figure 3.6: Recombination model and defects.....	71
Figure 3.7: The defect properties panel.....	72
Figure 3.8: Interface defects panel.....	73
Chapter 4: Performances of CZTS TFSC using different HTLs Layer	
Figure 4.1: Schematic view of typical CZTS structures (a) conventional cell (b) proposed cell.....	77
Figure 4.2: Absorption coefficients of different layers.....	78
Figure 4.3: A comparison between simulated and real typical solar cells.....	82
Figure 4.4: PV performance parameters depend on the thickness of MoS ₂ and CZTS layers.....	83
Figure 4.5: The acceptor density of the MoS ₂ layer and CZTS absorber determines the PV performance characteristics.....	85
Figure 4.6: Impact of absorber defect density on the suggested CZTS solar cell's efficiency using HTL.....	86
Figure 4.7: Influence of Back Contact Work Function on the Photovoltaic Performance Metrics of CZTS Solar Cells.....	87
Figure 4.8: Impact of operation temperature on the suggested CZTS solar cell's PV performance characteristics.....	88
Figure 4.9: Impact of series resistance on the suggested CZTS solar cell's PV performance metrics.....	89
Figure 4.10: Electric field variation throughout the structure with and without HTL.....	90
Figure 4.11: Simulated J-V characteristics of CZTS solar cells with different HTL candidates.....	91
Figure 12: Band diagram energy of CZTS solar cells of conventional and proposed cells...	92

Chapter 5: Structural and Electrical Features: A Comparative Parameter Extraction Study of Al/p-CZTS Thin Film Schottky Diodes.	
Figure 5.1: Al/p-CZTS/Mo Schottky barrier diode schematic cross section.....	101
Figure 5.2: SEM surface images of precursor CZTS film	102
Figure 5.3: Energy-Dispersive X-ray Spectra of precursor CZTS film.....	103
Figure 5.4: Room-temperature current–voltage characteristics in forward and reverse bias of the fabricated Al/p-CZTS/Mo Schottky junctions.....	104
Figure 5.5: Schottky barrier diode parameters extraction architecture.....	105
Figure 5.6: Flowchart of proposed algorithm for <i>SBD</i> Parameters estimation.....	106
Figure 5.7 (a) Characteristic $V = f(I)$, equation (5.22), (b) experimental solar cell $I-V$ characteristic and fitted curve in the direct polarization region 0.2 V – 1 V.....	111
Figure 5.8: (a) $I = f(V)$, equation (5.22), (b) $I = f(V)$ of Figure 5.4.....	112
Figure 5.9: $I = f(V)$, equation 5.3.....	113
Figure 5.10: Flowchart of GA approach.....	115
Figure 5.11: (a) Evolution of the objective function as function of the evolving generations, (b) Comparison of experimental and fitted $I-V$ characteristics.....	117
Figure 5.12: $I-V$ characteristics comparisons between the experimental data and the predicted by <i>NRM</i> and <i>GA</i>	118

List of tables	page
Chapter 2: Literature review of CZTS based solar cells	
Table 2.1: Different properties of secondary phases detected in CZTS materials	33
Table 2.2: Possible CZTS defects/complexes defects.....	38
Table 2.3: Band gap of CZTS/CZTSe simulated and measured experimentally.....	39
Table 2.4: The efficiencies achieved by CZTS materials using various preparation methods...	44
Table 2.5: Possible buffer layer materials that can be utilized taking into account their band gap	48
Table 2.6: Efficiency attained employing diverse buffer layers in CZTS solar cell.....	51
Chapter 4: Performances of CZTS TFSC using different HTLs Layer	
Table 4.1: Back and front contact parameters.....	80
Table 4.2: Materials parameters used in the simulation	81
Table 4.3: Electrical properties of different HTL layers in solar cells	81
Table 4.4: Defect parameters are used at different interfaces.....	81
Table 4.5: Comparison of characteristics features between the experimental data [22] and our simulation results.....	83
Table 4.6: Output parameters of various CZTS solar cell structures.....	92
Chapter 5: Structural and Electrical Features: A Comparative Parameter Extraction Study of Al/p-CZTS Thin Film Schottky Diodes	
Table 5.1: Weight and atomic composition of CZTS thin film.....	103
Table 5.2: Configuration parameters used for GA approach	116
Table 5.3: Parameters extracted using the GA method with experimental data.....	116
Table 5.4: Initial parameters value for the Newton–Raphson and GA.....	117
Table 5.5: Results of Schottky diode parameters obtained by Newton–Raphson and GA techniques.....	118
Table 5.6: Advantages and limitations of different competitive extraction methods	119

List of symbols and abbreviations

2D	Two-Dimensional
AM0	Air Mass zero
AM1.5	Air Mass 1.5 Global solar spectrum
CB	Conduction band
CBM	Minimum conduction band
CBO	The conduction band Offset
D_n [cm^2/s]	Electron diffusion constant
D_p [cm^2/s]	Hole diffusion constant
E [V/cm]	Electric field
E_A, E_a [eV]	apparent activation energy
E_C [eV]	Bottom edge of conduction band
E_{CBM}	Minimum conduction band, the bottom of the conduction bands
E_F [eV]	(Equilibrium) Fermi level
E_{Fn} [eV]	Electron Fermi level
E_{Fp} [eV]	Hole Fermi level
E_g (eV)	Gap optique
E_T [eV]	Trap level; energy level of a defect
E_{vac}	The vacuum level, free electron energy
f [Hz]	Frequency
FF [%]	Fill factor
G_n	The electron generation rates
G_p	The hole generation rates
$h\nu$ [J or eV]	Photon energy
I	Current
I_{ph}	Photogenerated current
J	Current density
J [A/cm^2]	Current density
J_0 [A/cm^2]	(Dark) saturation current density
J_m [A/cm^2]	Current density at maximum power
J_n [A/cm^2]	Electron particle current density
J_p [A/cm^2]	Hole particle current density

J_{sc} [A/cm ²]	Short circuit current density
HTL	Hole transport layer
KB	Boltzmann constant
L_e	The minority-carrier-diffusion lengths for electron
L_h	The minority-carrier-diffusion lengths for hole
n	Electron concentrations
N_A [1/cm ³]	Shallow acceptor density
N_C [cm ⁻³]	Densité effective d'états dans la bande de conduction
N_D [1/cm ³]	Shallow donor density
N_D^+ [cm ⁻³]	Density of ionized shallow donors
N_t, N_T [cm ⁻³]	Density of traps, defects
N_V [cm ⁻³]	Densité effective d'états dans la bande de valence
P	Hole concentrations
P_i	Incident power
P_m	Maximum produced power
PCE	Power conversion efficiency
q	Elementary charge
QE [%]	External quantum efficiency
R_n	The electron recombination rates
R_p	The hole recombination rates
R_s [Ω]	Series resistance
R_{sh} [Ω]	Shunt resistance
SRH	Shockley-Read-Hall recombination mechanism
T [K]	Absolute temperature
TCO	Transparent Conducting Oxide
V [V]	Voltage, applied voltage
VB	Valence band
VBM	Valence-band minimum
V_m [V]	Voltage at maximum power
V_{oc} [V]	Open circuit voltage
W [cm, μm or nm]	Depletion layer width
α [1/cm]	Optical absorption constant
ϵ	Relative permittivity
ϵ_0	[F/cm] Permittivity of vacuum

η [%]	Photovoltaic conversion efficiency
λ [nm] or [μm]	Wavelength
μ_n [cm^2/Vs]	Electron mobility
μ_p [cm^2/Vs]	Hole mobility
ρ [$\Omega\cdot\text{cm}$]	Résistivité
ρ_n	Electrons distribution
ρ_p	Holes distribution
σ [$\Omega^{-1}\cdot\text{cm}^{-1}$]	Conductivité, inverse de la résistivité
σ_n [cm^2]	Capture cross section for electrons
σ_p [cm^2]	Capture cross section for holes
ψ	Electrostatic potential
Φ	The flat band metal work function

General Introduction

Commercial applications frequently utilize semiconductor devices, such as those used in photovoltaic power generation. These devices convert sunlight into electricity and can be made from both elemental and compound materials, which may be non-crystalline or crystalline [1]. Crystalline materials typically offer higher conversion efficiency compared to polycrystalline and microcrystalline materials, but their production costs are also higher. Recent research has focused on enhancing efficiency while reducing costs, addressing the issues of low reliability and structural stability. Consequently, production research has significantly increased in recent years [2].

Currently, thin film technology is fully explored and commercialized as a cost-effective and economical way to produce solar cells. Interest in renewable energy sources has surged over the years, with solar energy—abundantly available in nature—being a prominent example [3]. The high demand for energy has led to the widespread use of solar devices. Alongside the sharp decline in organic fuel reserves, which contribute to atmospheric carbon dioxide and climate disruption, the demand for solar devices has risen [4]. The goal is to meet consumer electricity needs and produce high-efficiency solar cells cost-effectively without damaging the materials or photovoltaic cells [5].

The extended production potential of silicon-based thin-film photovoltaic cells has led to their increased demand. Various manufacturing processes have been employed for the production of these cells, including sputtering, evaporation, molecular beam epitaxy, e-beam evaporation, close space sublimation, and metal-organic chemical vapor deposition. However, these techniques are expensive due to the costs of materials, technology, and energy consumption.

Chalcopyrite solar cells are promising light-to-energy devices due to their high conversion efficiency, excellent electrical and optical properties, and high absorption coefficient, making them suitable candidates for commercial production. Significant efforts have been made over the years to improve the performance of CIGS and CdTe based devices. However, the high costs and toxicity of cadmium (Cd)-based CdTe absorbers and the scarcity of tellurium (Te), gallium (Ga), and indium (In) have limited their commercial expansion. Toxicity concerns hinder the development of solar cells, while the scarcity of materials like indium and gallium leads to higher manufacturing costs, restricting commercial production.

Quaternary compounds, abundant on Earth, show great potential as semiconductor materials due to their kesterite and stannite structures, specifically CZTS/Se and CFTS/Se. Copper zinc tin sulfide (CZTS), a naturally occurring absorber material, has a direct band gap of 1.4 to 1.6 eV, a high light absorption coefficient exceeding 10^4 cm^{-1} , cost-effective manufacturing methods, and consistent operational effectiveness [6-12]. These attributes make CZTS an attractive candidate for large-scale production of thin-film solar cells (TFSCs).

Experimental CZTS solar cells have achieved an efficiency of 6.7%, and another study reported 8.4% efficiency for TFSCs with a CZTS absorber derived from naturally available materials [13]. A $\text{Zn}_{1-x}\text{Cd}_x\text{S}$ buffer layer added to CZTS solar cells produced an attractive power conversion efficiency of 9.2% under functional resistivity conditions [13]. More specifically, the most complex hetero-junction device design, $\text{Mo}/\text{MoS}_2/\text{CZTS}/\text{CdS}/\text{ZnO}/\text{ITO}/\text{MgF}_2$, has a power conversion efficiency of nearly 11%, with an open-circuit voltage around 0.73V [14]. However, further research is needed as CZTS solar cells' efficiency is only slightly superior to that of existing thin-film sol-gel cells.

The purpose of this research is to maximize the photovoltaic conversion efficiency of CZTS-based solar devices for solar energy applications by integrating a hole transport layer (HTL) to boost carrier collection efficiency and reduce recombination at the rear-contact surface. Novel techniques for utilizing CuI, MoO_x , and SnS as HTL candidates in structures with CZTS are CuI/CZTS, MoO_x/CZTS , and SnS/CZTS. These configurations are evaluated using SCAPS-1D simulations to assess critical electrical parameters, addressing a significant gap in CZTS solar cell research.

Additionally, this work explores the use of Mo/CZTS/Al-based Schottky diodes to evaluate the CZTS absorption layer, emphasizing the extraction of electrical parameters such as saturation current, ideality factor, series, and shunt resistance through numerical methods like the Newton-Raphson method and genetic algorithm. These methods offer more accuracy and efficiency compared to traditional analytical methods, using curve fitting algorithms to better match experimental and theoretical models. This comprehensive approach not only optimizes solar cell parameters but also enhances the understanding of device behavior under various conditions.

The thesis is organized as follows:

The first chapter explains semiconductor theory, introduces pn-junctions, diode current equations, solar cell physics, and losses in a solar cell. It discusses solar cell technology,

generations of solar cells, different types of solar cells, thin-film solar cells, and the historical development of solar cells. It also covers fundamental parameters and methods used for electrical characterization and conclude with a discussion on advantages, challenges, and potential solutions.

The second chapter provides an overview of the development, fabrication methods, design, defects in CZTS material, and its potential use as a photovoltaic cell.

The third chapter presents the fundamental principles of numerical simulation and the use of SCAPS.

The fourth chapter examines the possible improvement of CZTS-based solar cells using different hole transport layers (HTLs) such as MoO_x, CuI, and SnS through numerical modeling. It enhances crucial cell characteristics, including the thickness of the CZTS absorber layer, defect density, and acceptor concentration.

The fifth and final chapter describes sol-gel Cu₂ZnSnS₄ thin-film production and Al/p-CZTS/Mo Schottky diode manufacturing. It analyzes the CZTS thin film's structure with XRD and its morphology with SEM. On the other hand, the electrical characterization was accomplished by analyzing the current–voltage (I–V) characteristics. A significant part of the chapter is dedicated to validating the obtained CZTS solar cell parameters by simulating the I V characteristic using extracted parameters and comparing them to experimental data. A comparative analysis of experimental and fitted I–V characteristics is presented, showcasing the effectiveness of the GA method in parameter extraction. The findings of this research contribute to the broader understanding of solar cell parameter optimization and offer a robust methodology for future applications in the field.

References

- [1] A.R. I. Rimmaudo, A. Salavei, *Effects of activation treatment on the electrical properties of low temperature grown CdTe devices*, *Thin Solid Films*, 535 (2013) 253–256.
- [2] M.A. Green, K. Emery, Y. Hishikawa, W. Warta, E.D. Dunlop, *Solar cell efficiency tables (Version 45)*, *Prog. Photovoltaics Res. Appl.* 23 (2015) 1–9. doi:10.1002/pip.2573.
- [3] Y.H. Khattak, T. Mahmood, K. Alam, T. Sarwar, U.H. Ullah, Inayat, *Smart energy management system for utility source and photovoltaic power system using FPGA and ZigBee*, *Am. J. Electr. Power Energy Syst.* 3 (2014) 86–94. doi:10.11648/j.epes.20140305.11.
- [4] K. Jimbo, R. Kimura, T. Kamimura, S. Yamada, W.S. Maw, H. Araki, K. Oishi, H. Katagiri, *Cu₂ZnSnS₄-type thin film solar cells using abundant materials*, *Thin Solid Films*. 515 (2007) 5997–5999. doi:10.1016/j.tsf.2006.12.103.
- [5] A. Mutalikdesai, S.K. Ramasesha, *Solution process for fabrication of thin film CdS/CdTe photovoltaic cell for building integration*, *Thin Solid Films*. 632 (2017) 73–78. doi:10.1016/j.tsf.2017.04.036.
- [6] Li, Y., Ru, X., Yang, M. et al. *Flexible silicon solar cells with high power-to-weight ratios*. *Nature* 626, 105–110 (2024). <https://doi.org/10.1038/s41586-023-06948-y>.
- [7] Haddout, A.; Fahoume, M.; Qachaou, A.; Raidou, A.; Lharch, M.; Elharfaoui, N. *Influence of Composition Ratio on the Performances of Kesterite Solar Cell with Double CZTS Layers—A Numerical Approach*. *Sol. Energy* 2019, 189, 491–502. <https://doi.org/10.1016/j.solener.2019.07.098>.
- [8] Qiu, L.; Xu, J.; Cai, W.; Xie, Z.; Yang, Y. *Fabrication of Cu₂ZnSnS₄ Thin Films by Microwave Assisted Sol-Gel Method*. *Superlattices Microstruct.* 2019, 126, 83–88. <https://doi.org/10.1016/j.spmi.2018.12.020>.
- [9] Chamekh, S.; Khemiri, N.; Kanzari, M. *Effect of Annealing under Different Atmospheres of CZTS Thin Films as Absorber Layer for Solar Cell Application*. *SN Appl. Sci.* 2020, 2 (9), 1507. <https://doi.org/10.1007/s42452-020-03287-9>.
- [10] Gunavathy, K. V.; Tamilarasan, K.; Rangasami, C.; Arulanantham, A. M. S. *Effect of Solvent on the Characteristic Properties of Nebulizer Spray Pyrolyzed Cu₂ZnSnS₄ Absorber Thin Films for Photovoltaic Application*. *Thin Solid Films* 2020, 697, 137841. <https://doi.org/10.1016/j.tsf.2020.137841>.
- [11] Bade, B. R.; Rondiya, S. R.; Jadhav, Y. A.; Kamble, M. M.; Barma, S. V.; Jathar, S. B.; Nasane, M. P.; Jadkar, S. R.; Funde, A. M.; Dzade, N. Y. *Investigations of the Structural, Optoelectronic and Band Alignment Properties of Cu₂ZnSnS₄ Prepared by Hot-Injection Method towards Low-Cost Photovoltaic Applications*. *J. Alloys Compd.* 2021, 854, 157093. <https://doi.org/10.1016/j.jallcom.2020.157093>.
- [12] Camara, S. M.; Wang, L.; Zhang, X. *Easy Hydrothermal Preparation of Cu₂ZnSnS₄ (CZTS) Nanoparticles for Solar Cell Application*. *Nanotechnology* 2013, 24 (49), 495401. <https://doi.org/10.1088/0957-4484/24/49/495401>.

[13] Shin, B.; Gunawan, O.; Zhu, Y.; Bojarczuk, N. A.; Chey, S. J.; Guha, S. *Thin Film Solar Cell with 8.4% Power Conversion Efficiency Using an Earth-abundant Cu₂ZnSnS₄ Absorber*. Prog. Photovoltaics Res. Appl. 2013, 21 (1), 72–76. <https://doi.org/10.1002/pip.1174>.

[14] Sun K., Yan C., Liu F., Huang J., Zhou F., Stride J. A., Green M., Hao X. (2016). *Over 9% Efficient Kesterite Cu₂ZnSnS₄ Solar Cell Fabricated by Using Zn_{1-x}Cd_xS Buffer Layer*. Adv. Energy Mater., 6: 1600046. doi: 10.1002/aenm.201600046.

Chapter 1: Overview of Principle Physics of Solar Cells

1.1. Introduction

Electricity has become essential to human life since its discovery. For instance, our phones, street lights and cars need power and gas. Our homes use national or local grid-supplied oil, gas, or electricity for lighting, heating, and appliances. All these things use fuel. These sources pollute and destroy the environment. Solar photovoltaic methods immediately convert solar radiation into power, unlike carbon fuel-generated electricity. The earth is working hard to reduce carbon emissions and limit global warming. To protect the ecosystem and the earth, we must switch to renewable energy.

In this chapter, we will present several useful concepts related to the photovoltaic conversion. Firstly, we define a photovoltaic solar cell and provide an overview of solar radiation, which serves as the primary source of energy conversion in solar cells. We delve into the operational principles of solar cell, including its equivalent circuit diagram and primary characteristics and examining the physical and technological losses that limit its efficiency. Furthermore, we explore the different generations and different structures of solar cells. We conclude this chapter by highlighting the advantages, challenges, and potential solutions of photovoltaic energy.

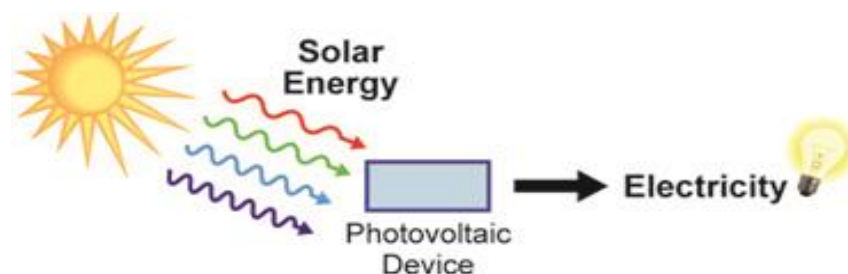


Figure.1.1: Solar cell device for transforming solar energy into electricity [1].

1.2. Physics of Photovoltaic

1.2.1. Photovoltaic effect

The origin of the expression "photovoltaic" can be traced back to the Greek word "phos," which denotes light, and "voltaic," which pertains to electricity. This term was coined in honor of the Italian physicist Alessandro Volta. The word "photovoltaic effect" pertains to the phenomenon of electricity generation, wherein electromagnetic light radiation is directly converted into electrical energy. The solar cell, an apparatus that transforms solar radiation into electrical energy, functions according to this fundamental principle. The cells commonly referred to as

photovoltaic cells, utilize sunlight as their primary energy source, facilitating the conversion of light into electrical energy. The process of conversion takes place when solar radiation induces the unrestricted movement of electrons within the semiconductor material of the cell. The generation of an electrical flow, or electricity, is facilitated by the movement of electrons through the connection of wires to the positive and negative points of a cell. This electrical flow can then be utilized to power a range of electrical devices [1].

1.2.2. Solar radiation

The emission of solar radiation bears a striking resemblance to that of a black substance at a temperature of 5800 Kelvin [2]. The intensity of sunlight is reduced when it traverses the Earth's atmosphere as a result of scattering and absorption phenomena. The solar irradiance spectrum encompasses a wide array of energies, often known as wavelengths. The notion of Air Mass (AM) pertains to the distance that light traverses as it traverses the atmosphere, and functions as a metric for quantifying the reduction in light's intensity caused by atmospheric absorption. The definition of Air Mass is given by the equation :

$$AM = \frac{1}{\cos(\theta)} \quad (1.1)$$

The zenith angle, denoted as κ , plays a crucial role in determining the Air Mass (AM) value, which signifies the distance that sunlight travels through the atmosphere. The AM value is 1 when the sun is positioned directly overhead, causing its beams to be perpendicular to the Earth's surface. The conventional range of solar radiation detected at the Earth's surface is commonly denoted as AM1.5G, with the abbreviation "G" representing global. The designation AM1.5G is associated with a zenith angle of 48.2° and has been adjusted to a solar irradiation of 1 kW/m². The process of normalisation establishes the AM1.5G spectrum as the standard for assessing the performance of solar cells under controlled laboratory circumstances. On the other hand, the AM0 spectrum, which represents the standard spectrum outside the Earth's atmosphere, signifies the absence of atmospheric attenuation of sunlight. The assessment of the anticipated performance of solar cells in space applications heavily relies on the AM0 spectrum [3]. Figure 1.2 illustrates the distinctions between the AM0 and AM1.5G spectra, offering significant insights for the advancement of solar cell research and development under diverse circumstances.

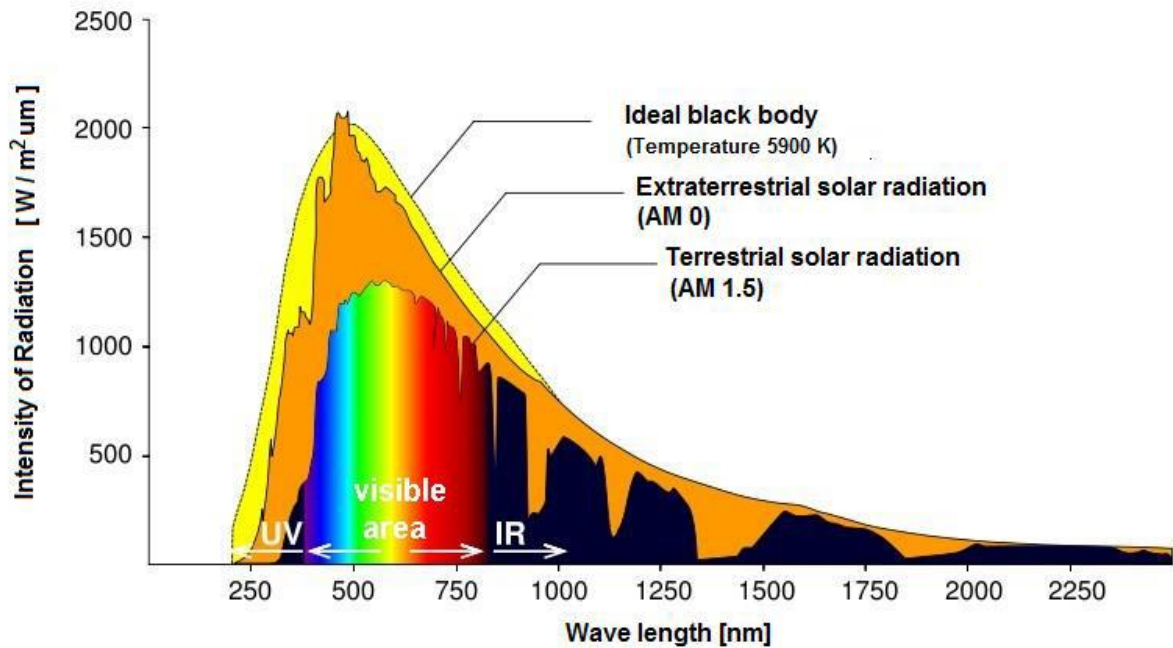


Figure 1.2: Solar irradiance spectrum above atmosphere and at Earth surface [3].

1.2.3. Principle of working of a photovoltaic cell

A photovoltaic (PV) cell operates established on the photovoltaic effect, which occurs when electromagnetic radiation causes a potential difference to be made at the junction of two different materials. The observed phenomena bears resemblance to the photoelectric effect, which is distinguished by the release of electrons from a substance when it absorbs light with a frequency exceeding a particular threshold that is dependent on the material. Albert Einstein clarified the photoelectric effect in 1905, introducing the concept that light is composed of distinct energy packets called photons. The equation that determines the energy of a photon is

$$E = h\nu \quad (1.2)$$

In this context, the symbol E denotes the energy of the photon, ν is the frequency of the light and h represents Planck's constant ($h = 6.626 \times 10^{-23} \text{ Js}$), where $\nu = c/\lambda$ and c is the speed of light in a vacuum ($C=3 \times 10^8 \text{ m/s}$). This foundational principle underlies the operation of PV cells, where photons with sufficient energy can excite electrons across the semiconductor's bandgap, generating an electron-hole pair and there by producing electrical energy through the separation and collection of these charges. The photovoltaic effect can be distributed into the subsequent three basic processes [4].

a. Generation of charge carriers due to photon absorption

Photons absorption into the photovoltaic material excites the electrons to higher energy state than initial created between $E_i \rightarrow E_f$ as shown in Figure 1.3. In Figure 1.3 (a), photons energy represented as $E_{ph} = h\nu$ excites the electrons from the valence band to conduction band after it absorbs the photons energy from Figure 1.3 (b) when $h\nu > E_g$ while other energy converted to thermal energy.

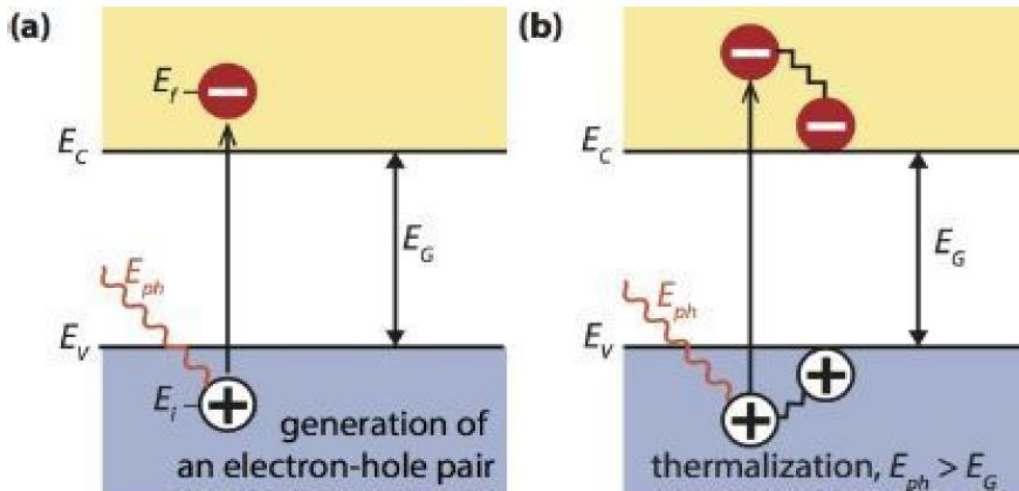


Figure 1.3: Charge carrier generation by absorption of photons [5]

Photon energy can be absorbed when there are electron energy levels E_f and E_i present. The equation (1.3) states that the photon energy is determined by the difference between E_f and E_i .

$$h\nu = E_f - E_i \quad (1.3)$$

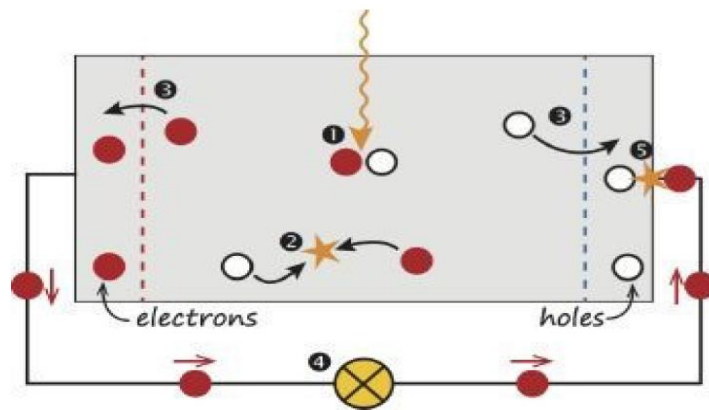
In an ideal situation electron occupy energy levels below the valence band edge (E_v) and above the conduction band edge (E_c) in a semiconductor. There are no further energy levels for the electron population between these two states. Therefore, the disparity in energy between E_c and E_v is referred to as the band gap energy, as stated in equation (1.4). Hence, photons with energy lower than the band gap energy will not be absorbed.

$$E_g = E_c - E_v \quad (1.4)$$

b. Photogenerated charge carrier separation

Recombination is the process in which an electron goes rear to its primary energy state, resulting in the release of energy. This energy can be released either through radiative recombination, which involves the emission of a photon, or through non-radiative recombination, where the energy is transferred to other electrons and holes. The existence of semi-permeable membranes on both sides of the absorber layer enables the efficient extraction of energy from electron-hole pairs in an external circuit. Electrons are emitted through one membrane, while holes are discharged through another, as seen in Figure 1.3 [5]. This diagram depicts the segregation of electrons and holes by the use of semipermeable membranes, which are formed by employing p-type and n-type materials. The solar cell design guarantees that electron-hole pairs reach their respective membranes prior to recombination. Hence, in order to ensure that the carrier travel time to each membrane is shorter than their lives, it is necessary to restrict the thickness of the absorption layer.

c. Photogenerated charge carrier extraction



1. Photon absorption generates electron-hole pair.
2. Electron-hole recombination.
3. Semipermeable membrane electron-hole separation.
4. Separated electron external circuit.
5. Electron-hole recombination following external circuit electrons passage

Figure 1.4: Simple solar cell model[5].

The process of extracting charge carriers generated by the absorption of light is made easier by connecting electrical contacts outside. This allows the energy to be used in an external circuit. The process is clearly illustrated in Figure 1.4, where the conversion of light energy into electrical energy is successfully shown. After moving via the external circuit, electrons join with holes at the junction between the back contact and the absorber layer, so completing the conversion process.

1.2.4. Physics of p–n junction

Semiconductor photovoltaic cells consist of two layers of semiconductors: an n-doped layer and a p-doped layer, which create a p-n junction [4], as shown in Figure 1.5.a. A homojunction is formed when both halves of the p-n junction are composed of the identical material. A connection formed by the combination of different materials in the n and p regions is referred to as a heterojunction. The majority charge carriers undergo diffusion in the junction region when their concentration is at their minimum. During the process, electrons undergo diffusion towards the p region, while holes undergo diffusion towards the n region. As a consequence, a region close to the interface is formed, which contains immobile charges and lacks mobile charge carriers. The region is referred to as the depletion zone, sometimes known as the Space Charge Region (SCR). Within the context of the SCR, the principle of electrical neutrality is disregarded, resulting in the generation of an electric field. This field hinders the spread of electrons and holes by causing electrons to accelerate in the opposite direction of the electric field \vec{E} , and causing holes to accelerate in the same direction as the electric field \vec{E} . This occurrence is referred to as drift. Once equilibrium is established, a voltage difference V_d arises at the junction. Figure 1.5.b illustrates the comprehensive PN junction and the corresponding phenomena.

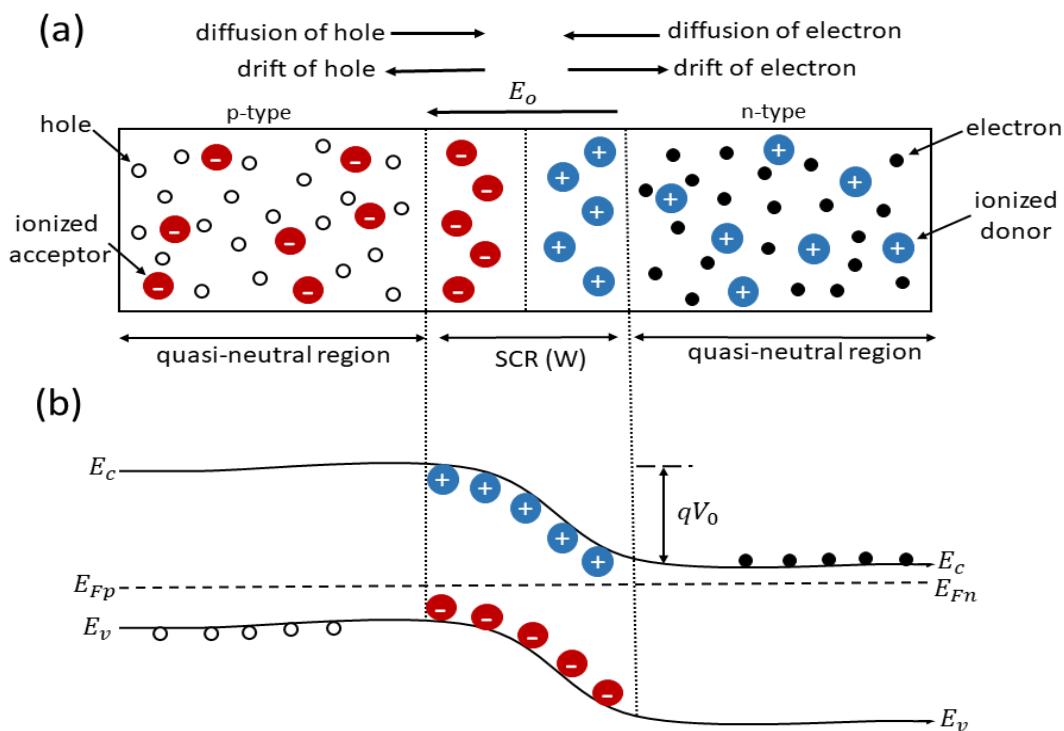


Figure 1.5: p–n junction in thermal equilibrium with zero-bias voltage applied [5].

The photovoltaic cell comprises a PN junction with electrodes affixed to the extremities. These electrodes facilitate the accumulation of photo-generated charges that are segregated by the electric field. When the depletion zone is not considered and the junction is in a state of balance, electrical neutrality is upheld. The regions adjacent to the SCR are referred to as Quasi-Neutral Zones (QNZ). Charge carriers in the QNZ exhibit movement through diffusion without any cost. Therefore, if these charges are not collected within a time period τ , they will undergo recombination. The diffusion length of a charge is the distance it covers over its lifetime τ before recombining. Charges produced by light in the QNZ are only gathered if they are created within a distance shorter than their diffusion length from the PN junction.

1.2.5. Equivalent circuit of photovoltaic cell

In order to understand how a solar cell works, it is advantageous to create a model that is electrically equivalent. A perfect solar cell can be represented by a basic model consisting of a constant current source and a diode connected in parallel, as seen in Figure 1.6. The continuous current source functions as a generator, driving electrons into the external circuit. The photocurrent, represented as I_L , is generated as a result of the photovoltaic effect. The size of the photocurrent depends on the intensity of the available sunshine; hence, the current from a source is exactly proportional to solar radiation. This indicates that a rise in the strength of accessible sunlight requires a proportional increase in I_L . The symbol I_D denotes the reverse saturation current of the solar cell [6].

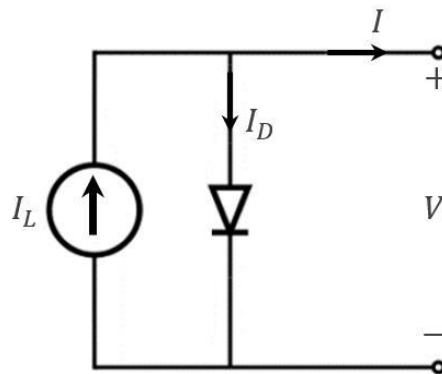


Figure 1.6: Ideal photovoltaic cell [6].

Photovoltaic cells are inherently imperfect. Therefore, both shunt and series resistance components are included in the analogous circuit. The following similar circuit is depicted in Figure 1.7.

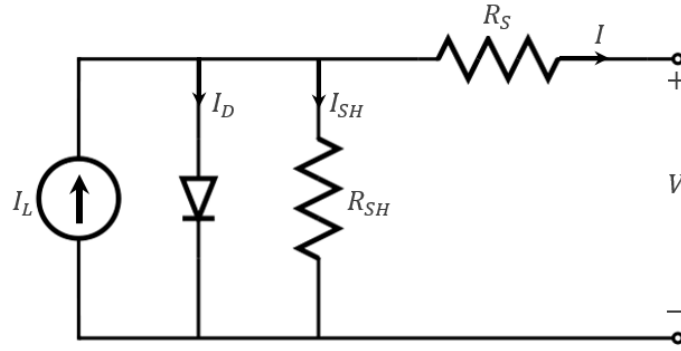


Figure 1.7: Photovoltaic cell equivalent circuit [6].

Equation 1.6 shows that the output current of a photovoltaic cell may be calculated by subtracting the photo-generated current, diode current, and shunt resistance current from each other. This is demonstrated in the schematic of a solar cell equivalent circuit.

$$I = I_L - I_D - I_{SH} \quad (1.6)$$

The voltage across these components regulated the flow of electric currents.

$$V_D = V + IR_S \quad (1.7)$$

The voltage across the shunt resistance and diode is denoted as V_D , whereas the output terminal voltage is represented as V . The voltage across the series resistance is referred to as IR_S .

Diode current from Shockley diode equation is:

$$I_D = I_0 \left[\exp\left(\frac{qV_D}{nkT}\right) - 1 \right] \quad (1.8)$$

Current flows through shunt resistance can be calculated from ohms law

$$I_{SH} = \frac{V_D}{R_{SH}} \quad (1.9)$$

By substituting these values in equation 1.6

$$I = I_L - I_0 \left[\exp\left(\frac{q(V+IR_S)}{nkT}\right) - 1 \right] - \frac{V+IR_S}{R_{SH}} \quad (1.10)$$

The photovoltaic cell is non-ideal in practice. The factors that contribute to resistance effects are edge leaks, recombination, and contacts. Figure I.7 depicts the two resistors.

The series resistance (R_s) represents the interface resistance between the front and rear contact. The short circuit resistance (R_{sh}) is connected in parallel with both the diode and the current generator. It minimizes the occurrence of a short circuit within the cell. Typically, the value of R_{sh} is bigger than R_s by at least one order of magnitude. Decrease the series resistance (R_s) and increase the shunt resistance (R_{sh}) in order to minimize losses. An optimal scenario occurs when R_{sh} is infinite and R_s is zero [7].

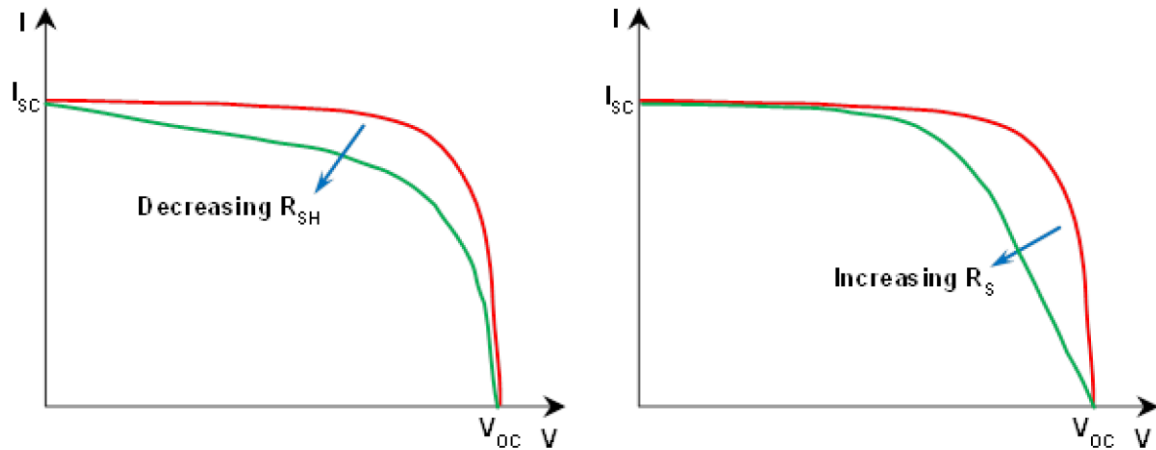


Figure 1.8: The influence of the series resistance and shunt resistance on the current-voltage (I-V) behavior of the solar cell [3].

1.2.6. Photovoltaic Cell Parameters

The J-V curves of a solar cell under dark and illumination conditions are depicted in Figure 1.9. Current density is defined as the amount of current flowing through the cell per unit area. The J-V profile undergoes a shift due to the short circuit current density (J_{sc}) when exposed to light. The J-V curve of a solar cell is often characterized by the 4th quadrant, and the fundamental characteristics of the photovoltaic cell are obtained from this curve.

The current density created by illuminating a solar cell in short circuit is referred to as J_{sc} . J_{sc} is defined as the negative value of J_{ph} and is contingent upon the intensity of light. The short circuit current density of a solar cell is determined by the point at which the J-V curve intersects the J axis at $V=0$.

The open circuit voltage (V_{oc}) is another crucial element of a solar cell. The open-circuit voltage is the electrical potential difference across a solar cell when it is exposed to light and there is no external load connected. The intersection of the V axis ($J=0$) with the J-V curve yields the value of V_{oc} , as depicted in Figure 1.9.

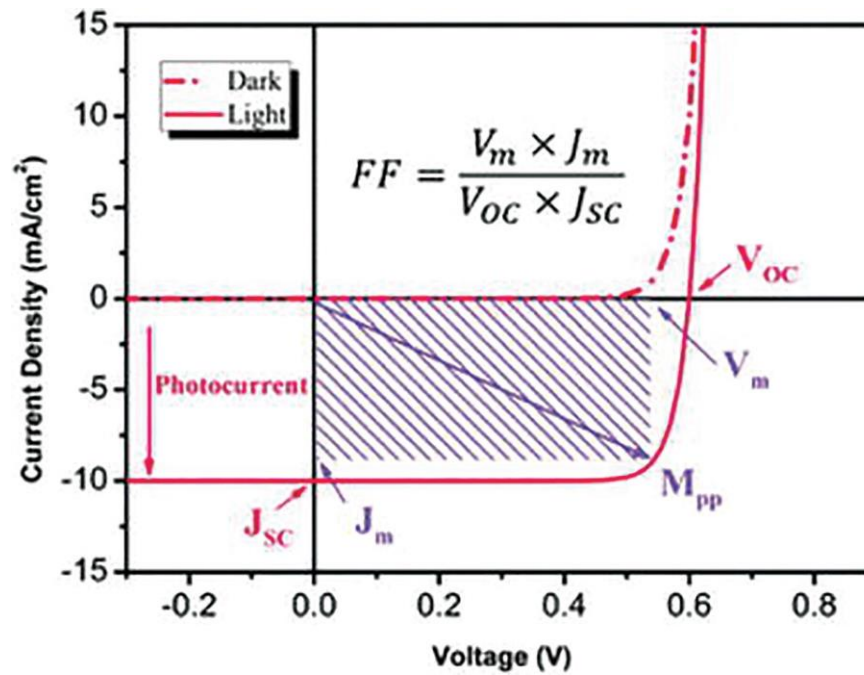


Figure. 1.9: Typical dark and light solar cell current density-voltage characteristics[9].

1.2.6.1. Short-circuit current density J_{sc}

The short circuit current I_{sc} is the current that drifts through the external circuit when the electrodes of the solar cell are short circuited. The short circuit current of a solar cell depends on the photon flux incident on the solar cell, which is determined by the spectrum of the incident light. For standard solar cell measurements, the spectrum is standardized to the AM1.5 spectrum. The I_{sc} depends on the area of the solar cell. In order to remove the dependence of the solar cell area on I_{sc} , the short-circuit current density is often used to describe the maximum current delivered by a solar cell. The maximum current that the solar cell can deliver strongly depends on the optical properties of the solar cell, such as absorption in the absorber layer and reflection.

A cell with zero potential delivers short-circuit current density. The cell can deliver this current maximum. As a function of temperature, radiation wavelength, cell active surface, and light intensity received on the cell region, carrier mobility is linearly influenced by light intensity (I.11):

$$J_{sc} = J_{ph} - J_0 \cdot \left(\exp\left(\frac{qR_s J_{sc}}{nKT}\right) - 1 \right) - \frac{J_{sc} R_s}{R_{sh}} \quad (1.11)$$

When ($R_s=0$ and $R_{sh} \rightarrow \infty$)

$$J_{sc} = J_{ph} \quad (1.12)$$

1.2.6.2. Open-circuit voltage V_{oc}

The open-circuit voltage (V_{oc}) of a solar cell is the maximum voltage it can produce while there is no current flowing through it. The open-circuit voltage is a consequence of the forward bias of the solar cell junction caused by the current created by light. The equation (I.13) yields the result.

$$0 = I_{ph} - I_0 \cdot \left(\exp\left(\frac{qV_{oc}}{AKT}\right) - 1 \right) - \frac{V_{oc}}{R_{sh}} \quad (1.13)$$

When ($R_s=0$ and $R_{sh} \rightarrow \infty$)

$$V_{oc} = \frac{nKT}{q} \ln\left(\frac{I_{sc}}{I_0} + 1\right) \quad (1.14)$$

1.2.6.3. Fill Factor FF

The Fill Factor is a quantitative measure that evaluates the shape quality of the current-voltage characteristic J-V. It is also the ratio between the highest power output of a cell and the theoretically achievable power output for optimal performance [8][9]. The equation utilized to define this ratio is as follows:

$$FF = \frac{P_m}{I_{sc}V_{oc}} = \frac{I_m V_m}{I_{sc}V_{oc}} \quad (1.15)$$

I_m and V_m denote the current-voltage pair at which the cell delivers the maximum power, denoted as P_m . Theoretical research suggest that the fill factor ranges from 0.25 to 1. When the fill factor falls below 25%, it often indicates the presence of a non-ohmic contact or an oxidized/insulating layer at the interface between the material and electrode. This event can provide information on the quality of the material-electrode interfaces.

1.2.6.4. Power Conversion Efficiency PCE

The power conversion efficiency (PCE) is the fundamental parameter used to evaluate the performance of a solar cell. The cell's efficiency is determined by its capacity to convert light energy into electrical power, which may be quantified as the ratio between the highest power output of the cell and the incident power P_{in} . The mathematical expression that represents this relationship is as follows:

$$PCE = \frac{P_m}{P_{in}} = \frac{I_{sc}V_{oc}FF}{P_{in}} \quad (1.16)$$

The incident power of the light is equivalent to the solar power, which is measured at 100 mW/cm². To enhance conversion efficiency, one might increase the Fill Factor, short-circuit current, and open-circuit voltage [10].

1.2.7. Generation and Recombination

Carrier generation and recombination take place when an electron undergoes a transition from the conduction band (E_V) to the valence band (E_C) inside the bandgap of a semiconductor. This

transition occurs due to interactions with other electrons, holes, or photons. During the process of generation, electron-hole pairs are formed by the excitation of an electron, resulting in the creation of a vacancy in the E_v . Recombination is the inverse phenomenon in which electrons from the conduction band (E_c) and holes from the valence band (E_v) mix, leading to the release of a photon. The duration of carrier production in semiconductors is determined by recombination processes, which restrict the current generation and thus impact the device's performance. There exist three distinct categories of conventional recombination processes [11,12,13]:

✓ **Auger Recombination**

Auger recombination is highly efficient in semiconductors with a high density of charge carriers due to intense doping under concentrated sunlight. It includes three carriers. Upon recombination, the electron and hole do not emit a photon, but instead transfer their energy to a third carrier, an electron in the E_c . This mechanism restricts the duration and effectiveness of the solar cell. In this process, at low injection level, the expression of the recombination rate is related to the excess carrier concentration and to doping density [20]:

$$R_{Auger} = (C_p \cdot p + C_n \cdot n)(np - n_i^2) \quad (1.14)$$

with C_n and C_p the Auger coefficients for electrons and holes.

✓ **Radiative (band-to-band) Recombination**

Radiative recombination is the primary mechanism of recombination in direct bandgap semiconductors. This phenomenon takes place when an electron from the conduction band (E_c) immediately joins with a hole in the valence band (E_v) and emits a photon with energy that closely matches the bandgap of the semiconductor.

The formula for the total recombination rate is given by:

$$R_{radiative} = B \cdot (n \cdot p - n_i^2) \quad (1.15)$$

Here B is a proportionality constant which is called radiative recombination coefficient; n and p are the concentrations of free electron and hole.

✓ Shockley-Read-Hall (SRH) Recombination

Shockley-Read-Hall recombination, also known as recombination by defects. It happens when an electron or hole becomes stuck in an energy state within the forbidden gap, which is created by imperfections in the crystal lattice. The unbound carriers are caught by the traps and then released by a thermal activation procedure.

The theory for recombination through these localized traps was for the first time analyzed by Shockley and Read [12, 13] and then by Hall. Their analytical model which describes the recombination rate (SRH-rate) is given by:

$$R_{SRH} = \frac{pn - n_i^2}{\tau_p \left(n + n_i \exp\left(\frac{E_T - E_{Fi}}{kT}\right) \right) + \tau_n \left(p + n_i \exp\left(-\frac{E_T - E_{Fi}}{kT}\right) \right)} \quad (1.16)$$

Where n_i is density of intrinsic charge carriers. Here, E_T and E_{Fi} are, respectively, the recombination center and the intrinsic Fermi energy levels; and σ_n , (σ_p) is the capture cross section, that is an estimation of how much the electron (hole) must be near to the trap to be captured.

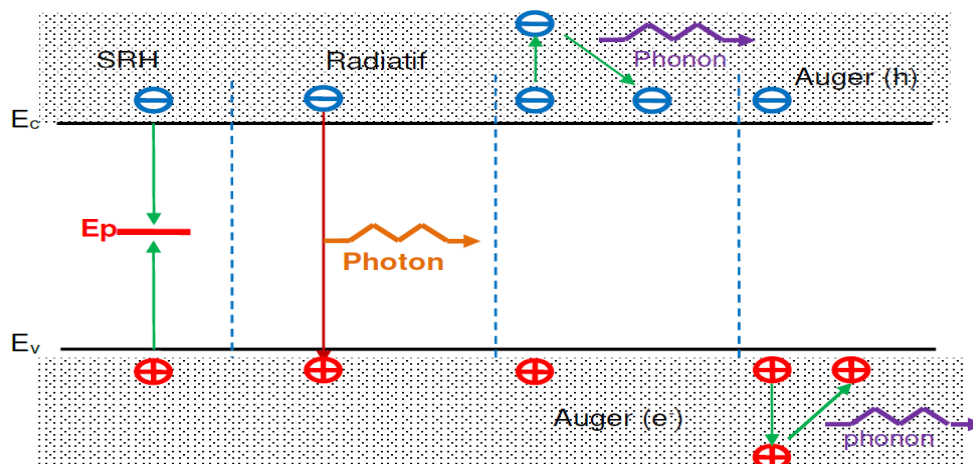


Figure I.10: Generation and types of recombination processes [11].

1.2.8 Minority Carrier Lifetime

If minority electrons in the conduction band, when in an excited state, remain uncollected for a certain period or if the concentration of minority carriers significantly surpasses that of the bulk volume, these excess minority electrons will undergo recombination with majority holes. The duration between generation and recombination is termed as the minority carrier lifetime of a material, which plays a crucial role in solar cell performance. In materials experiencing low-level

injection (where the number of minority carriers is less than the doping), the minority carrier lifetime is directly proportional to the excess minority carrier concentration (Δn) and inversely proportional to the recombination rate (R), as described in equation 1.17.

$$\tau = \frac{\Delta n}{R} \quad (1.17)$$

Nevertheless, recombination can occur in both the surface and bulk of the semiconductor. Consequently, there are two lifetimes, τ_s and τ_b , associated with these respective recombination mechanisms. The effective minority carrier lifetime is the sum of both surface and bulk recombination lifetimes.

$$\frac{1}{\tau_{eff}} = \frac{1}{\tau_s} + \frac{1}{\tau_b} \quad (1.18)$$

The recombination in the bulk may result due to radiative, trap or Auger process. Thus the minority carrier lifetime in the bulk region can be written as,

$$\frac{1}{\tau_b} = \frac{1}{\tau_{radiative}} + \frac{1}{\tau_{SRH}} + \frac{1}{\tau_{Auger}} \quad (1.19)$$

1.2.9. Energy Band alignment

When two semiconductors, SC-1 and SC-2, with electron affinities χ_1 and χ_2 respectively, are brought into contact, energy equilibrium is formed. This causes the Fermi levels of both materials to align, resulting in band bending at the interface, as shown in Figure 1.11.

The energy discontinuities can be estimated using the Anderson's approximation [15], under the assumption of a flawless contact.

The conduction band offset (CBO):

$$\Delta E_c = \chi_1 - \chi_2 \quad (1.20)$$

The valence band offset (VBO):

$$\Delta E_v = E_{g1} - E_{g2} - \Delta E_c \quad (1.21)$$

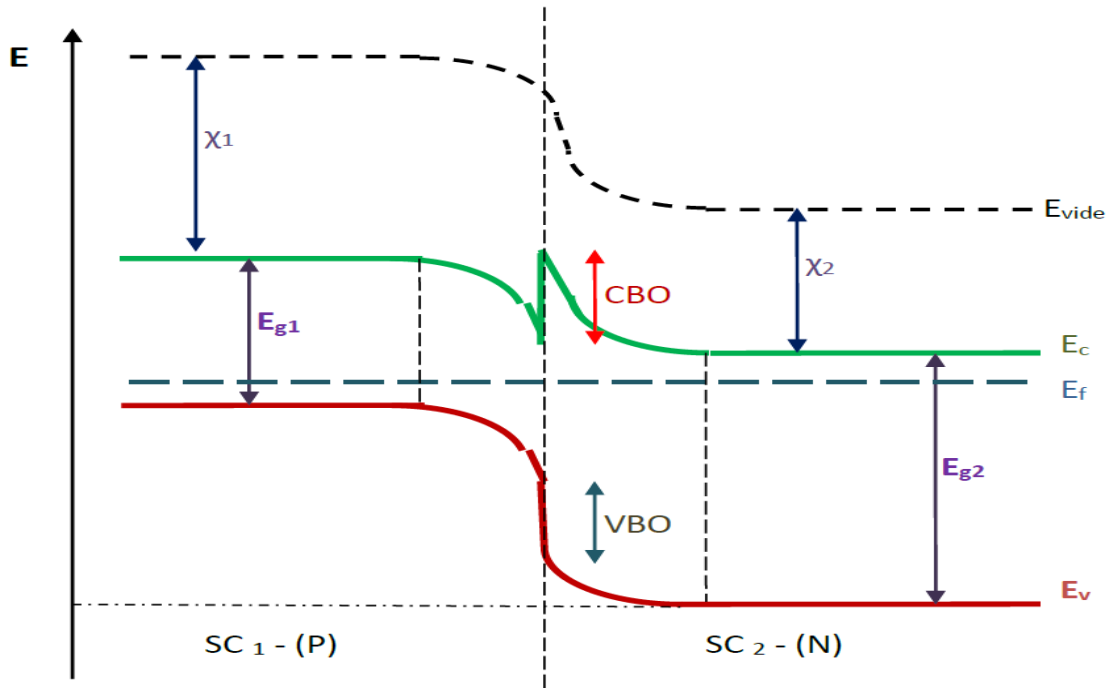


Figure 1.11: Band structure of a hetero-junction [15].

A positive band discontinuity is commonly known as a spike-like energy barrier. If the discontinuity has a negative value, it is referred to as an energy step for electrons in the conduction band. In this scenario, it forms a barrier that resembles a cliff-like.

Figure 1.12 depicts a schematic illustration of the two aforementioned types of barriers.

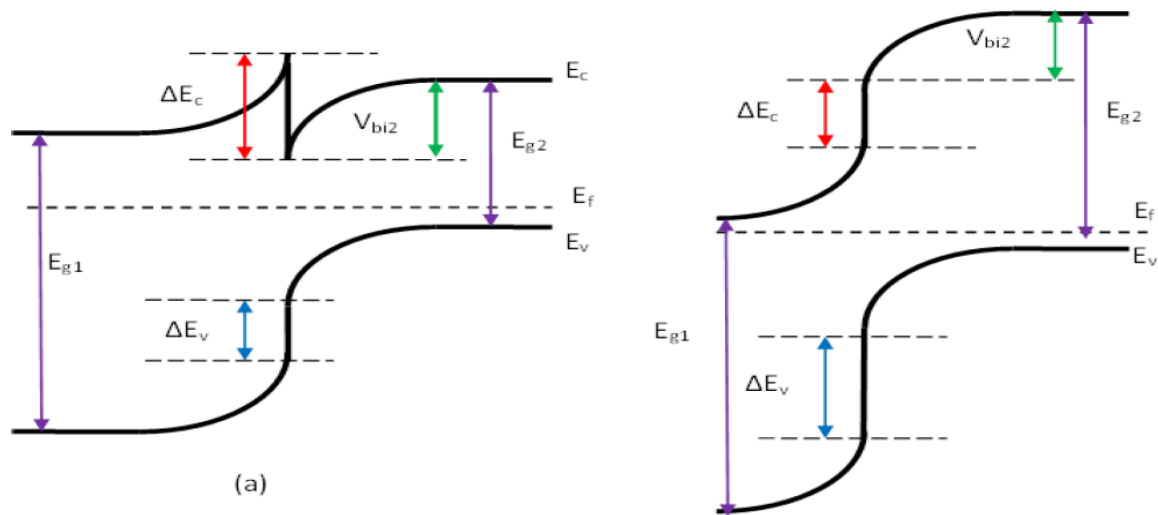


Figure 1.12: Two types of barriers: (a) spike-like barrier and (b) cliff-like barrier [15].

In the case of a negative conduction band difference, the open-circuit voltage V_{oc} decreases significantly due to the absence of any obstruction to electron flow and the promotion of their recombination at the interface defects. In contrast, when there is a positive difference ($\Delta E_c > 0.4$), electrons may have difficulty in transferring from the absorber to the buffer layer because

of the overly elevated barrier. This will have an impact on the amount of electric current that can be collected. However, when the energy difference ($0 < \Delta E_c < 0.40$) between two barriers exists, it can be surpassed by the thermionic effect. This enables a balance to be achieved between the photo-voltage and photo-current.

1.3. Photovoltaic cell technologies

Commercial photovoltaic solar cells can be categorized into two main groups: crystalline silicon (c-Si) wafer-based solar cells and thin-film solar cells. Currently, the distribution of the annual global market is 85-90% for the first generation and 10-15% for the second [16]. Furthermore, there exists a variety of now developing technologies, such as sophisticated thin-film designs, PV concentrators, organic, and photo-electrochemical solar cells. Over the course of time, novel and inventive ideas are under consideration. It is anticipated that the implementation of nano-geometries, plasmonic effects, and up or down conversion will result in a substantial improvement in performance and a decrease in costs [16]. Figure 1.13 illustrates a comparison of different technologies in terms of their efficiency in converting solar energy to electricity. This comparison serves as a guide to understand the chronological and topical development of photovoltaic (PV) technology. The new concepts are categorized into three generations based on their technological advancements [17].

Solar cells are traditionally categorized into three generations.

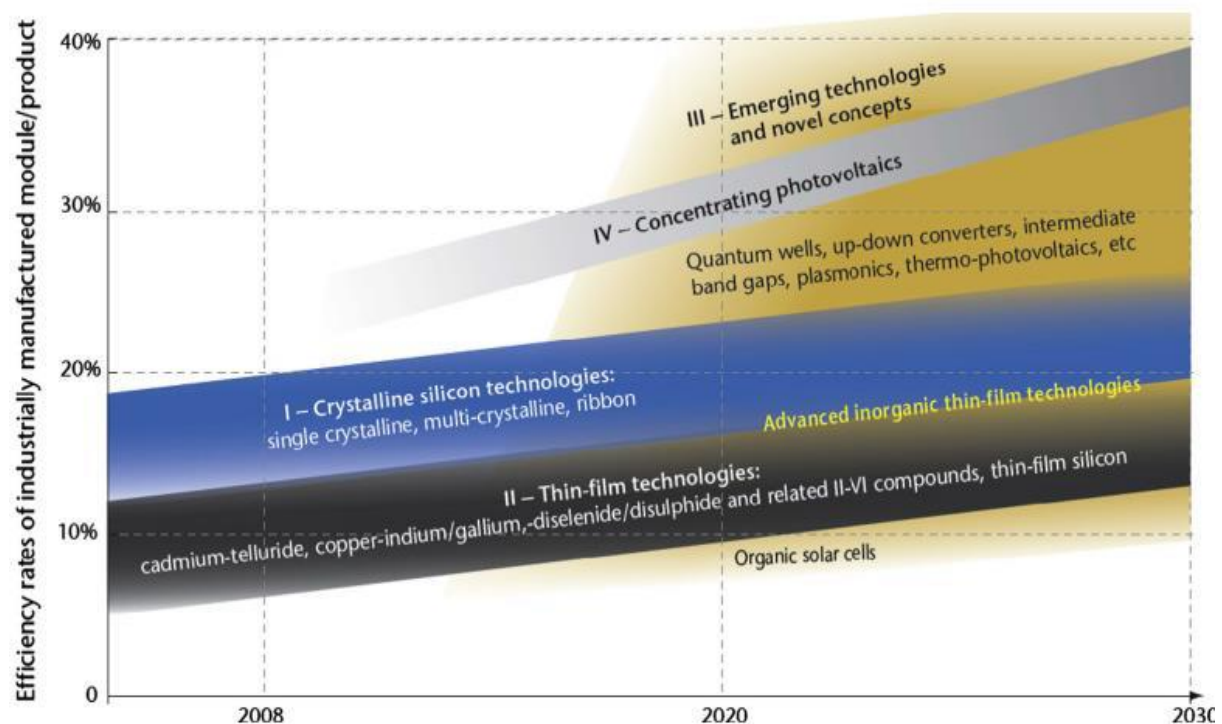


Figure 1.13: An analysis of the historical, present, and future state of photovoltaic technology [17].

1.3.1 First Generation solar cells

Presently, it holds the highest level of usage. Nevertheless, it is evident that the efficacy of cells in this particular group has either remained stagnant or had minimal growth in the last two decades. This is mostly due to the constrained absorption range of silicon, which is limited to the visible and near-infrared regions. However, it is the most developed technology and provides the most favorable ratio of price to performance. Different module technologies can be classified according to the production of silicon material.

After oxygen, silicon is the second most abundant element found in the Earth's crust. It is advantageous because it can be manufactured from a nearly unlimited natural resource called silica, which is found in granite, sand, and sandstone [16]. In 1954, the initial silicon solar cell was produced at Bell Laboratories in the United States, achieving an efficiency of 6% [17]. This sector comprises monocrystalline and multicrystalline variants of silicon-based materials with a crystalline structure.

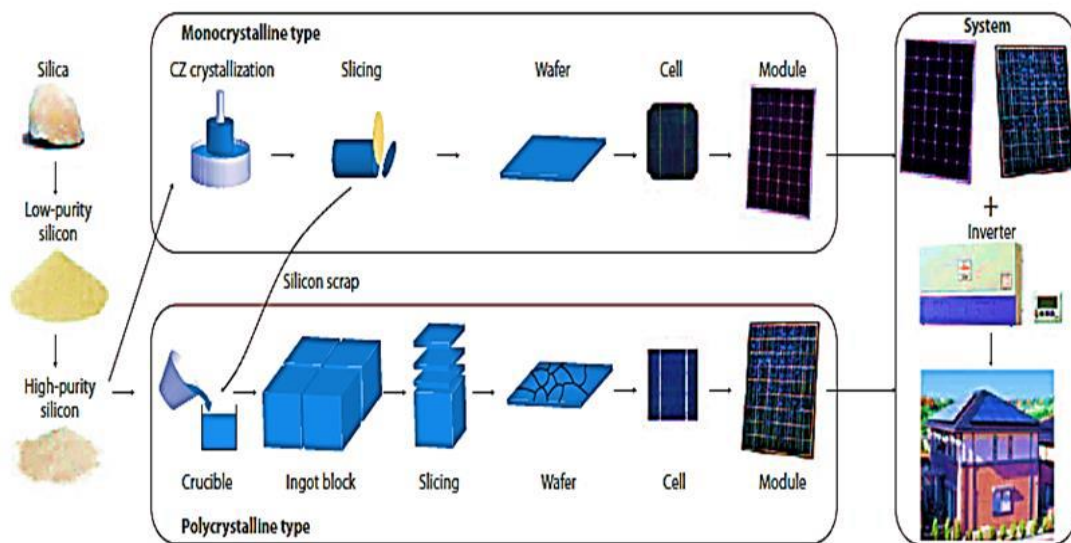


Figure 1.14: The manufacturing process for standard commercial crystalline silicon solar cells [16].

1.3.2. Second Generation solar cells

The primary thin-film technologies comprise amorphous silicon, which has been employed in many applications for a considerable period, particularly in watches and calculators, CdTe (Cadmium Telluride heterojunction), CIS or CIGS (Copper Indium Gallium Diselenide heterojunction). This talk will mostly discuss single-junction cells, which function in a similar manner as multi-junction cells by utilizing different layers to capture a wider range of solar energy. Nevertheless, these technologies are highly intricate and now limited to specialized niche

applications, such as concentrating solar power, predominantly employed in spacecraft. Thin-film technologies utilize materials that have a high coefficient of absorption for the solar spectrum, such as:

- Amorphous Silicon (a-Si): The utilization of amorphous silicon can be traced back to the early 1970s (Figure 1.15). The utilization of thin-film form presently yields cost-effective generators that rival preceding technologies.
- Cadmium Telluride (CdTe) is a type of polycrystalline material that is applied onto glass substrates. The initial cells were created in 1972. The conversion efficiency attained using this method is considerably more gratifying. Nevertheless, the primary constraint hindering the extensive implementation of this technique is the hazardous nature of cadmium.
- Copper Indium Selenide (CIS or CIGS) is a technologically advanced material that has great promise for future advancements, with laboratory efficiency reaching up to 20% [15]. Nevertheless, there is a limited supply of the ingredients needed for producing this particular form of cell [14]. Furthermore, their efficiency is now the highest among thin-film solar cells. A solar cell measuring around 0.5 cm², manufactured by Solar Frontier-Japan, reached a record efficiency of 22.3% on December 8, 2015 [17].

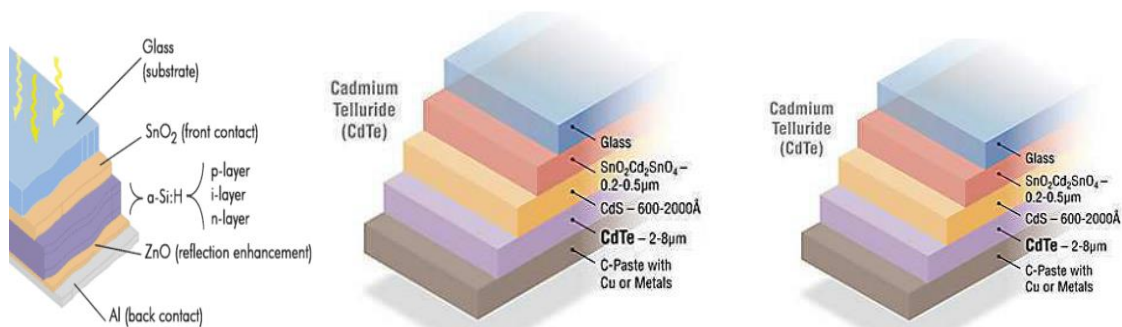


Figure 1.15: Thin film Photovoltaic Cell [14].

CIGS cells have higher heat resistance compared to crystalline silicon cells; however they are not as resilient as CdTe cells. Furthermore, thin-film technologies have a minor advantage in capturing light throughout the early morning and late afternoon, with an increase in efficiency of a few percentage points. CIGS cells can be fabricated on plastic supports, soda-lime-silicate glass with a thickness ranging from 1 to 3 mm, or on metal foils.

1.3.3. Third Generation solar cells

The objective is to create a next-generation of significantly lighter and more efficient cells by utilizing polymers and organic components. The fundamental concept is to substitute the mineral compounds that make up the solar cell with polymers or organic molecules. The goal for today is to enhance the effectiveness of light absorption and manipulate the structure of cells in order to raise overall efficiencies. Upcoming organic cells will possess the qualities of transparency, flexibility, and notably thinness. When placed on rooftops, walls, or even windows, these devices will provide the necessary electricity for the building's energy use. Designed for compatibility with mobile phones and portable devices, they will offer power.

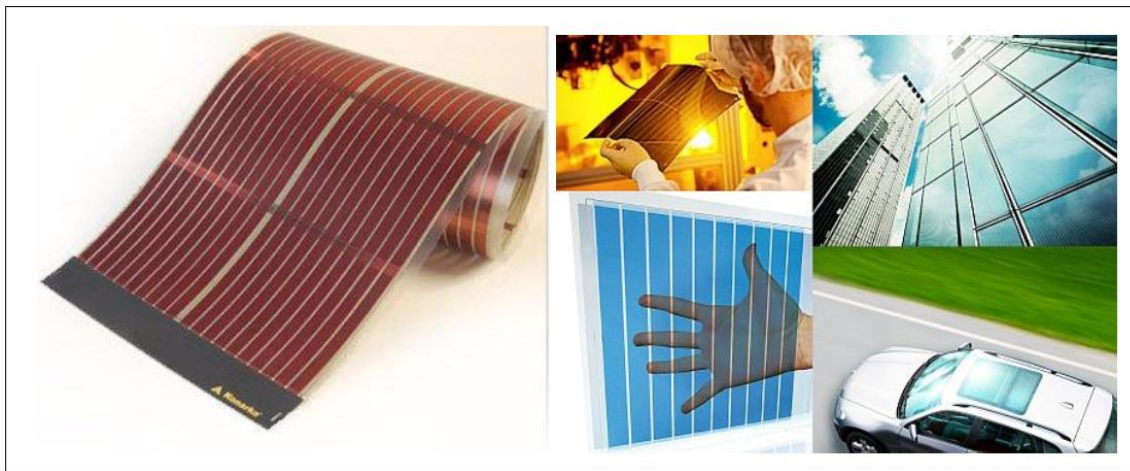


Figure 1.16: Organic Photovoltaic Cell "HeliaFilm"[18]

The perovskite sector refers to a novel kind of solar cells. It is still in the experimental phase and has not been released for public use. Perovskite is a crystalline structure that is based on the structure of calcium titanate CaTiO_3 [18]. The photovoltaic characteristics of this material, such as its ability to absorb photons, which is 10 times higher than silicon, efficient separation of electric charges, and their mobility, are attributed to a recent discovery [18]. The credit for this finding is attributed to two renowned experts in the field: Michael Graetzel from the Ecole Polytechnique Federale de Lausanne, and Henry Snaith from the University of Oxford. In 2009, Toim University in Japan developed the inaugural photovoltaic cell with an efficiency rating of 3.8% [18]. The Ecole Polytechnique Federale de Lausanne (EPFL) holds the world record in this field. Nevertheless, the primary obstacle faced by perovskite solar cells is their long-term stability and the inclusion of lead within their molecular structure.

1.4. The advantages, Challenges, and Possible Solutions

Like any other technology, PV technology has its own unique advantages and disadvantages. The list below provides reasons for the differing opinions on the technology, along with corresponding solutions to the challenges [19].

1.4.1. The advantages

Solar PV technology offers a multitude of advantages. The following paragraphs provide a clear explanation of these points:

1. Renewable energy: The electricity generated by solar PV modules does not produce any greenhouse gas (GHG) emissions. Greenhouse gases (GHGs) are the primary cause of significant environmental harm, including global warming and climate change. Photovoltaic (PV) technology guarantees that energy generation is free from any emissions.

2. PV technology is centered around the conversion of sunlight into electricity using Silicon modules, which are derived from sand and are one of the most plentiful elements on Earth. This makes it a sustainable energy source. As long as solar radiation reaches the Earth, we can ensure a consistent supply of electricity.

3. Noiseless technology: Photovoltaic systems typically lack any mechanical components that could generate noise. Thus, it is regarded as a viable renewable resource that can be implemented in residential areas. However, other renewable generation systems are excessively large in size and intricate in operation to be suitable for installation in local areas.

4. Minimal maintenance requirement: Photovoltaic modules necessitate minimal technical upkeep. Periodic cleaning is necessary to prevent waste materials from obstructing the modules' access to sunlight.

5. PV module manufacturers typically offer a linear performance warranty for the modules listed in their datasheet, which covers the entire operating lifespan [20].

6. There are no limitations based on location: Photovoltaic (PV) modules can be installed anywhere in the world, regardless of site conditions. This is because PV modules are capable of generating electricity even in cloudy areas. Nevertheless, it is more desirable to install PV systems in a sunny location that is unobstructed by the shadows of tall trees or buildings.

7. Affordable: Over the past twenty years, the price of PV modules has significantly decreased, reaching a global ex-factory gate price of 0.214 \$/W for polycrystalline Silicon modules. Recent

advancements in semiconductor technologies suggest that prices will continue to decrease in the near future.

8. **Maturing with continued promise:** Despite experiencing a significant boom in the early twenty-first century, the photovoltaic (PV) industry has demonstrated considerable maturity and potential for integration into the well-established utility grids industry. This potential is expected to grow in the coming years due to advancements in efficiency and lifespan.

9. **Solar module recycling:** Once a solar module reaches the end of its lifespan, it can be recycled due to its composition primarily consisting of glass, silicon, and various metals.

10. **Reduced susceptibility to natural disasters:** Solar PV systems exhibit a lower level of vulnerability to natural disasters such as earthquakes, floods, and tsunamis [21].

1.4.2. The Challenges

There are specific difficulties related to the installation of solar photovoltaic (PV) technology, which is outlined below:

1. **The initial and recycling costs of PV applications are high, but their maintenance costs are relatively negligible.** Nevertheless, the initial expense can be significantly higher when compared to traditional resources for large-scale implementations. Furthermore, after its use, carrying out multiple recycling procedures such as segregation, fusion, and disintegration of each component may exceed its selling price in terms of expenses.

2. **Inconsistent and variable energy:** The amount of energy produced by solar modules depends on the unpredictable solar irradiance that is present during the day, which can also change due to shading. Thus, due to its intermittent characteristics, solar energy is often regarded as secondary in the electricity markets.

3. **The need for energy storage:** Energy storage technology provides a solution to the problem of solar power's intermittent nature by compensating for fluctuations that occur during periods of shading. Nevertheless, the durability of energy storage components, such as batteries, is shorter compared to that of solar modules. Consequently, these components need to be replaced multiple times over the course of the project's lifespan. Put simply, the addition of a new operating cost can result in an increase in the initial cost of the PV system.

4. **Toxicity and disposal concern:** The manufacturing process of PV modules does not completely eliminate carbon emissions. When solar modules containing heavy elements like Cadmium, Lead, and Selenium are taken apart, they can release toxic substances. While solar

modules can be recycled, certain components cannot be fully recycled, resulting in additional waste.

5. Footprint: Due to the relatively low efficiency of the light-electricity conversion process, PV modules require a substantial amount of space to generate enough energy to meet the load or grid demand. This challenge pertains to the placement and financial implications of the land installation.

1.4.3. The Potential Solutions

As solar technology is being widely adopted worldwide, researchers and engineers are actively working on solutions to address its challenges, driven by its rapid evolution. Due to the commercialization of the most recent semiconductor technologies, the price of solar modules is experiencing a substantial decrease. Despite the high initial cost, the system typically provides a quick return on investment. Furthermore, energy storage systems such as Batteries are being incorporated to tackle the problem of inconsistent and variable energy. These batteries are being used with optimized controllers to enhance their lifespan. Researchers are also endeavoring to reduce the cost of recycling and disposing of expired module parts, while also preventing the release of toxic substances. Both local and federal regulations are currently being implemented to ensure the appropriate disposal of hazardous materials, with the aim of preventing toxicity and disposal-related problems. In addition, the use of innovative mounting mechanisms allows installers to maximize the utilization of the available land. Ongoing research and progress in solar technologies will significantly reduce the difficulties encountered in installing solar modules, positioning it as a prominent energy source in numerous regions worldwide in the coming years [19].

1.5. Conclusion

In this chapter, we presented the operating principles of a photovoltaic cell, including its $I(V)$ characteristics in darkness and under illumination, and its various parameters. These include the open-circuit voltage (V_{oc}), the short-circuit current density (J_{sc}), the fill factor (FF) and the power conversion efficiency. We also discussed the losses due to series resistance (R_s) and shunt resistance (R_{sh}), along with a description of the different generations of the cell. We conclude with a discussion of the advantages, challenges, and potential solutions.

References

- [1] P.J. Sturman, *Photovoltaic and Photo-refractive Effects in Non centrosymmetric Materials*, CRC Press Taylor & Francis Group, 1992
- [2] NASA Solar System Exploration – Sun: Facts & Figures retrieved 27 April 2011.
- [3] S.S. Li, *Semiconductor Physical Electronics*, Springer US, Boston, MA, 1993.
- [4] M.Z. Klaus Jager, Olindo Isabella, Arno H. M. Smets, Rene A. C. M. M. van Swaaij, *Solar Energy Fundamentals, Technology and Systems*, 2014.
- [5] S.S. Li, *Semiconductor Physical Electronics*, Springer US, Boston, MA, 1993.
- [6] A. Ortiz-Conde, F. García-Sánchez, J. Muci, A. Sucre-González, *A review of diode and solar cell equivalent circuit model lumped parameter extraction procedures*, Facta Univ.-Ser. Electron. Energ. 27 (2014) 57–102.
- [7] A. McEvoy, T. Markvart, L. Castañer, T. Markvart, and L. Castaner, *Practical handbook of photovoltaics: fundamentals and applications*: Elsevier, 2003.
- [8] B. Qi and J. Wang, "Fill factor in organic solar cells," *Phys. Chem. Chem. Phys.*, vol. 15, no. 23, p. 8972, May 2013.
- [9] M. A. Green, "Solar cell fill factors: General graph and empirical expressions," *Solid. State. Electron.*, vol. 24, no. 8, pp. 788–789, Aug. 1981.
- [10] Mathieu, H. *Physique des semiconducteurs et des composants électroniques*, Dunod, sciences sup, 2009.
- [11] S. M. Sze and K. N. Kwok, *Physics of Semiconductor Devices*, no. 1. 2007.
- [12] W. Shockley and W. T. Read, "Statistics of the Recombinations of Holes and Electrons," *Phys.Rev.*, vol. 87, no. 5, pp. 835-842, 1952.
- [13] R. N. Hall, "Electron-Hole Recombination in Germanium," *Phys.Rev.*, vol. 87, no. 2, p. 387, 1952.
- [14] Nelson, J., *The physics of solar cells*. 2003: World Scientific Publishing Company.
- [15] Andrea Crovetto, Ole Hansen, What is the band alignment of Cu₂ZnSn(S,Se)₄ solar cells?, *Solar Energy Materials and Solar Cells*, Volume 169, 2017, Pages 177-194, ISSN 0927-0248,
- [16] Abermann, S. (2013). *Non-vacuum processed next generation thin film photovoltaics: Towards marketable efficiency and production of CZTS based solar cells*. *Solar Energy*, 94, 37-70.
- [17] T. Saga, "Advances in crystalline silicon solar cell technology for industrial mass production," *npg asia materials*, vol. 2, p. 96, 2010
- [18] Green, M. A. (2006). *Third-Generation Photovoltaics: Advanced Solar Energy Conversion*. Springer, Berlin.
- [19] Yaman Abou Jieb, Eklas Hossain, *Photovoltaic Systems Fundamentals and Applications*, Springer Nature Switzerland AG 2022.
- [20] A. Gong, *Understanding PV system losses, part 1: nameplate, mismatch, and lid losses* (2021) <https://www.aurorasolar.com/blog/understanding-pv-system-losses-part-1/>
- [21] E. Hossain, S. Roy, N. Mohammad, N. Nawar, D.R. Dipta, *Metrics and enhancement strategies for grid resilience and reliability during natural disasters*. *Appl. Energy* **290**, 116709 (2021)

Chapter 2:

Literature review of CZTS based solar cells

2.1. Introduction

Solar energy has become a highly abundant resource in the renewable energy sector, with applications ranging from large-scale businesses to residential consumption. Thick-film Silicon solar cells have dominated the solar cell market since they were first developed. Nevertheless, due to recent technological progress, thin film has emerged as the favoured configuration for solar cells due to its numerous advantages over thick cells. CIGS (Copper Indium Gallium Diselenide) and CdS (Cadmium Selenide) have demonstrated exceptional performance in the field of thin film technology. However, because to issues related to toxicity and high expenses, these cells are not considered to be practical or viable.

$\text{Cu}_2\text{ZnSnS}_4$ generally abridged as CZTS (Copper Zinc Tin Sulfide), a substitute for CIGS, has remarkable photovoltaic properties and possesses exceptional light absorption capabilities.

Moreover, the components of CZTS are plentiful in the natural environment, resulting in a reduction of associated expenses. In order to improve effectiveness, a variety of structural and material characteristics have been altered through experimentation. Despite multiple tries, the efficiency of the single-junction CZTS solar cell has not surpassed 13%. This chapter provides a comprehensive overview.

2.2. Advancements in kesterite Solar Cell Technology

Amazing progress has been made in CZTS solar cells throughout the last twenty years. In order to provide a more unambiguous viewpoint, we have gathered the year-wise data of CZTS research papers and citations in Figure 2.1, which clearly demonstrates a noticeable upward trend in CZTS solar cell research. The fabrication of CZTS thin film solar cells involves the use of substrate and superstrate combinations. Considerable research has been conducted on the substrate-structure of CZTS-based solar cells, as well as the manufacturing of the superstrate structure of CZTS devices. Following a thorough examination spanning many years, the device with a substrate structure including a Cd-alloyed CZTS absorber has obtained the highest peak power conversion efficiency (PCE) of 12.6%. [1] However, the challenges for researchers in further enhancing the power conversion efficiency (PCE) of S-J CZTS solar cells have arisen from issues with the CZTS absorber and the front/back interfaces. To address these difficulties, exceptional endeavors have been undertaken and documented in the literature. These efforts include doping and alloying

techniques, etching and post-annealing treatments for absorber CZTS [2,3], incorporation of barrier/passivation layers at Mo/CZTS [4] and CZTS/buffer layer interfaces [5], and investigation of new buffer layers. Substantial outcomes have been attained. Furthermore, to surpass the S-Q limit, scholars have explored the use of CZTS as a top- and middle-cell in tandem devices for both experimental and theoretical studies. Consequently, research has been initiated in this particular area. While numerous valuable review papers have been written on kesterite solar cells in recent years, the advancements, difficulties, and future potential of pure sulfide-based CZTS solar cells have been more extensively examined in conjunction with CZTSe and CZTSSe solar cells.[2,6] Notwithstanding their publication in 2018, Khalate et al.[7] and Ravindiran et al.[8] focused mostly on sulfide-based CZTS solar cells in their review papers.

However, much progress has been made in the sector since then, and still, the previously published review papers fail to adequately summarize the prior developments in CZTS solar cells. In this context, a thorough and current analysis particularly focused on pure sulfide-based CZTS solar cells is necessary to close this disparity.

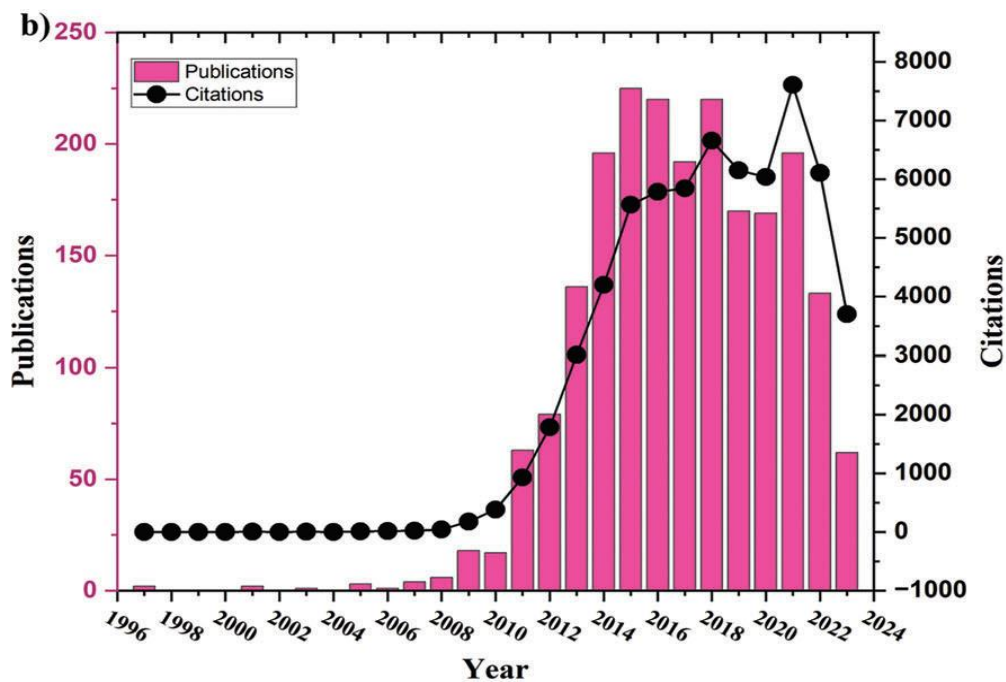


Figure 2.1 : Evolution of the number of publications and citations per year for CZTS material till October 2023; search for “ $\text{Cu}_2\text{ZnSnS}_4$ (CZTS) solar cells”, source: Web of Science database. [9]

2.3. Properties of CZTS

CZTS, a polycrystalline semiconductor also known as kesterite, is favored for thin-film solar cells due to its abundance, eco-friendly profile, and non-toxic nature [9,10]. Its constituents Copper, Zinc, Tin, and Sulfide are relatively plentiful on Earth compared to those in CIGS, making CZTS

an appealing alternative [11,12]. With a structure akin to CIGS, CZTS boasts long-term stability and excellent light absorption capabilities thanks to its kesterite structure.

Its absorption coefficient of 10^4 cm^{-1} leads to efficient hole-electron pair generation upon exposure to light [14]. CZTS features a straight optical band gap, making it an excellent candidate for the absorber layer. The band gap can be adjusted between 1.4 and 1.6 eV through various preparation methods, dopants, or replacements [11, 15]. Acting as an intrinsic p-type semiconductor, CZTS offers promise for thin-film solar cells. Recent research suggests that replacing Sulfide (S) with Selenium (Se) can further decrease the band gap to 1 eV [16]. These inherent properties position CZTS as a highly viable option for absorber layers in thin-film solar cells.

2.3.1. The CZTS Structure

There are three potential tetragonal crystal forms that CZTS (copper zinc tin sulfide) can adopt: kesterite, stannite, and primitive-mixed CuAu (PMCA) structures [17,18].

The Kesterite type structure is formed by substituting In atoms with Zn and Sn in the Chalcopyrite type CuInS_2 (CIS) structure [19]. The kesterite structures consist of layers arranged in a certain pattern: CuSn, CuZn, CuZn, and CuZn at $z=0, 1/2, 1/2,$ and $3/4$, respectively. The kesterite CZTS crystal has a tetrahedral bonding configuration, in which the anions and cations are arranged in a stacking pattern reminiscent of zinc blende structures such as ZnO or ZnS.

The exclusive distinction between the stannite and kesterite structures lies in the organization of the layers. The kesterite structure consists of alternating layers of ZnSn and Cu_2 , as previously indicated. Nevertheless, the arrangement of layers in the stannite structure varies [20]. The PMCA consists of two kesterite structures and one stannite unit cell, creating a singular and distinguishable arrangement. According to research, the kesterite structure of CZTS is more thermodynamically stable compared to the other two forms [21]. It has been chosen in preference to alternative constructions. Based on both theoretical and experimental evidence, it has been established that tetragonal kesterite has the most stable crystal structure for $\text{Cu}_2\text{ZnSn}(\text{S,Se})_4$ [22]. Aside from stannite, several other metastable structures have been shown, including Zinc blende, wurtzite, wurtzite-kesterite, and wurtzite-stannite (Figure.2.2).

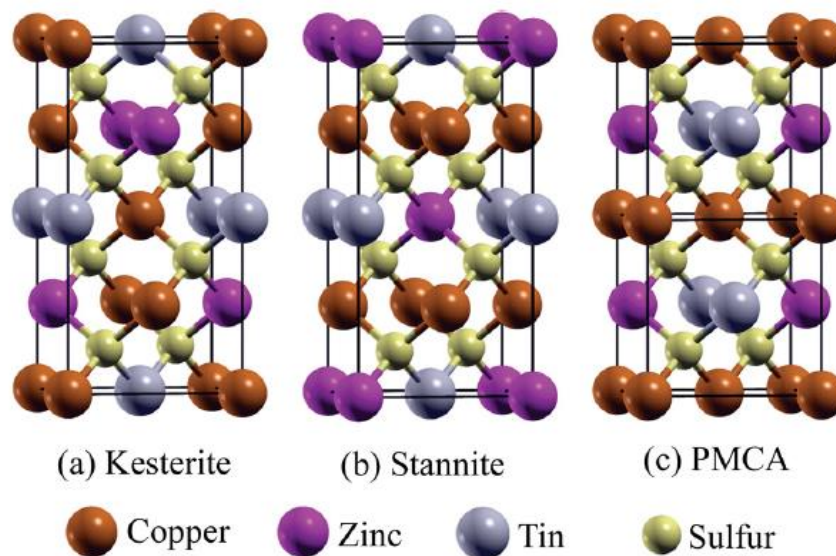


Figure 2.2 : a Kesterite, b Stannite and c PMCA structure of the CZTS material based on the different alternating planes[23].

2.3.2. The CZTS Phases

CZTS exhibits subsequent phases. The suggested chemicals are zinc sulfide and copper sulfide [24, 25]. The identification of the secondary phases is accomplished through the use of X-ray diffraction (XRD), microprobe fluorescence analysis, Raman spectroscopy, and X-ray absorption near-edge spectroscopy.

In zinc-rich structures, the significance of ZnS secondary phases is heightened due to their large formation energies. The presence of these secondary phases can influence the optical characteristics of the compound [26]. However, their existence may also limit the performance of the solar cell absorber layer. While empirical evidence supporting this claim is lacking, variations in band offsets with CZTS in different scenarios are possible.

When the band gap of the secondary phase is smaller than that of CZTS, both majority and minority carriers are attracted to it, posing challenges for carrier separation [27, 28]. This phenomenon could impede the efficient collection of hole-electron pairs. Conversely, if the band gap of the secondary phase exceeds that of CZTS, it not only reduces the conductivity of CZTS but also inhibits the formation of electron-hole pairs (Figure.2.3).

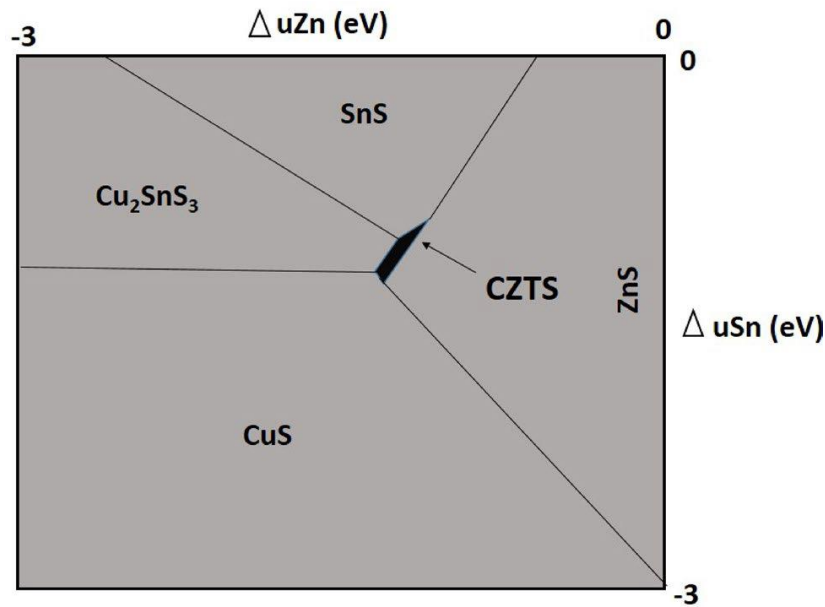


Figure 2.3: Secondary phase generation in the CZTS material [28].

Additionally, the process of synthesizing quaternary compounds is more intricate in order to prevent the formation of binary and tertiary phases. $\text{Cu}_2\text{ZnSnS}_4$ consists of four distinct elements and has the ability to form various more binary and ternary compounds, such as CuS , Cu_2S , ZnS , SnS , SnS_2 , and Cu_2SnS_3 . (Figure 2.4)

During the synthesis of $\text{Cu}_2\text{ZnSnS}_4$, heterocyclic compounds are formed when the composition percentage of any unidentified components increases or when there is a change in the growth environment.

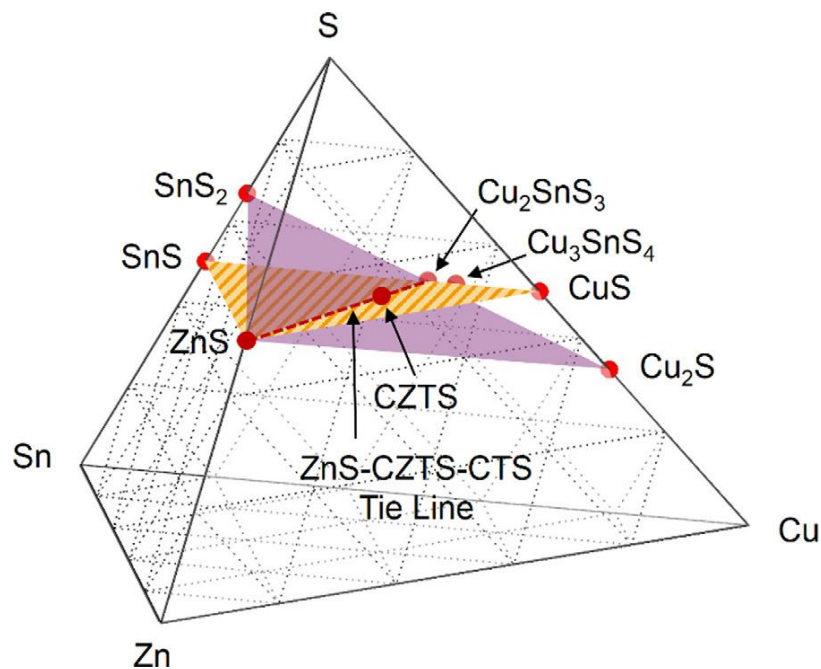


Figure 2.4: CZTS quaternary phase diagram containing the known phases [28].

Table 2.1: Different properties of secondary phases detected in CZTS materials [29]

Properties	$\text{Cu}_2\text{ZnSnS}_4$	Cu_2SnS_3	ZnS	Cu_2S	SnS_2
Band gap E_g	~1.45 eV	0.98-1.35 eV	3.54-3.68 eV	1.21 eV	2.2 eV
Electrical properties	Semiconductor, p-type	p-type	Semiconductor n-type	p-type, metal like, highly defective	n-type
Structural properties	Kesterite	Cubic and Tetragonal	Sphalerite and wurtzite	Chalcocite	Rhombohedral
Impact on solar cell performance	Essential absorbing material	Affect carrier collection efficiency	Insulating, reduce device active area	Metallic, short solar cell	n-type, forms diode and barrier for carrier collection

2.3.3. CZTS Defects

Aside from the secondary phases, PV solar cells can be influenced by various inherent point defects, including vacancy defects, antisite defects, interstitial defects, and complex defects, which have the potential to impact their performance. Among the most prevalent defects found in CZTS crystals are vacancies, with notable examples being the copper vacancy (V_{Cu}), zinc vacancy (V_{Zn}), tin vacancy (V_{Sn}), and sulfur vacancy (V_{S}). In addition, there are defects known as antisite defects, including the presence of Cu_{Zn} (copper on zinc antisite), Zn_{Cu} (zinc on copper antisite), Cu_{Sn} (copper on tin antisite), Sn_{Cu} (tin on copper antisite), Zn_{Sn} (zinc on tin antisite), and Sn_{Zn} (tin on zinc antisite). Other flaws that can be identified in CZTS are interstitials, notably copper interstitials (Cu_i) and zinc interstitials (Zn_i), as seen in Figure 2.14. Furthermore, there exist defect pair complexes that are balanced in charge and consist of vacancies for both donors and acceptors, as well as antisites and interstitial defects. The combinations include $[\text{Cu}_{\text{Zn}} + \text{Zn}_{\text{Cu}}]$, $[\text{Sn}_{\text{Zn}} + \text{Zn}_{\text{Sn}}]$, $[\text{Cu}_{\text{Sn}} + \text{Sn}_{\text{Cu}}]$, $[\text{Zn}_{\text{Sn}} + 2\text{Zn}_{\text{Cu}}]$, and $[2\text{Cu}_{\text{Zn}} + \text{Sn}_{\text{Zn}}]$. Additionally, there are other intricate abnormalities such as $[V_{\text{Cu}} + \text{Zn}_{\text{Cu}}]$, $[V_{\text{Zn}} + \text{Sn}_{\text{Zn}}]$, and $[2V_{\text{Cu}} + \text{Sn}_{\text{Zn}}]$. Defects in CZTS lead to the creation of several energy levels within the band gap. The levels consist of shallow acceptor and donor levels, a mid-gap level, and deep trap levels. Figures 2.5 and 2.6 depict the levels for CZTS [30-36].

V_{Cu} and Cu_{Zn} are both shallow acceptor levels, with Cu_{Zn} being deeper than V_{Cu} since its formation energy level is larger at 120 meV, compared to V_{Cu} is 20 meV. The abundance of V_{Cu} and Cu_{Zn} in CZTS results in a substantial population of hole carriers, leading to p-type conductivity. The performance of solar cells is improved based on the concentration of faults and the chemical

composition. More precisely, a copper-poor situation is defined as having a $\text{Cu}/\text{Zn}+\text{Sn}$ ratio of 1 or less, whereas a zinc-rich condition is defined as having a Zn/Sn ratio of 1 or greater. Higher composition ratios have a detrimental effect on the performance of CZTS by causing the formation of a large number of inherent defects and increasing losses due to recombination [38].

High energy production energies of 220 and 230 meV can be used to identify additional acceptor-level defects in CZTS, such as V_{Zn} and Zn_{Sn} , respectively. Cu_{Sn} exists in CZTS as many deep-level acceptors with formation energies that differ at the mid-gap level. In addition, it possesses a low formation energy and serves as recombination centers in CZTS, which has a detrimental effect on the efficiency of solar cells [37, 32, 39, 40]. Figure 2.5 depicts the main differentiation between CIGS and CZTS. More precisely, CZTS displays mid-gap states and tail states, but these states are not present in CIGS.

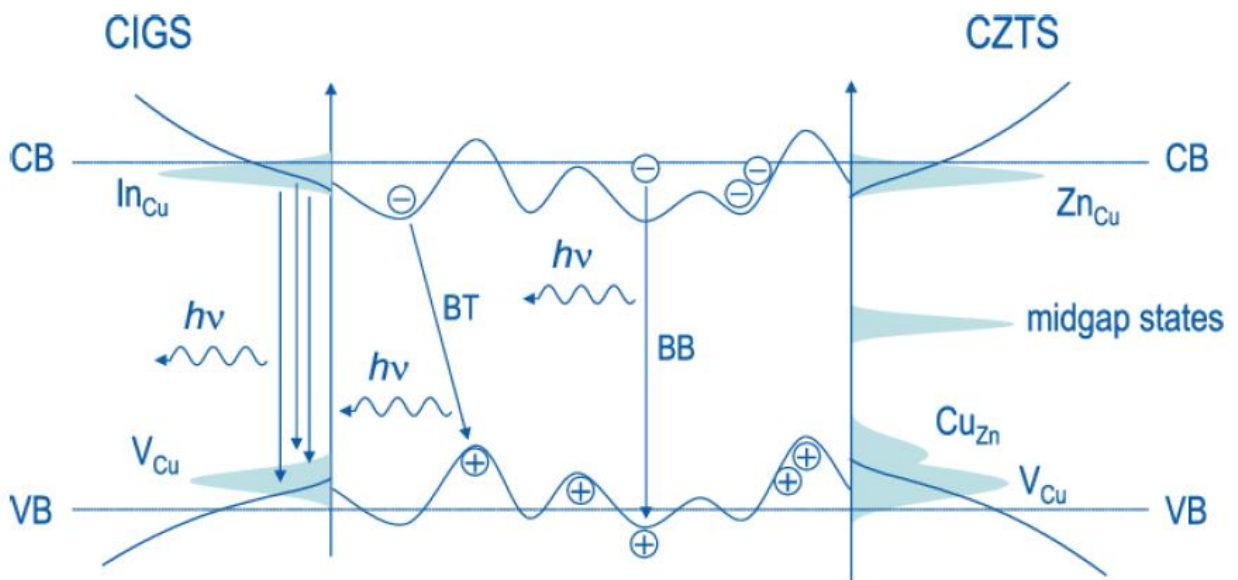


Figure 2.5: Different levels of defects present in both CIGS and CZTS materials [41].

However, there are other undesirable flaws, such as Zn_{Cu} , Sn_{Cu} , Sn_{Zn} , Cu_i , and Zn_i . All of these imperfections are classified as donor levels in the CZTS material. Zn_{Cu} is categorized as a shallow donor level, whilst the remaining ones are regarded as deep donor levels with a high formation energy [32]. Sn_{Cu} displays two discrete energy levels: a shallow donor level located in proximity to the conduction band, and a deep donor level positioned at the mid-gap energy level.

The elucidation of these energy levels can be achieved by examining the atomic orbital energies, particularly the multi-valence of Sn. Cu_i and Zn_i are categorized as a shallow donor level and two mid-gap levels, respectively. Moreover, Vanadium Sulfide (V_s) functions as a profound electron donor, leading to the formation of energy states located in the middle of the energy gap. However,

these flaws serve as sites where hole-electron couples can recombine, which has the potential to limit the performance of CZTS. This is seen in Figure 2.6 [42, 32].

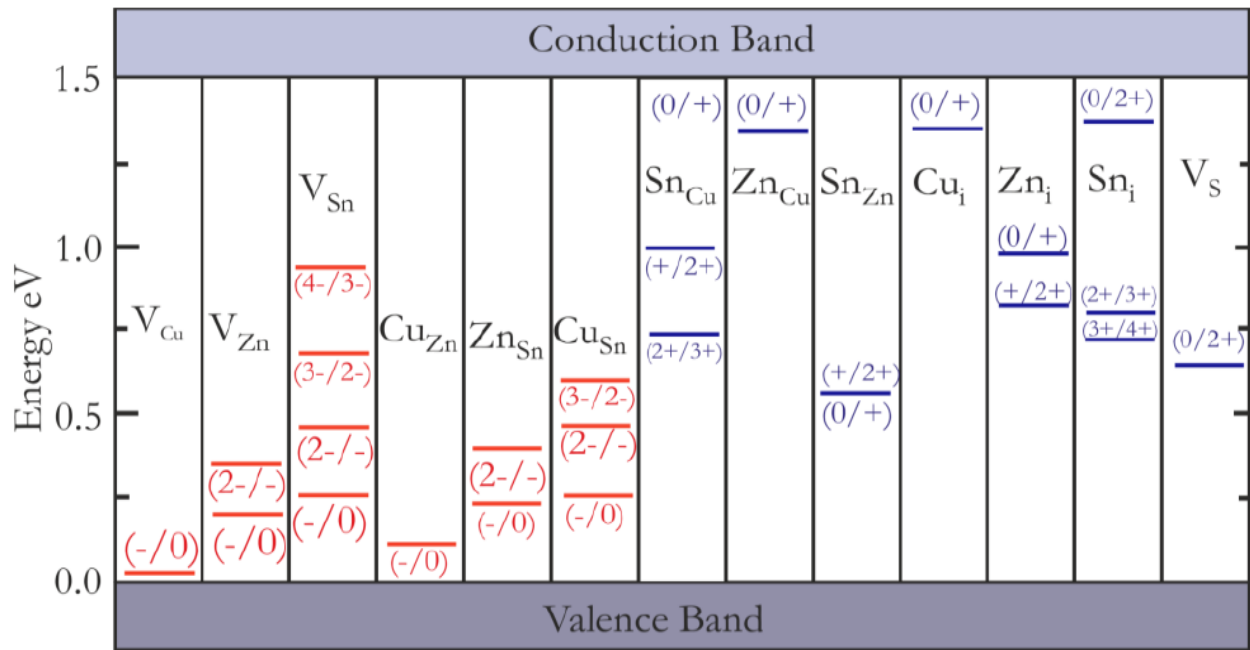


Figure 2.6: The energy levels at which intrinsic point defects arise in the band gaps of CZTS [32].

Defect complexes have a notable impact on the efficiency of CZTS solar cells, as illustrated in Figure 2.6. As an illustration, the compound $[Cu_{Zn} + Zn_{Cu}]$ exhibits the lowest energies for both shallow acceptors and donors, measuring at 200meV. This leads to a decrease in the band gap of CZTS. Conversely, the compounds $[Sn_{Zn} + Zn_{Sn}]$ and $[Cu_{Sn} + Sn_{Cu}]$ exhibit a significant formation energy exceeding 200 meV, resulting in a reduction of the band gap of CZTS by 300 meV. The intricate defect $[V_{Cu} + Zn_{Cu}]$ exhibits a low formation energy, yet it results in an augmentation of the band gap of CZTS [42]. The presence of antisite defect pairs in CZTS is not influenced by the chemical composition. Finally, the formation energy for the compounds $[V_{Zn} + Sn_{Zn}]$ and $[2Cu_{Zn} + Sn_{Zn}]$ is between 300 and 600 meV, as shown in Figure 2.7. The occurrence of these flaws in CZTS is influenced by the synthesis procedure, particularly by modifying the proportions of copper and zinc. These defects are observed during the synthesis of CZTS under conditions of copper deficiency and zinc excess. This phenomenon has been recorded in various studies, specifically studies [32, 43, 44, 45].

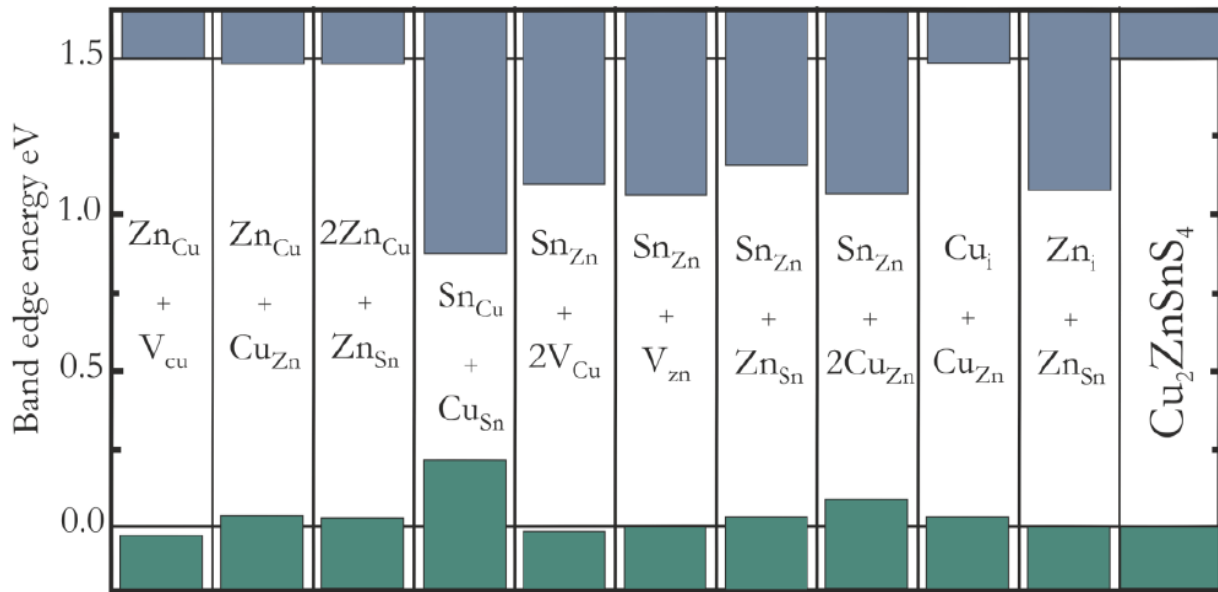


Figure 2.7: Different defect complexes change CZTS's valence (green) and conduction (blue) bands [32].

Nevertheless, it is evident that the existence of tin defects, both point and complex, results in an important increase in the formation energy, primary to a reduction in the energy band gap of CZTS. The significant formation energy of these defects renders them challenging to occur spontaneously. The formation energy of certain defects, such as $[2Cu_{Zn}+Sn_{Zn}]$, $[Sn_{Zn}+Zn_{Sn}]$, and $[Zn_{Sn}+2Zn_{Cu}]$, is measured at 600, 860, and 830 meV, respectively. In addition, there are other intricate defects with formation energies exceeding 1.2 eV, such for example $[Cu_{Sn}+Sn_{Cu}]$, $[Zn_{Sn}+Zn_i]$, $[V_{Zn}+Sn_{Zn}]$, and $[2V_{Cu}+Sn_{Zn}]$.

Table 2.2: Possible CZTS defects/complexes defects [29].

	Details of defects	Ionization levels (Donor/Acceptor)	Effect on CZTS solar cell Performance
Vacancies defect	Tin vacancy (V_{Sn})	One, Acceptor	Negatively impact the performance of the device, particularly at deep levels. Ionization from neutral to -1
	Zinc vacancy (V_{Zn})	Two, Acceptor	Unfavorable, profound depths
	Copper vacancy (V_{Cu})	Four, Acceptor	state and transition level, $\epsilon(-/0)$, creates shallow state, enhancing solar cell efficiency.
	Sulfur/Selenium vacancy (V_S/V_{Se})	One/One, Donor/Donor	unfavorable, mid gap states
Antisites defects	Copper-on-Zinc antisite (Cu_{Zn})	One, Acceptor	Deeper than copper vacancy, contribute to the p-type nature of CZTS
	Zinc-on-Copper antisite (Zn_{Cu})	One, Donor	Not favorable, shallow level near conduction band
	Copper-on-Tin antisite (Cu_{Sn})	Three, Acceptor	Not favorable, deep and multi Levels
	Tin-on-Copper antisite (Sn_{Cu})	Two, Donor	Not favorable, deep level/mid gas state
	Zinc-on-Tin antisite (Zn_{Sn})	Two, Acceptor	Not favorable, deep levels
	Tin-on-Zinc antisite (Sn_{Zn})	Two, Donor	Not favorable, mid gap states
Interstitials	Zinc interstitial (Zn_i)	Two, Donor	Not favorable, mid gap states
	Copper interstitial (Cu_i)	One, Donor	Not favorable, shallow states adjacent conduction band
Defect complexes	Non-stoichiometric-conserving defect complex ($V_{Cu}+Zn_{Cu}$), ($V_{Zn}+Sn_{Zn}$), ($Zn_{Sn}+2Zn_{Cu}$), ($2Cu_{Zn}+Sn_{Sn}$)	Formation energy $\sim 0.3-0.6$ eV	Significant impact and responsible for local variation in chemical potential and stoichiometric in-homogeneity
	Stoichiometric-conserving defect complex ($Cu_{Zn}+Zn_{Cu}$), ($Cu_{Sn}+Sn_{Cu}$), ($Zn_{Sn}+Sn_{Zn}$)	($Cu_{Zn}+Zn_{Cu}$): ~ 0.2 eV formation energy, for other two >0.2 eV	($Cu_{Zn}+Zn_{Cu}$): Low impact on optoelectronic properties other two have significant impact on CZTS and decrease band gap by 0.3 eV

2.3.4. Band Gap energy

The band structure of CZTS is contingent upon the diverse compositions of the materials within the compound. Additionally, the introduction of doping alters the energy band gap of the compound. Decreasing the Cu/(Zn+Sn) ratio causes the band energy of CZTS to increase [46]. Diverse energy bands are represented by distinct band structures. The transition from the Kesterite

structure to the stannite structure is accompanied by changes in the energy bands, as shown in Table 2.3.

Table 2.3: Band gap of CZTS/CZTSe simulated and measured experimentally.

Material	Energy Band (eV)	
	Simulated	Experimental
CZTSe kesterite	0.55 [18]	1.0 [27]
CZTS kesterite	0.87 [22]	1.5 [26]
CZTSe stannite	0.35 [28]	0.9 [12]
CZTS stannite	0.68 [47]	1.45 [27]
CZTSe stannite	0.35 [28]	0.9 [12]
CZTS PMCA	0.27 [14]	0.65 [14]

Theoretical calculations have revealed that the optical bandgap of stoichiometric kesterite-CZTS is 1.50 eV [15]. The experimental results showed that the bandgap of CZTS thin film, deposited using various methods, ranged from 1.4 eV to 1.5 eV [26, 27]. The CZTS thin film is well acknowledged to have an absorption coefficient of up to 10^4 cm^{-1} . The CZTS thin film produced using sol-gel synthesis in our research group has been found to exhibit an absorption coefficient above 10^4 cm^{-1} for photon energies above 1.2 eV.

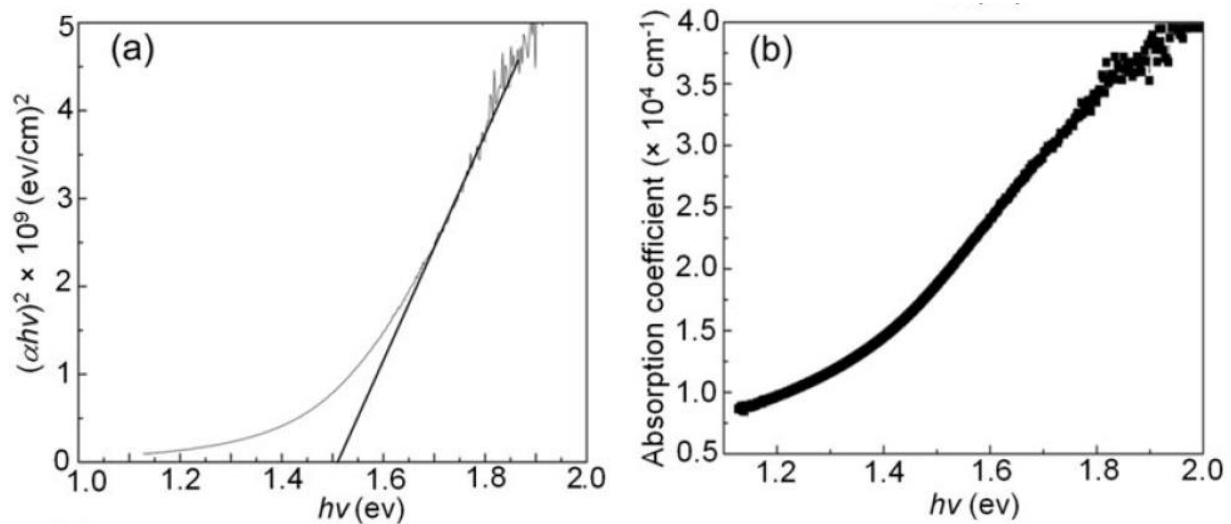


Figure 2.8: a) Typical band-gap and (b) Absorption coefficients of a CZTS thin film [90].

2.4. Deposition Techniques for CZTS

Various methods exist for the synthesis of CZTS materials. Researchers have been interested in the preparation of thin-film solar cell materials for over a decade. Various methodologies have been examined, empirically executed, and outcomes have been computed. The efficiency of CZTS

varies depending on the preparation method used. This section will cover various techniques for preparing CZTS materials.

There are two main methods when it comes to the processing of the material. [48].

1. Vacuum-based methods
2. Non-vacuum-based methods.

2.4.1. The Vacuum based methods

Vacuum-based methods are indeed costly, but they come with notable advantages. These processes yield materials with superior uniformity, resulting in exceptional quality. Moreover, they offer a high level of reproducibility. During these procedures, material compositions are deposited onto a substrate using various techniques, which will be elaborated on in the following section. By meticulously controlling pressure and temperature throughout the process, an optimal composition is maintained with high efficiency. Vacuum-based methods can be categorized as follows:

2.4.1.1. Evaporation techniques

Considering the high degree of achievement seen in the building of thin-film solar cell absorber films using the evaporation procedure, it is reasonable to select this method for preparing CZTS material. There are multiple methods available for evaporation. There are two approaches to accomplish the evaporation of the mixture. The first phase involves the simultaneous deposition of the components. Following the sulfurization process, the second phase of the procedure involves sequentially depositing the material compositions, which are then subjected to sulfurization. The precursor ingredients are deposited onto soda-lime glass (SLG). This process utilizes ethylene alcohol, copper (II) chloride dihydrate, zinc (II) chloride, tin (IV) chloride tetrahydrate ($\text{SnCl}_4 \cdot 4\text{H}_2\text{O}$), and thiourea ($\text{CH}_4\text{N}_2\text{S}$) [49]. The use of molybdenum (Mo) coated soda-lime glass has resulted in the highest efficiency ever achieved in CZTS solar cells. The evaporation rate remains efficient at 8.4%.

2.4.1.2. The Pulsed Laser Deposition technique (PLD)

Pulsed Laser Deposition (PLD) is a deposition technology that involves directing high-power laser pulses onto a solid state target in a vacuum chamber. This process is non-equilibrium in nature [13]. Laser ablation is a phenomena that occurs when a laser beam strikes a target. In this process, the target material absorbs the photons, which are usually millisecond UV pulses, through rapid interactions between photons and electrons. The energized electrons promptly (within a few picoseconds) transfer their energy to the lattice through phonon scattering, resulting in the eventual vaporization of the material as a partially ionized plasma. The interaction between the material and

the laser is highly intricate, and a comprehensive theory of plasma creation has not been established [50-53]. However, it is clear that it is not a straightforward process of evaporation. Yes, the plasma's effective temperature can exceed the boiling point of the target and typically ranges from 1 to 100 electron volts (eV), depending on the laser energy density and interaction characteristics. After its formation, the plasma rapidly spreads away from the target in a forward direction and ultimately reaches the substrate, where it is then deposited as a thin coating. The substantial kinetic energy exhibited by the atoms when they reach the substrate yields various advantageous outcomes on the formation of the film, rendering PLD a technology that operates outside of non-equilibrium technique.

2.4.1.3. Sputtering techniques

First described by Grove in 1852, this technique involves bombarding the surface of the target, which represents the material to be deposited (cathode), with non-reactive ions, typically argon ions (Ar^+). The sputtering effect mostly occurs when energy is transferred from the incident ions to the atoms on the surface of the blasted material. Surface atom removal is triggered when the amount of energy supplied above the binding energy of the atoms. The atoms that have been uninvolved gather and solidify onto a heated substrate, known as an anode, at a high temperature, resulting in the formation of a layer. The ions are generated in a plasma with the application of an electric discharge, either direct current (DC) or radiofrequency (R.F), at a low pressure range of 0.02-0.2 torr. This method enables the application of almost all types of materials (including semiconductors and insulators) to make thin films that have the same composition as the desired material. Additionally, it allows for the production of large-area deposits. Ito and Kanazawa [54] were the initial researchers to fabricate thin CZTS layers using this technique. They achieved a CZTS bandgap energy of 1.45 eV. Subsequently, Katagiri et al [55] discovered that immersing thin CZTS layers in demineralized water prior to depositing CdS enhances solar cell efficiency to 6.77%. In 2016, Yu-Pin Lin and colleagues [56] developed a solar cell using an SLG/Mo/CZTS/CdS/i-ZnO/IZO/Al structure. This solar cell achieved an efficiency of 5.2% when exposed to AM1.5 illumination. Recently, a group of researchers led by K. Sun et al [57] created a solar cell using a KS-CZTS material and a $\text{Zn}_{1-x}\text{Cd}_x\text{S}$ buffer layer composed of three elements. Their efficiency reached 9.2%, with the following current-voltage $I(V)$ characteristics: V_{oc} , J_{sc} , and FF, measuring 747.8 mV, 19.5 mA, and 63.2%, respectively.

2.4.2. A Non-vacuum-based methods

After extensive research and long-term application, it has been observed that vacuum processes are costly, complex, and do not optimally utilize composition materials. Given the rising demand for thin-film solar cells like CZTS, it became essential to explore more cost-effective and efficient production methods at an industrial scale. Consequently, non-vacuum processes have emerged as a superior alternative. These processes offer greater material utilization, require less energy, and incur lower costs compared to their vacuum counterparts. Additionally, the advantage of not requiring a vacuum environment makes non-vacuum processes especially beneficial for large-scale production.

The subsequent methods are employed in non-vacuum processes.

2.4.2.1. Spray pyrolysis methods

A precursor solution is made by combining elemental salts of copper, zinc, and tin. Subsequently, the solution is applied onto the substrate and subjected to precise thermal conditions. The temperature of the substrate is essential in determining the outcome of this operation. Excessive temperatures hinder the layer from sticking to the substrate surface, whilst excessively low temperatures can cause crystallization problems with the composition materials. The applied coating undergoes a desulfurization procedure utilizing hydrogen sulfide (H₂S) gas.

This method is straightforward and provides a high level of efficiency. Optimal optical characteristics are achieved by maintaining the substrate temperature within the range of 500–650 °C. No documented cases exist where CZTS generated using this technology has been utilized in thin-film solar cells.

2.4.2.2. Electrochemical deposition methods

Lately, electrochemical deposition techniques, also known as electro-deposition methods, have been extensively used for the fabrication of thin-film solar cell materials [58,59]. The initial semiconductor electrochemical deposition technique was performed almost forty years ago [60]. It employs two distinct methodologies. There are two methods for depositing the material: single-step deposition and sequential deposition. In this procedure, an aqueous solution electrode is immersed, with one serving as the anode and the other as the cathode. An electric potential is useful among the anode and cathode, resulting in the deposition of a layer onto the substrate. Prior to the procedure, the substrate undergoes a cleaning process, often followed by the application of a Mo coating onto the substrate. Electrodeposition is employed due to its superior material

utilization and precise process control. Additionally, this procedure becomes highly advantageous for extensive regions of sediment accumulation.

The first occurrence of CZTS manufacture using electrochemical deposition involved dissolving CuCl, SnCl, and ZnCl individually in NaOH and sorbitol, and thereafter depositing them in a sequential order. The maximum efficiency achievable for a solar cell using this specific approach is 6.03% [61]. Furthermore, in 2008, Bath University in Britain achieved the creation of CZTS with an efficiency of 0.8% [62,63], which was then enhanced to 3.2% in 2010 [64]. In 2009, Ennaoui at the Helmholtz-Zentrum Berlin (HZB) in Germany successfully attained an efficiency of 3.6% through the utilization of the electrochemical deposition method [65, 47].

2.4.2.3. Sol-gel deposition method

Despite being around for over 150 years, the sol-gel process has advanced significantly in the previous two decades. Before studying sol-gel chemistry, review certain definitions.

Sols are stable liquid colloidal suspensions. Solid particles, which are denser than liquid, must be small enough to prevent gravity from overwhelming dispersion forces.

Gels are stable, connected, three-dimensional solid networks extended in liquid. Colloidal gels have colloidal particles in their solid networks. Polymeric gels include sub-colloidal chemical units, such as macromolecules [66].

German auto rearview mirror manufacturer Schott Glaswerke filed the first Sol-Gel patent in 1939. Later patents covered various products, including cathode ray tube screen coatings that improved visual contrast. In 1981, Padua hosted the first international convention on glass and glass ceramics made from gels [67].

Sol-gelation, also known as solution-gelation, uses room-temperature chemical reactions like polymerization to solidify a liquid-phase precursor solution. The initial solution contains a precursor, alcohol solvent, water, and sometimes an acidic or basic catalyst. Measuring each component is crucial to the gel's properties. Precursor choice depends on intended material. Chemical properties of the precursor, the solution's major component, dictate solvent and catalyst choices [40].

The preparation room humidity and temperature, solution pH, catalyst properties, and deposition solution concentration control this process.

Various research groups have made efforts to create CZTS films using the sol-gel process, as documented in the literature. Agawane et al utilized the spin coating technique to create CZTS thin films. The purpose was to examine how the morphological, structural, and optical properties of

these films were affected by annealing temperatures ranging from 525 °C to 575 °C, while being exposed to an environment of H₂S gas. The CZTS absorber layer, which achieved an efficiency of 3.01%, underwent annealing at a temperature of 575 °C [68]. Yeh et al conducted a study where they synthesized CZTS thin films using copper chloride (II), zinc chloride (II), tin chloride (IV), and thiourea in a water-based solution. They also investigated the impact of annealing temperature, which varied from 160 °C to 320 °C [69].

Table 2.4: The efficiencies achieved by CZTS materials using various preparation methods

Preparation Methods of CZTS	Efficiency Recorded	Precursors	Years
Sputtering	6.77	Cu, SnS, ZnS	2008 [55]
Electrochemical deposition	3.14	Cu, Zn, Sn	2009 [25]
NP based methods	0.23	Copper(2) acetylacetonate, zinc acetate, tin(2) chloride dehydrate, elemental sulfur	2009 [70]
Screen Printing	0.49	CZTS microparticle	2010 [21]
CBD ion Exchange	0.16	tin chloride dehydrate, zinc acetate dehydrate, aqueous Cu ²⁺	2011 [71]
Electron beam deposition	5.43	Cu, Zn, and Sn	2011 [72]
Sol gel-based methods	2.23	Copper (2) acetate monohydrate zinc (2) acetate dehydrate tin (2) chloride dehydrate	2011 [49]
Pulsed laser deposition	3.14	in-house fabricated CZTS pellet	2011 [73]
Spray pyrolysis	1.15	-	2011 [74]
Ink based Fabrication	11	-	2012 [75]
Vacuum Sputtering	6.8	Cu ₂ , Zn, Sn, S ₄	2013 [76]
Rapid Thermal Annealing	2.56	Cu ₂ , Zn, Sn, S ₄	2014 [77]

2.5. Design of CZTS solar cell

CZTS has rapidly dominated thin-film solar cell research due to its outstanding photovoltaic properties. The thin-film solar cell is classified as a second-generation solar cell because of its polycrystalline/heterojunction structure [78,79]. The CZTS layer in thin-film solar cells functions as a p-type region. The CZTS material undergoes light absorption, resulting in the generation of electron-hole pairs. These pairs are then separated by the electric field at the junction. Periodically,

the basic architecture of the CZTS solar cell has undergone several enhancements in order to improve its overall efficiency (Figure 2.9).

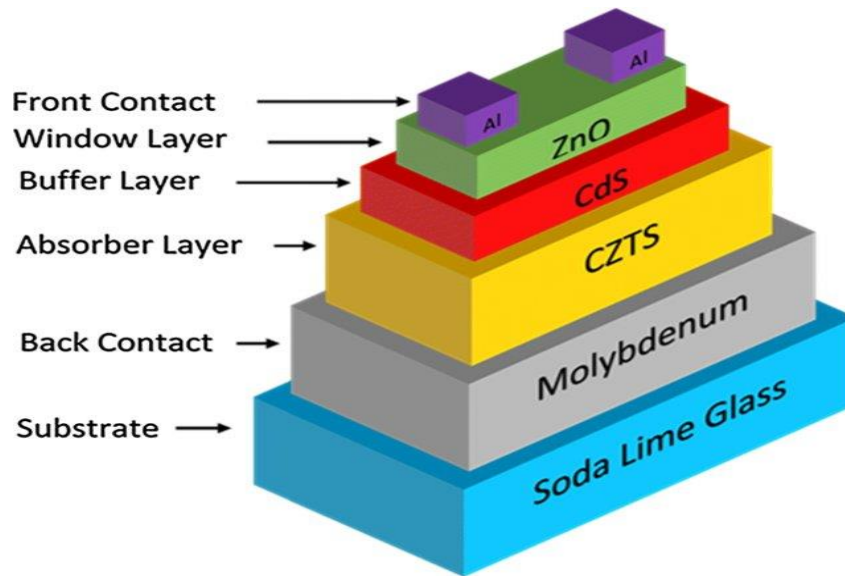


Figure 2.9: General structure of single-junction thin-Film CZTS solar Cell [80].

The provided design illustrates the fundamental framework of the solar cell [80]. Thin-film solar cells generally consist of five primary layers, as depicted in Figure 2.9. The absorbing layer, $\text{Cu}_2\text{ZnSnS}_4$ in this instance, is the most vital component of the photovoltaic cell. Its primary function is to absorb solar radiation and produce charge carriers, namely electrons and holes. The experiments and simulations are conducted using only sunlight as the primary source to determine the efficiency of the device (Figure 2.10).

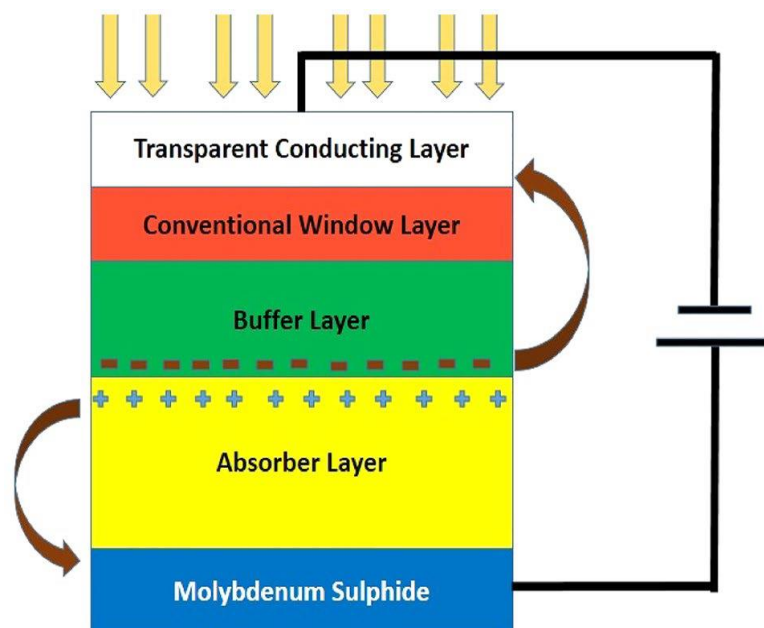


Figure 2.10: Transportation of electrons and holes in thin-film solar cells constructed from CZTS [80].

2.5.1. Anti-reflecting layer

Traditional glasses are efficient transparent barriers that facilitate the passage of light. However, in the context of solar applications, it is imperative to have an antireflection layer that also exhibits conductivity. The anti-reflective characteristic is crucial for minimizing the energy loss of photons (reflected photons), hence enhancing the generation of electron-hole pairs. In addition, the layer must have conductivity to collect the electrons generated in the pn-junction. As the number of electrons in the system rises, the short-circuit current will also increase. ITO is a highly commendable option for an anti-reflective coating. The layer possesses both transparency and conductivity. The material qualities are suitable for use in the solar cell. Indium tin oxide is a binary chemical consisting of tin and indium. The material is a doped n-type material with a band gap of 4 electron volts (eV), which means that it absorbs very little light in this layer [81,82]. One advantage of the ITO compared to its competitors is its superior production capability. It demonstrates a lower temperature at which it may be deposited and has desirable features for etching. In addition, ITO demonstrates decreased series resistance, which enables unimpeded electron mobility.

Aluminum Zinc Oxide is a type of Transparent Conductive Oxide (TCO) material that has applications in solar cells. It exhibits high electrical conductivity and allows the transmission of a broad spectrum of light [83]. However, ITO is still the preferred choice due to its superior conductivity compared to AZO and its ability to resist degradation when exposed to the external environment [84]. However, in terms of cost, ITO is generally more expensive than AZO.

2.5.2. The Window layer

Beneath the anti-reflection layer, there is a layer called the window layer. The material exhibits n-type conductivity and possesses both transparency and electrical conductivity. It is imperative that no obstruction is present to allow the passage of light to the PN junction. In summary, the material must possess a band gap that exceeds the energy range of visible light. This layer, which functions as a transparent barrier, is commonly referred to for example the window layer. The surface of the absorber layer in CZTS solar cells is predominantly rough, primarily as a result of sulfurization. The surface's roughness increases the possibility of direct contact among the TCO and absorber layer, resulting in significant band incoherence and a decrease in the pen circuit voltage of the device [85]. In order to bypass this issue, an additional layer of glass is inserted between the layer that conducts electricity and the layer that absorbs light. Optimizing the layer is necessary to enhance the efficiency of the solar cell.

The thickness is crucial. Increasing the thickness results in a decrease in series resistance and an increase in conductivity, which is advantageous. However, excessive increase in thickness may result in a higher absorption of light within this layer [86]. Conversely, an excessive number of thin layers will result in a high level of band discontinuity, while a layer that is too thick will disrupt the built-in field, preventing the efficient collection of electron-hole pairs. The parameter utilised to assess the performance of the windows layer or determine its appropriateness as a windows layer is defined by the ratio of conductivity to absorption. Performance improves as the ratio increases. Furthermore, the analysis takes into account factors such as work functions, thermal stability, homogeneity, corrosiveness, and other relevant factors (Figure 2.11).

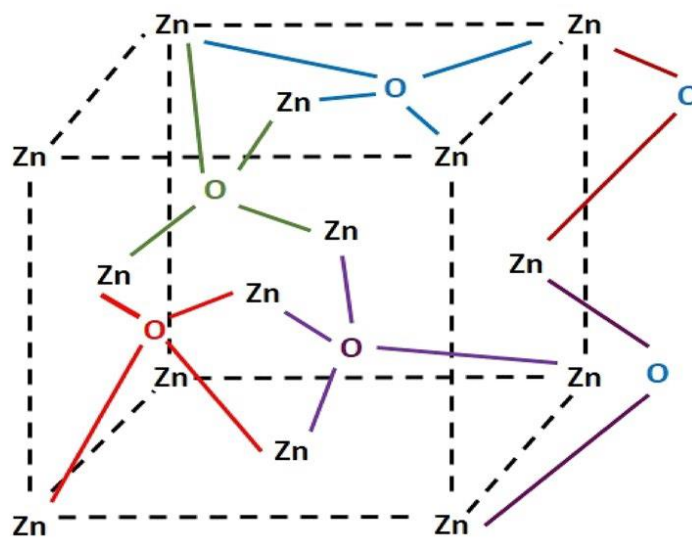


Figure 2.11: CZTS thin-film solar cells use Zinc Oxide's crystal structure as a resistive layer[85].

Zinc Oxide is the conventional material used as a window layer in thin-film solar cells. This material exhibits a high degree of light scattering. Photons effectively reach the absorber layer. The resistivity of the i-ZnO material is determined to be $(1.5-2.0) \times 10^4$ per cm. The material demonstrates Hall mobilities reaching up to $60 \text{ cm}^2/\text{Vs}$, approximately 2.0 refractive indices, and a typical transmittance of 85%. The band gap of i-ZnO is in the range of 3.35–3.45 eV. Due to its favorable characteristics, it is highly suitable for utilization as the windows layer in thin-film solar cells, as well as in CZTS solar cells.

2.5.3. The buffer layer

The buffer layer, also known as the emitter layer, has a significantly smaller thickness compared to the absorbing layer, usually designed to be approximately 40-50 nm. The purpose of this is to establish the p-n junction and facilitate the separation of charges. Recombination occurring at the

interface between the absorber and buffer layers has been recognised as a major cause of loss in CZTS solar cells. This is due to the relatively long lifetime of charge carriers in the CZTS absorber[83], which can extend up to a few nanoseconds. The recombination rate at the interface in a CZTS cell has been quantified to be roughly 10^5 cm/s.

Cadmium sulphide (CdS) is frequently employed as the buffer layer due to its superior suitability for CIGS cells, which have been extensively utilised in the construction of CZTS cells. The large energy gap of CdS allows for efficient passage of light to the absorbing layer [85], and cadmium atoms have been shown to deactivate flaws at the interface between the absorber and buffer layers. Typically, the bandgap at the interface between CZTS and CdS is reduced due to the presence of localised states, which results in an increase in the valence band maximum in CZTS[87]. This phenomenon is responsible for the prevalence of interface recombination in CZTS solar cells.

Additional materials that have been effectively utilised as buffer layers in conjunction with CZTS include CeO₂[87], In₂S₃[88], InS₂[89], TiO₂, a-Si[90], ZnO[91], ZnS[92], and Zn_{1-x}Cd_xS[93].

Table 2.5: Possible buffer layer materials that can be utilized taking into account their band gap [93].

Buffer layer material	Band Gap (eV)	Electron Affinity (eV)
ZnO	3.3	4.6
ZnS	3.5	4.5
ZnSe	2.9	4.1
CdS	2.4	4.2
Cd _{0.4} Zn _{0.6} S	2.98	4.2
In ₂ S ₃	2.8	4.7
Zn ₁ MgO	3.32- 3.65	4.53-4.21

Due to the myriad detrimental effects, it became imperative to find a substitute for CdS. Zinc sulphide (ZnS) was determined to be a feasible substitute. Zinc sulfide (ZnS) benefits from an abundant availability of raw materials, leading to a comparatively reduced cost. Moreover, the substance is non-toxic, thus it does not present any danger to the environment. As toxicity is not present, the cost of packaging decreases. The material has a band gap ranging from 3.10 to 3.40 eV, which is greater than that of CdS. A larger band gap facilitates the transmission of a higher quantity of photons towards the junction. Increasing the band gap of the solar cell also improves its blue response, thereby enhancing its efficiency. Zinc sulfide (ZnS) demonstrates a higher level of lattice matching with copper zinc tin sulfide (CZTS), which consequently leads to an improvement in efficiency [91]. Experimental results have demonstrated that reducing the thickness of the buffer layer enhances the efficiency of the solar cell during the optimization

process. This phenomenon occurs because a thinner buffer layer enables a larger quantity of photons to generate a greater quantity of electron-hole pairs in the junction. Figure 2.12.

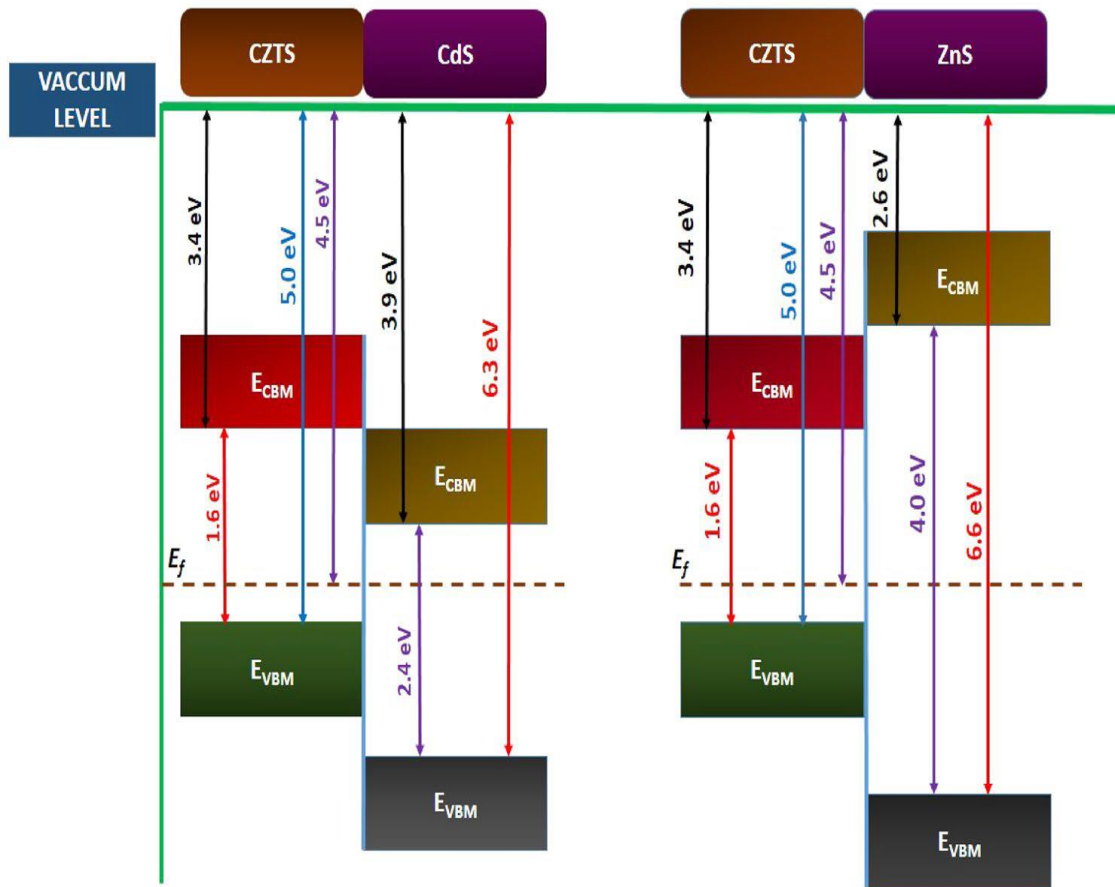


Figure 2.12: Band-to-band comparison of ZnS and CdS, the best communal buffer layer materials, with CZTS [93].

The other alternative buffer layers include In₂S₃, SnS₂, and ZnSe. Experimental observations have shown that ZnS is the most effective buffer layer [88],[89]. The primary reason for the recent preference of thinfilm CZTS solar cell developments is its stability at higher temperatures and its efficiency. This is supported by Figures 2.13 and 2.14, as well as Table 2.6.

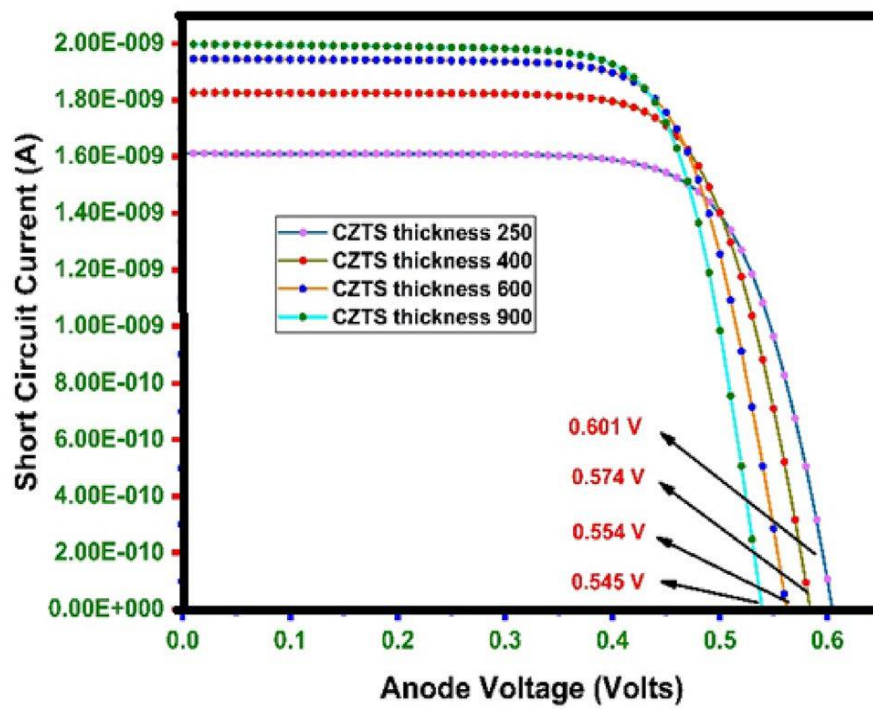


Figure.2.13 I-V characteristics of simulated CZTS solar cells with varying absorber layer thicknesses[93].

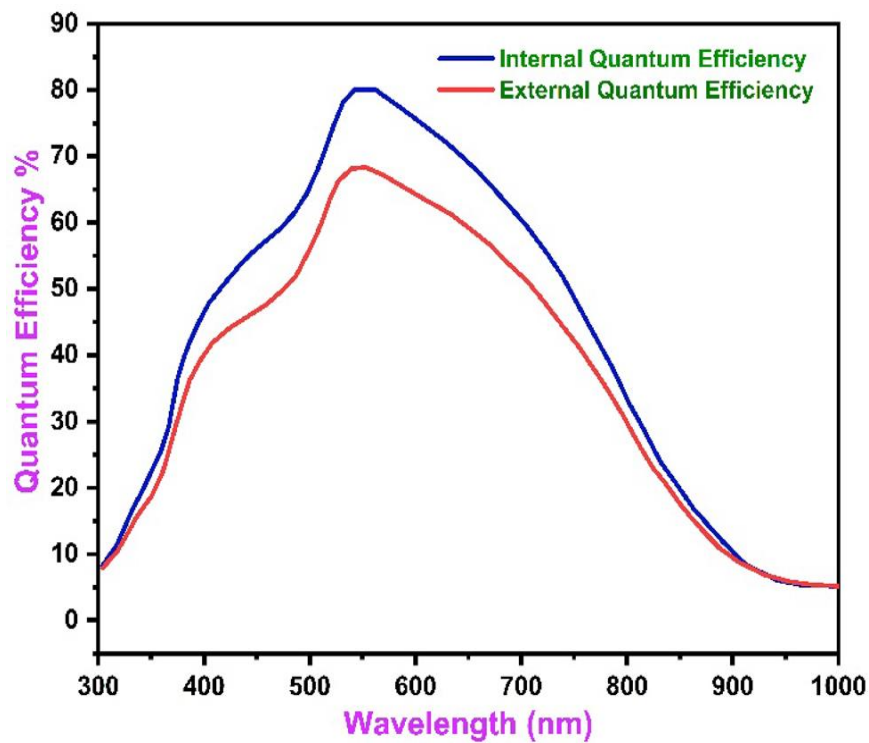


Figure 2.14: Efficiency analysis of the simulated thin-film CZTS solar cell, considering both external and internal factors [93].

Table 2.6: Efficiency attained employing diverse buffer layers in CZTS solar cell[93]

Buffer layer material	Conduction Band Offsets(eV)	Valance Band Offsets(eV)	E_v of Buffer layer (eV)	Efficiency of the device (%)
CdS	0.1-0.40	1-1.30	2.31	8.77
ZnO	0.09	+1.78	3.37	-
CeO2	-0.12	+1.919	3.3	6.6
ZTO	0.3		3.8-4	5.4
ZnS	0.86	-	-	2.87
$Zn_{1-x}Sn_xO_y$	-	-	-	9.0
$Zn_{1-x}Cd_xS$	0.37	-0.83	2.7	9.2
In2S3/CdS	-	-	-	6.62

2.5.4 Back contact

The primary function of the back contact is to establish optimal contact with the absorber layer, thereby facilitating efficient hole transmission. Therefore, it is essential to select a material that possesses the appropriate work function, band gap, and lattice constant. Problems like cracking, bulking, bubbling, and pinhole development in the back contact of the device have been identified as factors that reduce its performance [94–96]. The diminished efficacy of the solar cells can be attributed to mechanical stresses caused by various deposition techniques and the difference in thermal expansion between CZTS and the material used for the back contact. Moreover, the dispersion originating from both the layer that absorbs and the underlying material can also contribute to the identical outcome. Molybdenum is the preferred material for the rear contact of CZTS solar cells because of its favorable work function and band gap [97]. An inherent issue with molybdenum is that, during the desulfurization process, it undergoes a reaction with sulfur, resulting in a decrease in the effective thickness of molybdenum disulfide. An additional concern arises from the chemical interaction between sulphur (Su) and molybdenum disulfide (MoS_2). The performance parameters of the solar cell have been assessed by replacing molybdenum with other materials. Recent endeavors have been made to address the concerns associated with the back contact. A buffer layer is deposited between CZTS and MoS_2 to inhibit any chemical reaction between the absorber and the back contact material [98]. According to reference [99], AZO is the favored option for an intermediate layer.

2.6. Interface Buffer /Absorber layer

The electrical characteristics of the solar cell are significantly impacted by the band alignment between the buffer layer and absorber layer. The CIGS/Se structure exhibits superior current properties compared to the CZTS/Se configuration, primarily due to less interface recombination. The conduction band offset is essential in easing electron movement through layers and regulating

the recombination process at the interface. The band offset in a hetero-junction is determined by the variance in electron affinities between the two layers of materials. The presence of positive and negative band offsets results in the construction of two distinct structures: a cliff and a spike. The CZTS material has a higher electron affinity than CdS, making it the preferred option as a buffer layer because of its superior routine characteristics. By way of a result, a steep cliff-like structure forms at the hetero-junction of the solar cell [100]. The presence of this unwanted precipice-like structure at the intersection impedes the flow of electrons from the absorber to the buffer layer, preventing any loss due to recombination. Furthermore, the junction experiences electron accumulation, leading to the recombination of the prevailing carriers (holes) and electrons. The process of recombination decreases the short-circuit current, hence impacting the overall efficiency of the solar cell. Therefore, in order to enhance the conduction band offset, band engineering is employed at the junction of CZTS/CdS to create a spike-like structure. The decrease in recombination is a result of the positive band offset, which functions as a barrier for electrons. This barrier prevents the accumulation of electrons in the junction [101]. To achieve maximum efficiency in electron conduction, it is desirable to have a conduction band offset (CBO) in the range of +0.3 eV to +0.5 eV. A conduction band offset (CBO) greater than 0.5 electron volts (eV) prevents the entrance of electrons, while a CBO lower than 0.3 eV reduces efficiency because of the presence of a steep structure [102]. Utilizing front band grading can be used to address the CBO problem. The bandgap property of the compound CZTS can be adjusted by employing the distinct components of the material, hence achieving a graded bandgap. Substituting Sulphur with Selenium leads to a reduction in the bandgap from 1.5 to 0.9 eV. However, it also diminishes the substance's electron affinity.

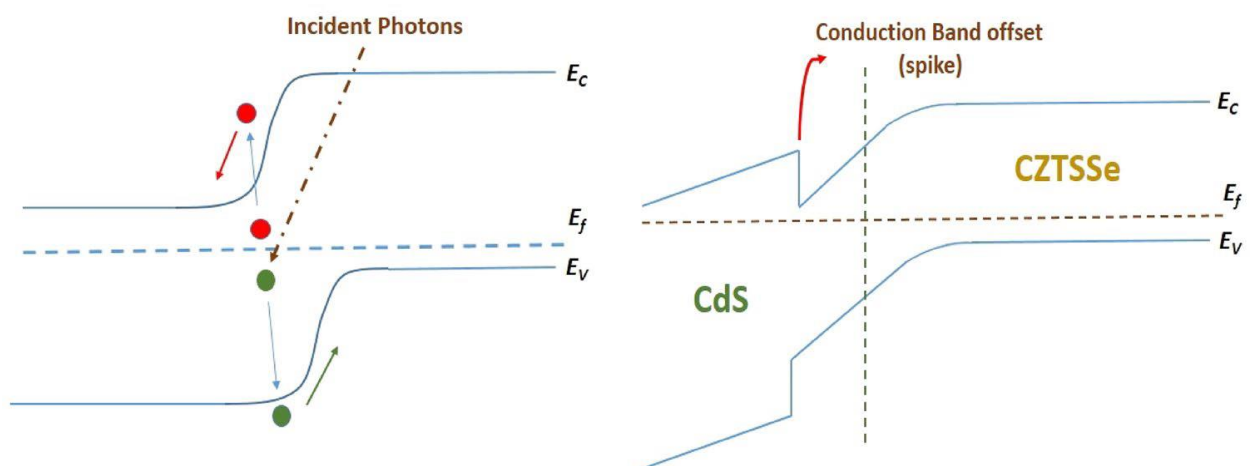


Figure 2.15: Band alignment of buffer layer in CZTS solar cells compared with and without a spike-like structure in junction CdS/CZTSSe [100].

Another possible method involves inserting an intermediary layer between the absorber and buffer layer, serving as a connecting bridge between the two. The presence of a band gap and electron affinity in this layer is necessary in order to generate spike-like formations with both layers. The fundamental reason for the low efficiency of the CZTS/Se solar cell is its lower open-circuit voltage. The problems related to the open-circuit voltage of the device can be handled by enhancing the band alignment in the hetero-junction between the absorber and buffer layer.

2.7. Prospects for CZTS solar cell in the future

Recent developments in solar cell research have led to the emergence of CZTS as a promising option for minimizing material usage and assuring consistent performance. Because of its high thin-film efficiency in capturing abundant light, this second-generation substance can be employed as a transparent solar cell. This application is frequently observed in translucent electric car roofs and construction materials. Nevertheless, the CZTS layer's high hole mobility makes it an ideal candidate for the Hole Transport Layer (HTL) in third-generation Perovskite solar cells. Because of its cost-effectiveness and non-toxic nature, it can be used as a replacement for the HTL and improve the stability of the device. Furthermore, the incorporation of CZTS nano-particles as an additive to the absorber material in solar cells has demonstrated significant efficacy. This has the capacity to improve the optical and electrical characteristics of the absorber, hence leading to improved performance of the solar cell. There exist numerous unknown domains within the field of solar cell research, in which CZTS has the potential to significantly augment the efficiency of the device. Undoubtedly, this topic holds substantial potential for the future if we can evaluate it.

2.8. Conclusion

In this chapter, a brief overview of the technology of solar cells based on kesterite materials CZTS has been presented. The properties and electronic characteristics of the absorber material CZTS have been explained. We introduced the cell structure based on the kesterite absorber material CZTS, and defined the band structure at the absorber/buffer layer interface. Additionally, we mentioned some techniques used in the elaboration of kesterite materials.

References

- [1] Su, Z.H.; Liang, G.X.; Fan, P.; Luo, J.T.; Zheng, Z.H.; Xie, Z.G.; Wang, W.; Chen, S.; Hu, J.G.; Wei, Y.D. Device post annealing enabling over 12% efficient solution-processed $\text{Cu}_2\text{ZnSnS}_4$ solar cells with Cd^{2+} substitution. *Adv. Mater.* 2020.
- [2] Kumar et al., « Strategic review of secondary phases, defects and defect-complexes in kesterite CZTS–Se solar cells ». *Energy Environ. Sci.* 2015.
- [3] Chen S, Walsh A, Gong XG, Wei SH. Classification of lattice defects in the kesterite $\text{Cu}_2\text{ZnSnS}_4$ and $\text{Cu}_2\text{ZnSnSe}_4$ earth-abundant solar cell absorbers. *Adv Mater.* 2013 Mar 20;
- [4] Katagiri, H., Jimbo, K., Moriya, K., Tsuchida, K.: *Solar cell without environmental pollution by using CZTS thin film*. In: Proceedings of the 3rd World conference on photovoltaic energy conversion, Osaka, pp. 287432879 (2003)
- [5] Shin, B., Gunawan, O., Nestor, Y.Z., Bojarczuk, A., Chey, S.J., Guha, S.: *Thin film solar cell ith 8.4 % power conversion efficiency using an earth-abundant $\text{Cu}_2\text{ZnSnS}_4$ absorber*. *Prog. hotovoltaics Res. Appl.* 21, 72376 (2013)
- [6]] Giraldo S, Jehl Z, Placidi M, Izquierdo-Roca V, Pérez-Rodríguez A, Saucedo E. Progress and Perspectives of Thin Film Kesterite Photovoltaic Technology: A Critical Review. *Adv Mater.* 2019.
- [7] S.A. Khalate, R.S. Kate, R.J. Deokate, A review on energy economics and the recent research and development in energy and the $\text{Cu}_2\text{ZnSnS}_4$ (CZTS) solar cells: A focus towards efficiency, *Solar Energy*, Volume 169, 2018.
- [8]. Ravindiran M and Praveenkumar, Status review and the future prospects of CZTS based solar cell—A novel approach on the device structure and material modeling for CZTS based photovoltaic device, *Renew. Sustain. Energy Rev.* 94 317–29 (2018)
- [9]. Shah, Usman, Ao Wang, Muhammad Ullah, Muhammad Ishaq, Imtiaz Shah, Yiyu Zeng, Misbah Abbasi, et al. 'A Deep Dive into $\text{Cu}_2\text{ZnSnS}_4$ (CZTS) Solar Cells: A Review of Exploring Roadblocks, Breakthroughs, and Shaping the Future'. *Small* 20 (March 2024): e2310584.
- [10]. E. Indubala, V. Sudha, S. Sarveshvaran, S. Harinipriya, A.Y. Mamajiwala, *Unusual composition of CZTS: elemental sulfurization and solution method*. *Mater. Today Proc.* **8**, 393– 401 (2019).
- [11]. J. A. Okwako, "Optical and electrical characterization of $\text{Cu}_2\text{ZnSnS}_4$ deposited by Silar technique." A research Master of science degree in physics, University of Nairobi, 2018.
- [12]. A. Benami, *Effect of CZTS parameters on photovoltaic solar cell from numerical simulation*. *J. Energy Power Eng.* **13**(1), 32–36 (2019).
- [13]. X. Song, X. Ji, M. Li, W. Lin, X. Luo, H. Zhang, *A review on development prospect of CZTS based thin film solar cells*. *Int.J. hotoenergy* **2014**, 1–11 (2014).
- [14].S.H. Zyoud et al., *Numerical modeling of high conversion efficiency FTO/ZnO/CdS/CZTS/MO thin film-based solar cells: using SCAPS-1D software*. *Crystals* **11**(12), 1468 (2021).
- [15]. N.A. Bakr, S.A. Salman, S.A. Hameed, *Deposition and characterization of $\text{Cu}_2\text{ZnSnS}_4$ thin films for solar cell applications*. *Int. J. Tech. Res. Appl.* e-ISSN 2320-8163 **13**(6), 3379–3388 (2018)
- [16]. S. Padhy, R. Mannu, U.P. Singh, *Graded band gap structure of kesterite material using bilayer of CZTS and CZTSe for enhanced performance: a numerical approach*. *Sol. Energy* **216**(2020), 601–609(2021).
- [17]. N. Kattan, B. Hou, D.J. Fermín, D. Cherns, *Crystal structure and defects visualization of $\text{Cu}_2\text{ZnSnS}_4$ nanoparticles employing transmission electron microscopy and electron diffraction*. *Appl. Mater. Today* **1**(1), 52–59 (2015).

- [18]. S. Jain, P. Chawla, S.N. Sharma, D. Singh, N. Vijayan, *Efficient colloidal route to pure phase kesterite Cu_2ZnSnS_4 (CZTS) nanocrystals with controlled shape and structure*. Superlattices Microstruct. **119**, 59–71 (2018).
- [19]. R. Article, S. Ikeda, *Copper - based kesterite thin films for photoelectrochemical water splitting*. High Temp. Mater. Proc.. (2021).
- [20]. J. Paier, R. Asahi, A. Nagoya, G. Kresse, *Cu_2ZnSnS_4 as a potential photovoltaic material: a hybrid Hartree-Fock density functional theory study*. Phys. Rev. B **79**(11), 115126 (2009).
- [21]. A. Sharmin, M.S. Bashar, M. Sultana, S.M.M. Al Mamun, *Sputtered single-phase kesterite Cu_2ZnSnS_4 (CZTS) thin film for photovoltaic applications: post annealing parameter optimization and property analysis*. AIP Adv. (2020).
- [22]. M. Kumar, C. Persson, *Cu_2ZnSnS_4 and $Cu_2ZnSnSe_4$ as potential earth-abundant thin-film absorber materials: a density functional theory study*. Int. J. Theor. Appl. Sci. **5**(1), 1–8 (2013)
- [23] A. Khare; B. Himmetoglu; M Johnson; D. J. Norris; M. Cococcioni; E. S. Aydil , *Calculation of the lattice dynamics and Raman spectra of copper zinc tin chalcogenides and comparison to experiments* J. Appl. Phys. **111**, 083707 (2012).
- [24]. J. Just, C.M. Sutter-Fella, D. Lützenkirchen-Hecht, R. Frahm, S. Schorr, T. Unold, *Secondary phases and their influence on the composition of the kesterite phase in CZTS and CZTSe thin films*. Phys. Chem. Chem. Phys. **18**(23), 15988–15994 (2016).
- [25]. A. Aldalbahi, E.M. Mkawi, K. Ibrahim, M.A. Farrukh, *Effect of sulfurization time on the properties of copper zinc tin sulfide thin films grown by electrochemical deposition*. Sci. Rep. **6**(1), 32431 (2016).
- [26].O. Cu *et al.*, “Secondary Crystalline Phases Influence on Optical,” vol. 4, pp. 1–14, 2020.
- [27]. W. Bao, M. Ichimura, *Influence of secondary phases in kesterite- Cu_2ZnSnS_4 absorber material based on the first principles calculation*. Int. J. Photoenergy (2015).
- [28] C. Platzer-Björkman, J.K. Larsen, N. Saini, M. Babucci, N. Martin, *Ultrathin wide band gap kesterites*. Faraday Discuss. (2022).
- [29] Tian, Qingwen, et Shengzhong (Frank) Liu. « Defect suppression in multinary chalcogenide photovoltaic materials derived from kesterite: progress and outlook ». Journal of Materials Chemistry A **8**, no 47 (2020): 24920–24924.
- [30].Nagoya, A., et al., *Defect formation and phase stability of Cu_2ZnSnS_4 photovoltaic material*. Physical Review B, 2010. **81**(11).
- [31] Kumar, M., et al., *Strategic review of secondary phases, defects and defect-complexes in kesterite CZTS-Se solar cells*. Energy & Environmental Science, 2015.
- [32]. Chen, S., et al., *Classification of Lattice Defects in the Kesterite Cu_2ZnSnS_4 and $Cu_2ZnSnSe_4$ Earth-Abundant Solar Cell Absorbers*. Advanced Materials, 2013. **25**(11): p. 1522-1539.
- [33]. Chen, S.Y., et al., *Defect physics of the kesterite thin-film solar cell absorber Cu_2ZnSnS_4* . Applied Physics Letters, 2010. **96**(2): p. 3.
- [34]. Yu, K. and E.A. Carter, *Determining and Controlling the Stoichiometry of Cu_2ZnSnS_4 Photovoltaics: The Physics and Its Implications*. Chemistry of Materials, 2016. **28**(12): p. 4415-4420.
- [35]. Romero, M.J., et al., *A Comparative Study of the Defect Point Physics and Luminescence of the Kesterites Cu_2ZnSnS_4 and $Cu_2ZnSnSe_4$ and Chalcopyrite $Cu(In,Ga)Se_2$* . 2012 38th IEEE Photovoltaic Specialists Conference (PVSC), 2012: p. 3349-3353.
- [36]. Azimi, H., Y. Hou, and C.J. Brabec, *Towards low-cost, environmentally friendly printed chalcopyrite and kesterite solar cells*. Energy & Environmental Science, 2014. **7**(6): p. 1829-1849.

- [37]. Chen, S., et al., *Crystal and electronic band structure of $\text{Cu}_2\text{ZnSnX}_4$ ($X=\text{S}$ and Se) photovoltaic absorbers: First-principles insights*. Applied Physics Letters, 2009. **94**(4).
- [38]. Yeh, M., C. Lee, and D. Wu, *Influences of synthesizing temperatures on the properties of $\text{Cu}_2\text{ZnSnS}_4$ prepared by sol-gel spin-coated deposition*. Journal of Sol-Gel Science and Technology, 2009. **52**(1): p. 65-68.
- [39]. Biswas, K., S. Lany, and A. Zunger, *The electronic consequences of multivalent elements in inorganic solar absorbers: Multivalency of Sn in $\text{Cu}_2\text{ZnSnS}_4$* . Applied Physics Letters, 2010. **96**(20).
- [40]. Tanaka, K., et al., *$\text{Cu}_2\text{ZnSnS}_4$ thin film solar cells prepared by non-vacuum processing*. Solar Energy Materials and Solar Cells, 2009. **93**(5): p. 583-587.
- [41]. Romero, M.J., et al., *Comparative study of the luminescence and intrinsic point defects in the kesterite $\text{Cu}_2\text{ZnSnS}_4$ and chalcopyrite $\text{Cu}(\text{In,Ga})\text{Se}_2$ thin films used in photovoltaic applications*. Physical Review B, 2011. **84**(16)
- [42]. Huang, D. and C. Persson, *Band gap change induced by defect complexes in $\text{Cu}_2\text{ZnSnS}_4$* . Thin Solid Films, 2013. **535**: p. 265-269.
- [43] Kumar, M., et al., *Strategic review of secondary phases, defects and defect-complexes in kesterite CZTS-Se solar cells*. Energy & Environmental Science, 2015
- [44]. Poornima, N., et al., *Defect Analysis Of CZTS Thin Films Using Photoluminescence Technique*. Solid State Physics, Vol 57, 2013. **1512**: p. 464-465.
- [45]. Chen, S. Y., et al., *Intrinsic point defects and complexes in the quaternary kesterite semiconductor $\text{Cu}_2\text{ZnSnS}_4$* . Physical Review B, 2010. **81**(24).
- [46]. M.Z. Ansari, N. Khare, *Effect of intrinsic strain on the optical band gap of single phase nanostructured $\text{Cu}_2\text{ZnSnS}_4$* . Mater. Sci.Semicond. Process. **63**(June), 220–226 (2017).
- [47]. Q. Guo, H.W. Hillhouse, R. Agrawal, *Synthesis of $\text{Cu}_2\text{ZnSnS}_4$ nanocrystals ink and its use for solar cells*. J. Am. chem. Soc. **131**, s1–s2 (2009)
- [48]. M.P. Suryawanshi et al., *CZTS based thin film solar cells: a status review*. Mater. Technol. **28**(1–2), 98–109 (2013).
- [49]. S. X. W. Y. L. Zhou, W. H. Zhou, Y. F. Du, M. Li, “*Sphere-like kesterite $\text{Cu}_2\text{ZnSnS}_4$ nanoparticles synthesized by a facile solvothermal method,*” Mater. Lett., vol. 65, pp. 1535–1537, 2011
- [50]. A.V. Moholkar et al., *Development of CZTS thin films solar cells by pulsed laser deposition: influence of pulse repetition rate*. Sol. Energy **85**(7), 1354–1363 (2011).
- [51]. S. Dongaonkar, M.A. Alam, *Geometrical design of thin film PV modules for improved shade tolerance and performance*. Dis. Model. Mech. **5**(2), 259–269 (2013).
- [52]. H.U.K. Sekiguchi, K. Tanaka, K. Moriya, *Epitaxial growth of $\text{Cu}_2\text{ZnSnS}_4$ thin films by pulsed laser deposition*. Phys. Status Solidi C **3**(8), 2618–2621 (2006).
- [53]. R. Adhi Wibowo, E. Soo Lee, B. Munir, K. Ho Kim, *Pulsed laser deposition of quaternary $\text{Cu}_2\text{ZnSnSe}_4$ thin films*. Phys. Status Solidi Appl. Mater. Sci. **204**(10), 3373–3379 (2007).
- [54] Nakazawa, Kentaro Ito. ‘Electrical and Optical Properties of Stannite-Type Quaternary Semiconductor Thin Films’. Japanese Journal of Applied Physics 27, no. 11R (November 1988): 2094.
- [55] H. Katagiri, K. Jimbo, S. Yamada, T. Kamimura, W. S. Maw, T. Fukano, T. Ito, and T. Motohiro, *Enhanced Conversion Efficiencies of $\text{Cu}_2\text{ZnSnS}_4$ -Based Thin Film Solar Cells by Using Preferential Etching Technique*, Applied Physics Express, 1, 041201 (2008).
- [56] Yu-Pin Lin, Yi-Fang Chi, Tsung-Eong Hsieh, Yen-Chih Chen, Kun-Ping Huang, *Preparation of $\text{Cu}_2\text{ZnSnS}_4$ (CZTS) sputtering target and its application to the fabrication of CZTS thin-film solar cells*, Journal of Alloys and Compounds, Volume 654, 2016, Pages 498-508, ISSN 0925-8388.
- [57] Sun, Kaiwen, et al. *Over 9% efficient kesterite $\text{Cu}_2\text{ZnSnS}_4$ solar cell fabricated by using $\text{Zn}_{1-x}\text{Cd}_x\text{S}$ buffer layer*. Advanced Energy Materials 6.12 (2016): 1600046.

- [58]. D. Lincot et al., *Chalcopyrite thin film solar cells by electrodeposition*. Sol. Energy **77**(6), 725–737 (2004).
- [59]. D. Cunningham, M. Rubcich, D. Skinner, *Cadmium telluride PV module manufacturing at BP solar*. Prog. Photovoltaics Res.Appl. **10**(2), 159–168 (2002).
- [60]. D. Lincot, *Electrodeposition of semiconductors*. Thin Solid Films **487**(1–2), 40–48 (2005).
- [61]. T. Washio et al., *6% Efficiency Cu₂ZnSnS₄- based thin film solar cells using oxide precursors by open atmosphere type CVD*. J. Mater. Chem. **22**(9), 4021 (2012).
- [62]. J.J. Scragg, P.J. Dale, L.M. Peter, *Towards sustainable materials for solar energy conversion: preparation and photoelectrochemical characterization of Cu₂ZnSnS₄*. Electrochem. commun. **10**(4), 639–642 (2008).
- [63]. J.J. Scragg, P.J. Dale, L.M. Peter, *Synthesis and characterization of Cu₂ZnSnS₄ absorber layers by an electrodeposition annealing route*. Thin Solid Films **517**(7), 2481–2484 (2009).
- [64]. J.J. Scragg, D.M. Berg, P.J. Dale, *A 3.2% efficient Kesterite device from electrodeposited stacked elemental layers*. J. Electroanal. Chem. **646**(1–2), 52–59 (2010).
- [65]. R. Schurr et al., *The crystallisation of Cu₂ZnSnS₄ thin film solar cell absorbers from co-electroplated Cu–Zn–Sn precursors*. Thin Solid Films **517**(7), 2465–2468 (2009).
- [66] Jacques Livage, *Les procédés sol-gel*, revue du verre, Vol 6, N° 5, Octobre (2000).
- [67] M. Farida, *Préparation et caractérisation de couches minces d'oxyde de titane(TiO₂) et du couple d'oxydes (TiO₂/SnO₂)*, thèse de magister, Université Mentouri Constantine, (2012).
- [68] Agawane, G.L., Shin, S.W., Vanalakar, S.A. et al. *Synthesis of simple, low cost and benign sol-gel Cu₂ZnSnS₄ thin films: influence of different annealing atmospheres*. J Mater Sci: Mater Electron **26**, 1900–1907 (2015).
- [69] J.M. Y. Yeh, C. C. Lee, and D. S. Wu, *Influences of synthesizing temperatures on the properties of Cu₂ZnSnS₄ prepared by sol-gel spin-coated deposition*, Journal of Sol-Gel Science and Technology, vol. 52, no. 1, pp. 65–68, 2009.
- [70]. S. Engberg, Z. Li, J.Y. Lek, Y.M. Lam, J. Schou, *Synthesis of large CZTSe nanoparticles through a two-step hot-injection method*. RSC Adv. **5**(117), 96593–96600 (2015).
- [71]. A.S. Najm et al., *Towards a promising systematic approach to the synthesis of CZTS solar cells*. Sci. Rep. **13**(1), 1–16 (2023).
- [72]. E.M. Mkawi, Y. Al-Hadeethi, E. Shalaan, E. Bekyarova, *Substrate temperature effect during the deposition of (Cu/Sn/Cu/Zn)stacked precursor CZTS thin film deposited by electron-beam evaporation*. J. Mater. Sci. Mater. Electron. **29**(23), 20476–20484 (2018).
- [73]. S.A. Vanalakar et al., *A review on pulsed laser deposited CZTS thin films for solar cell applications*. J. Alloys Compd. **619**(2020), 109–121 (2015). <https://doi.org/10.1016/j.jallcom.2014.09.018>.
- [74]. S.M. Bhosale, M.P. Suryawanshi, M.A. Gaikwad, P.N. Bhosale, J.H. Kim, A.V. Moholkar, *Influence of growth temperatures on the properties of photoactive CZTS thin films using a spray pyrolysis technique*. Mater. Lett. **129**, 153–155 (2014).
- [75]. X. Zhang, E. Fu, Y. Wang, C. Zhang, *Fabrication of Cu₂ZnSnS₄ (CZTS) nanoparticle inks for growth of CZTS films for solar cells*. Nanomaterials **9**(3), 1–10 (2019).
- [76]. M. Mokhtarimehr, I. Forbes, N. Pearsall, *Environmental assessment of vacuum and non-vacuum techniques for the fabrication of Cu₂ZnSnS₄ thin film photovoltaic cells*. Jpn. J. Appl. Phys. (2018).
- [77]. M.A. Olgar, J. Klaer, R. Mainz, L. Ozyuzer, T. Unold, *Cu₂ZnSnS₄-based thin films and solar cells by rapid thermal annealing processing*. Thin Solid Films **628**, 1–6 (2017).

- [78]. M.F. Islam, N. Mdyatim, M.A. HashimIsmail, *A review of CZTS thin film solar cell technology*. J. Adv. Res. Fluid Mech. Therm. Sci. **81**(1), 73–87 (2021).
- [79]. S. Das, P. Chandra Mahakul, P. Mahanandia, *High efficient hybrid bulk hetero junction thin-film solar cell embedded with kesterite $\text{Cu}_2\text{ZnSnS}_4$ quantum dots*. Superlattices Microstruct. **148**, 106719 (2020).
- [80]. P.K. Singh, S. Rai, D.K. Dwivedi, *WITHDRAWN: numerical analysis on the improvement of open circuit voltage of kesterite based $\text{Cu}_2\text{ZnSnS}_4$ thin films solar cell*. Mater. Today Proc. (2020).
- [81]. R. K. Vataketath, *Investigation on the Transparent Conducting Oxide (TCO) material used in CIGS thin film solar cell in Midsummer AB*, no. October, 2020.
- [82]. Z. Yu et al., *Indium tin oxide as a semiconductor material in efficient p-type dye-sensitized solar cells*. NPG Asia Mater. **8**(9), e305–e305 (2016).
- [83]. A. Sharmin, S. Tabassum, M.S. Bashar, Z.H. Mahmood, *Depositions and characterization of sol-gel processed Al-doped ZnO (AZO) as transparent conducting oxide (TCO) for solar cell application*. J. Theor. Appl. Phys. **13**(2), 123–132 (2019).
- [84]. H.M. Mirletz, K.A. Peterson, I.T. Martin, R.H. French, *Degradation of transparent conductive oxides: Interfacial engineering and mechanistic insights*. Sol. Energy Mater. Sol. Cells **143**, 529–538 (2015).
- [85]104. R. Paul, T. R. Lenka, and F. A. Talukdar, *Performance Improvement of CZTSSe Solar Cell by using Mg-doped ZnO as Window Layer*, in *2021 IEEE 18th India Council International Conference (INDICON)*, Dec. 2021, pp. 1–5.
- [86]. R. Paul, S. Vallisree, T.R. Lenka, F.A. Talukdar, *Modeling and simulation of CZTS thin-film solar cell for efficiency enhancement*. J. Electron. Mater. **51**(5), 2228–2235 (2022).
- [87] A. Crovetto, *$\text{Cu}_2\text{ZnSnS}_4$ Solar Cells: Physics and Technology by Alternative Tracks*, PhD thesis, Technical University of Denmark, Department of Micro and Nanotechnology, (2016).
- [88] J. Yu, Z. Zheng, L. Dong, S. Cheng, Y. Lai, Q. Zheng, and al., *Effect of deposited temperatures of the buffer layer on the band offset of CZTS/In₂S₃ heterostructure and its solar cell performance*, *Chinese Physics B*, vol. 26, no. 4, 046802, pp. 1-6, 2017.
- [89] N.E. Gorji, *Quantitative analysis of the optical losses in CZTS thin film semiconductors*, *IEEE Transactions on Nanotechnology*, vol. 13, no. 4, pp. 743-748, 2014.
- [90] F. Jiang, H. Shen, W. Wang, and L. Zhang, *Preparation and properties of $\text{Cu}_2\text{ZnSnS}_4$ absorber and $\text{Cu}_2\text{ZnSnS}_4$ /amorphous silicon thin film solar cell*, *Applied Physics Express*, vol. 4, no. 7, 074101, pp. 1-3, 2011.
- [91] G. Yang, Y-F. Li, B. Yao, Z-H. Ding, R. Deng, J-M. Qin, and al., *Band alignments at interface of $\text{Cu}_2\text{ZnSnS}_4$ /ZnO heterojunction: An X-ray photoelectron spectroscopy and first-principles study*, *Journal of Alloys and Compounds*, vol. 628, pp. 293-297, 2015.
- [92] A. Nagoya, R. Asahi, and G. Kresse, *First-principles study of $\text{Cu}_2\text{ZnSnS}_4$ and the related band offsets for photovoltaic applications*, *Journal of Physics: Condensed Matter*, vol. 23, no. 40, 404203, pp. 1-6, 2011.
- [93]. Paul, R., Shukla, S., Lenka, T.R. et al. *Recent progress in CZTS (CuZnSn sulfide) thin-film solar cells: a review*. J Mater Sci: Mater Electron **35**, 226 (2024).
- [94]. C. Platzer-Björkman et al., *Back and front contacts in kesterite solar cells: State-of-the-art and open questions*. JPhys Energy (2019).
- [95]. S. Zhang et al., *Band alignment tuning at Mo/CZTS back contact interface through surface oxidation states control of Mo substrate*. Sol. Energy Mater. Sol. Cells **229**, 111141 (2021).
- [96]. S. Mahjoubi, N. Bitri, E. Aubry, F. Chaabouni, P. Briois, *Back contact nature effect on the CZTS/ZnS based heterojunction*. Appl. Phys. A **128**(5), 380 (2022).

- [97]. H. Toura, Y.H. Khattak, F. Baig, B.M. Soucase, M.E. Touhami, *Back contact effect on electrodeposited CZTS kesterite thin films experimental and numerical investigation*. Sol. Energy **194**(July), 932–938 (2019).
- [98]. S. Enayati Maklavani, S. Mohammad nejad, *Reduction of interface recombination current for higher performance of p^+ CZTS_xSe_(1-x)/p-CZTS/n-CdS thin-film solar cells using Kesterite intermediate layers*. Sol. Energy **204**, 489–500 (2020).
- [99]. X. Lu et al., *Modification of back contact in Cu₂ZnSnS₄Solar cell by inserting Al-Doped ZnO intermediate layer*. ACS Appl. Mater. Interfaces **12**(52), 58060–58071 (2020).
- [100]. S. Enayati Maklavani, S. Mohammad nejad, *Enhancing the open circuit voltage and efficiency of CZTS thin-film solar cells via band-offset engineering*. Opt. Quantum Electron. **52**(2), 1–22(2020).
- [101]. M. Kauk-Kuusik et al., *Detailed insight into the CZTS/CdS interface modification by air annealing in monograin layer solar cells*. ACS Appl. Energy Mater. **4**(11), 12374–12382 [(2021).
- [102]. H. Ferhati, F. Djefal, *Graded band-gap engineering for increased efficiency in CZTS solar cells*. Opt. Mater. (Amst) **76**, 393–399 (2018).

Chapter 3: Numerical Modeling by SCAPS 1-D

3.1. Introduction

By merging numerical analysis techniques with a computer or other virtual machine environment, one can utilize them to solve real-life issues. This has enabled the discipline of numerical problem solving with computers to come up with an effective approach towards tackling tough problems. The introduction of time-saving computing made it feasible to optimize any real-time design problem without having to physically implement anything in real test conditions. Global colleges prioritize computer-based learning because these systems have benefited semiconductor device developers. Semiconductor-based products like solar panels, laptops, computers, and cell phones now make up most of the global market. The most well-known area of semiconductor devices is the solar cell. It is possible to transform sunlight into electrical energy using a semiconductor device, and since customers are consuming too much electricity, solar cells are a good substitute to meet demand [1–4]. However, nuclear power plants, coal-fired thermal power plants, natural gas-fired thermal power plants, and hydel power plants today provide the majority of the world's energy needs [5]. Solar photovoltaic, or solar cells, are the subject of intense research due to the significant impact that fossil fuel combustion has on climate change [6–8]. The development of new and improved solar cell designs is happening very quickly, with efficiency rising to a maximum of 22%. However, there are still issues with these devices' price, accessibility, and stability for future commercial growth [9–11]. Therefore, numerical analysis of solar cells using a computer can be very important in solving these problems. The computer makes it possible to create realistic problems with flexibility, which makes it simple to experiment with various theories. Furthermore, it is frequently possible to obtain a full set of device characteristics with less time and effort required than a limited collection of manually calculated single point values. From the foregoing discussion, it is clear that numerical analysis of photovoltaic solar cells is a necessary way to evaluate the viability of the proposed physical structure and its performance, hence enabling rapid design and efficiency improvements. This chapter will discuss the impact of physical parameters on solar cell performance, including temperature, doping concentration in the layers, and layer thickness, using the key input parameters as a guide. When performing a numerical study of a solar cell, it is highly beneficial to start from a shared baseline [12]. This numerical study will produce consequences for verifying the viability of the suggested physical explanation and forecasting the effect of modifications in material attributes.

3.2. Basic Equations

The functioning of the majority of semiconductor devices, such as solar cells, may be explained using the mathematical equations referred to as semiconductor device equations. The fundamental equations governing the functioning of a semiconductor device elucidate the static and dynamic properties of charge carriers in semiconductors when subjected to external factors, such as applied electric fields or optical excitation, that disrupt the thermal equilibrium state. SCAPS-1D solves the one dimensional semiconductor equations. The equations are as follows:

A. Current –density equations:

Derivations of Boltzmann transport theory have demonstrated that the current densities in the continuity equations can be estimated using a conduction-diffusion model [13]. The current densities in this scenario are represented by the quasi-Fermi levels E_{Fn} and E_{Fp} .

$$\vec{J}_n = \mu_n n \nabla E_{Fn} \quad (3.1)$$

$$\vec{J}_p = \mu_p p \nabla E_{Fp} \quad (3.2)$$

μ_n and μ_p represent the mobilities of electrons and holes, respectively. The quasi-Fermi levels are determined by the carrier concentrations and the potential by the application of Boltzmann approximations [13].

$$n = n_i \exp\left(\frac{q\psi - E_{Fn}}{k_B T}\right) \quad (3.3)$$

$$p = n_i \exp\left(\frac{-q\psi + E_{Fp}}{k_B T}\right) \quad (3.4)$$

These two equations can then be rewritten to define the quasi-Fermi levels [3]:

$$E_{Fn} = q\psi - k_B T \ln\left(\frac{n}{n_i}\right) \quad (3.5)$$

$$E_{Fp} = q\psi + k_B T \ln\left(\frac{p}{n_i}\right) \quad (3.6)$$

By replacing these equations in the current density formulas, the resulting current relationships are derived as follows:

$$\vec{J}_n = qD_n \nabla n - qn\mu_n \nabla \psi - n\mu_n (k_B T \Delta(\ln n_i)) \quad (3.7)$$

$$\vec{J}_p = -qD_p\nabla p - qp\mu_p\nabla\psi - p\mu_p(k_B T\Delta(\ln n_i)) \quad (3.8)$$

Where D_n and D_p represent the diffusion constants for electrons and holes, respectively.

$$D_n = \frac{k_B T}{q} \mu_n \quad (3.9)$$

$$D_p = \frac{k_B T}{q} \mu_p \quad (3.10)$$

The last term in equations (3.7) and (3.8) takes into consideration the gradient of the effective intrinsic carrier concentration, which incorporates the impact of bandgap narrowing. The effective electric fields are determined by:

$$\vec{E}_n = -\nabla\left(\psi + \frac{k_B T}{q} \ln n_i\right) \quad (3.11)$$

$$\vec{E}_p = -\nabla\left(\psi - \frac{k_B T}{q} \ln n_i\right) \quad (3.12)$$

This enables us to express the conduction-diffusion equations in their most standard form:

$$\vec{J}_n = q\mu_n n \vec{E}_n + qD_n \nabla n \quad (3.13)$$

$$\vec{J}_p = q\mu_p p \vec{E}_p - qD_p \nabla p \quad (3.14)$$

B. Continuity equations:

The continuity equation elucidates the dynamics of surplus carriers over time and space when subjected to electric fields and density gradients.

$$\frac{\partial n}{\partial t} = \frac{1}{q} \text{div} \vec{J}_n + G_n - R_n \quad (3.15)$$

$$\frac{\partial p}{\partial t} = -\frac{1}{q} \text{div} \vec{J}_p + G_p - R_p \quad (3.16)$$

Where n and p are the concentrations of electrons and holes, J_n and J_p are the current densities of electrons and holes, G_n and G_p are the rates of electron and hole generation, and R_n and R_p are the rates of electron and hole recombination.

At steady state: $\frac{dn}{dx} = 0$ and $\frac{dp}{dx} = 0$.

C. Poisson equation:

The Poisson equation establishes a relationship between the electric potential and the space charge density.

$$\text{div} (\epsilon \nabla \Psi) = -\rho \quad (3.17)$$

The variables in the equation are as follows: ψ represents the electrostatic potential, ϵ represents the permittivity of the medium, and ρ represents the space charge density of the medium. The space charge density of the medium is the cumulative effect of all mobile and fixed charges, encompassing electrons, holes, and ionized impurities.

$$\rho = q(N_D + N_A + n + p) \quad (3.18)$$

The variables in the equation are as follows: q represents the elementary charge, n represents the electron concentration, p represents the hole concentration, N_A represents the concentration of ionized acceptor atoms, and N_D represents the concentration of ionized donor atoms. The electric field is derived from the gradient of the potential:

$$\vec{E} = -\nabla \psi \quad (3.19)$$

Various commercially available software and educational software exist for the numerical analysis of solar cells, which effectively solve the fundamental semiconductor equations. Below is a compilation of software that is available free of charge for educational purposes.

- SCAPS-1D (Solar cell capacitance simulator)
- FORS-HET (Automat FOR Simulation of Heterostructures)
- AMPS-1D (Analysis of Microelectronics and Photonics Structures)
- PC1D
- ASA (Amorphous Semiconductor Analysis)

Our work is carried out with SCAPS-1D, which is one of the various software programs that have been mentioned above. The reason that we have chosen SCAPS is due to the fact that there is a

substantial body of literature available for SCAPS and its potential applications for the analysis of a solar cell.

3.3. SCAPS-1D

Developed at the Department of Electronics and Information Systems (ELIS) of the University of Gent in Belgium, SCAPS-1D, also known as the Solar Cell Capacitance Simulator, is a program that simulates solar cells in a single dimension. Alex Niemegeers, Marc Burgelman, Koen Decock, Stefaan Degraeve, and Johan Verschraegen are just some of the researchers who have made contributions to its development.

SCAPS – 1D is a simulation program that is capable of modeling photovoltaic (PV) devices in a one-dimensional space. There are seven distinct semiconductor layers that can be taken as input in the SCAPS–1D software. These layers are distinct from the back and front contacts. The tool known as SCAPS–1D is freely accessible to the community of photovoltaic researchers and available for free download from its web link. It is a window-based operating system environment that it operates in. With the help of this software, we are able to simulate and analyze the characteristics curve $J-V$, as well as the ac characteristics ($C-V$ and $V-f$), the spectral response (QE) of a device, the power conversion efficiency (PCE), the fill factor (FF), the short-circuit current (J_{sc}), the open circuit voltage (V_{oc}), the energy bands of the materials used in solar cells, and the concentration of various materials used by solving the semiconductor basic equations.

In our work, we have relied on the simulation package known as SCAPS 1D. The majority of the information that we have used comes from the SCAPS manual [14]. Figure 3.1 offers a visual representation of the simulation stages known as SCAPS.

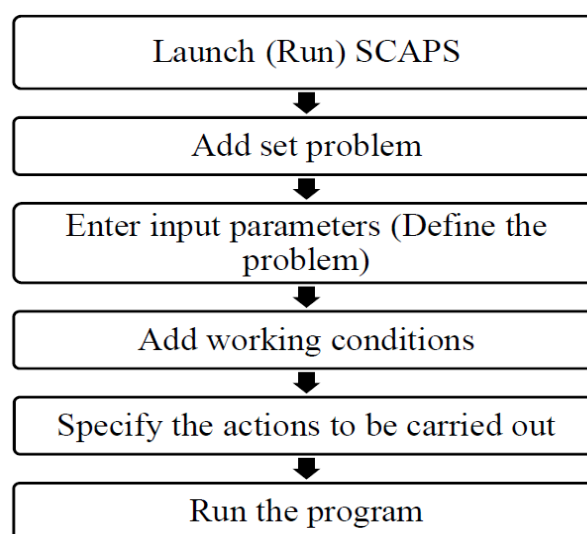


Figure 3.1: SCAPS working procedure.

3.3.1. Parameters

In device modeling, input or physical parameters are crucial for solving the fundamental equations of semiconductors. SCAPS-1D software utilizes various physical parameters like layer thickness, electron-hole mobility, intrinsic carrier concentration, electron affinity, band gap, and doping density of absorber, buffer, and window layers, as listed in Table 4.1. Symbols such as N_v represent the effective density of states in the valence band, N_c represent the effective density of states in the conduction band, both measured in cm^{-3} . p represents the concentration of holes in cubic centimeters (cm^{-3}), while n represents the concentration of electrons. W denotes the thickness of the material in micrometers (μm). χ represents the electron affinity measured in eV, E_g represents the bandgap measured in eV, μ_e represents the electron mobility measured in cm^2/Vs , and μ_h represents the hole mobility measured in cm^2/Vs .

All simulations are conducted under 1.5 AM solar radiation with an illuminating source of $100 \text{ mW}/\text{cm}^2$. Functional parameters of solar cells are provided in Table 3.1. The creation of the device serves two primary purposes: understanding and confirming the actual behavior of the device, and simulating the device using specific physical parameters to forecast corresponding results. The quality of device modeling is determined by how accurately the behavior of the reference device(s) is simulated.

SCAPS provides comprehensive simulations including J–V characteristics curve, AC characteristics (C–V and C–f), spectral response (QE), and advanced batch simulations with variable input parameters. Batch simulations monitor and analyze predefined physical parameters like carrier concentration densities and layer thickness. Outputs from SCAPS-1D software include J–V characteristics curve, band alignment diagram, spectral response, and functional parameters such as PCE, FF, J_{sc} , and V_{oc} . These outputs are crucial for producing high-performance photovoltaic devices. Measurements are computed for both illuminated and dark conditions, varying with temperature. Thermal velocity and effective density of states vary with temperature, while bandgap and mobility remain constant.

The Shockley-Read-Hall (SRH) formalism is employed to describe recombination processes occurring at interface states and within deep bulk levels, and to determine their occupation.

3.3.2. Interface for the front end of SCAPS-1D

Figure 3.2 displays the user interface of the SCAPS-1D software. The composition primarily comprises four panels, and the following is a summary of these panels.

1. *The problem definition panel* is utilized to specify the structure of a solar cell in SCAPS software. It allows for the analysis of simulated output, the saving of simulated output data, and the clearing of simulated history in SCAPS. In order to specify the structure of a solar cell, it is necessary to select a designated button for setting the problem.
2. *The action panel* is used to read and adjust the scale settings. It includes the calibration and setting of I-V characteristics scale, the capacitance voltage setting of C-V, the capacitance frequency setting of C-F, and the quantum efficiency setting of QE.
3. *The illumination panel* is used to adjust the spectrum and direction of the light that will illuminate the solar cell structure.
4. *The working point* refers to the specific temperature at which a system is set to operate.

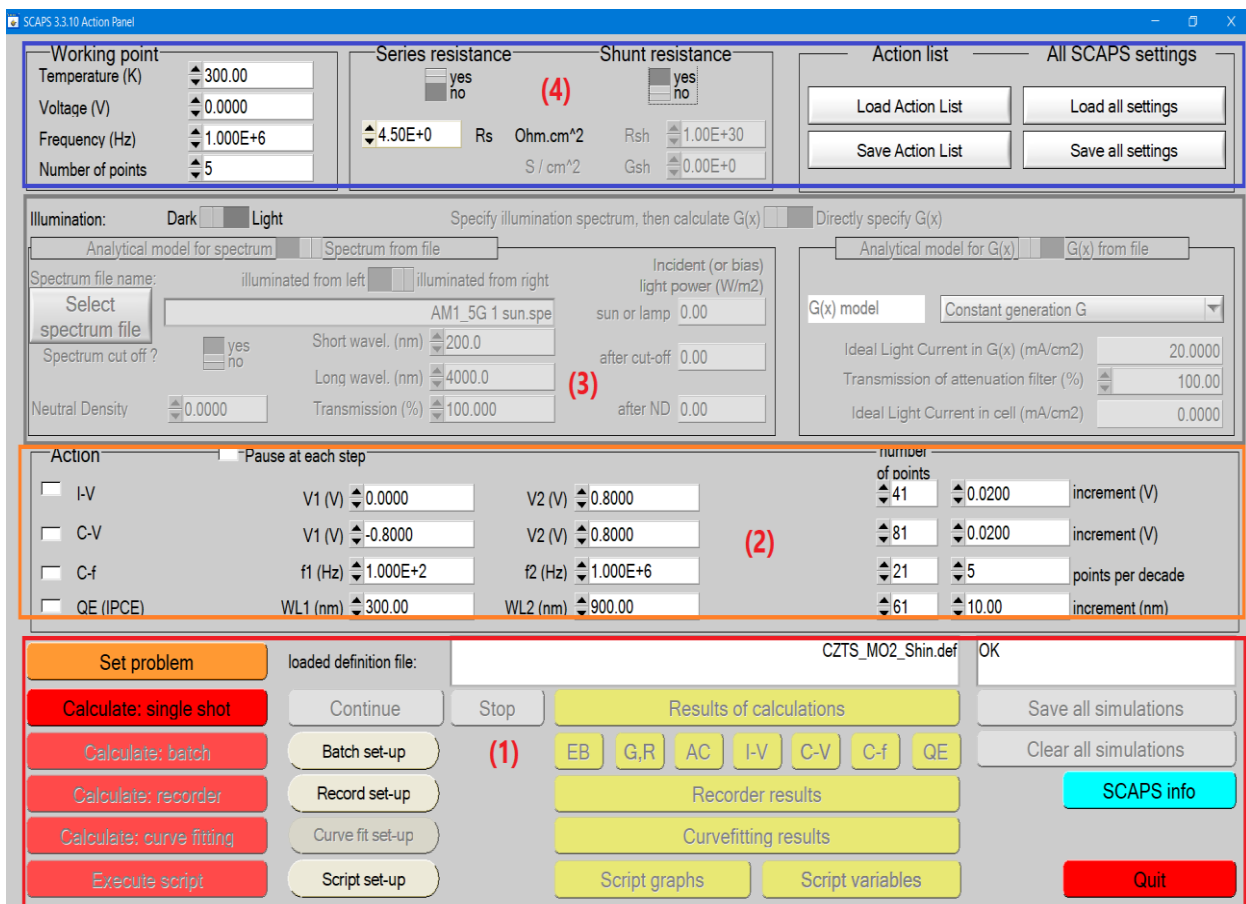


Figure 3.2: SCAPS startup panel: Action panel or main panel.

3.4. Solar Cell Definition

3.4.1. Editing a Solar Cell Structure

When you click the 'Set Problem' button on the action panel, it brings up the 'Solar cell definition' panel. This panel is where you can create and modify solar cell structures, and you can also save and load these structures using definition files. These files have the extension '*.def' and are standard ASCII files that can be opened using Notepad. Here, you can include various properties of your cell such as band gap, electron affinity, thickness, defects, and others.

You can add layers, contacts, and interface properties by selecting the corresponding boxes shown in Figure II.4. Additionally, users can add extra layers by selecting the 'add layer' option. You have the flexibility to specify your own reference conventions for the applied voltage V and the current density J in the external contacts.

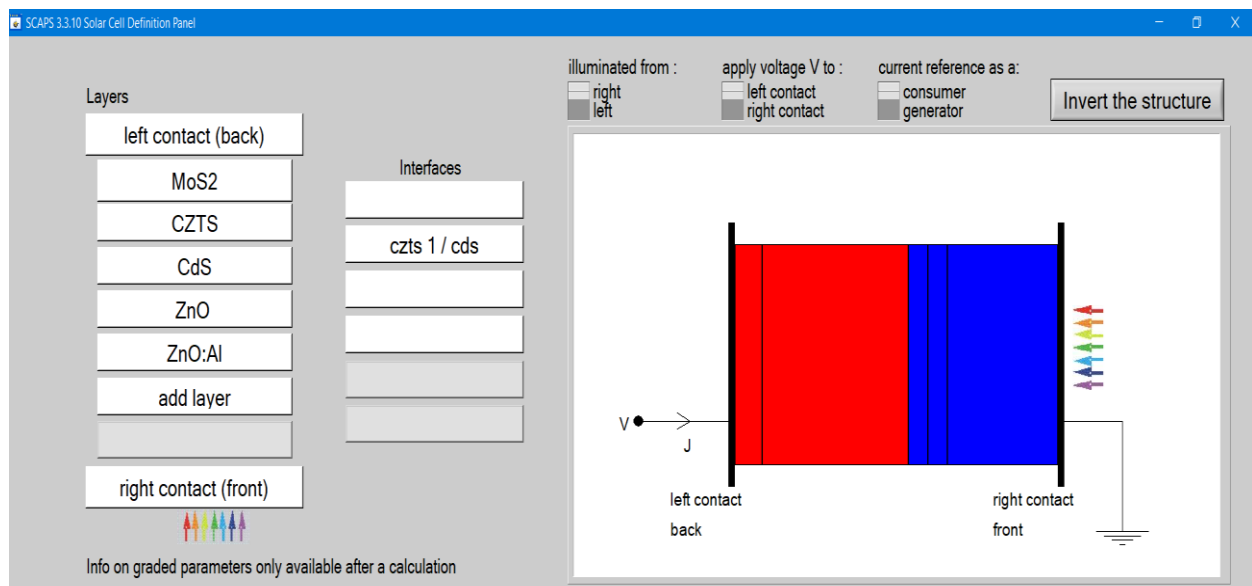


Figure 3.3: Defining a solar cell structure.

SCAPS 1D offers several features, including:

1. **Voltage Reference Settings:** In SCAPS < 4.0, the 'left' setting applies voltage V to the left contact, with the right contact serving as the reference. The 'right' setting reverses this, with the left contact becoming the reference. This affects the orientation of JV curves.
2. **Current Reference Arrow:** When specifying 'consumer', the current reference arrow represents power consumed ($P = J.V$), while 'generator' mode adjusts it to represent power generated. The arrow's position depends on voltage reference and consumer/generator selection.

3. **Solar Cell Structure Inversion:** Mirroring the structure along the x-axis swaps layers, interfaces, and grading information. Double-clicking the inversion icon restores the original layout, preserving illumination side, voltage, and current reference settings.
4. **Default Reference Configuration:** Internally, SCAPS applies voltage at the left contact and represents current from left to right, interpreting it as a consumer.
5. **Consistent Output Representation:** Output, including graphs and tables, aligns with the user's selected reference. Note: Electric field in SCAPS output is independent of user-defined V and J references, consistently referenced to the positive x-axis (from left to right).

3.4.2. Adding device structure layers

To add or define layers in SCAPS 1D software for modeling PV devices, simply click on the "add layer" button located in section 1 of Fig 3.3. The layer properties interface will appear as a pop-up when you click the button. The layer's physical parameter values are established or inserted through the layer properties interface. Figure 3.4 illustrates the user interface.

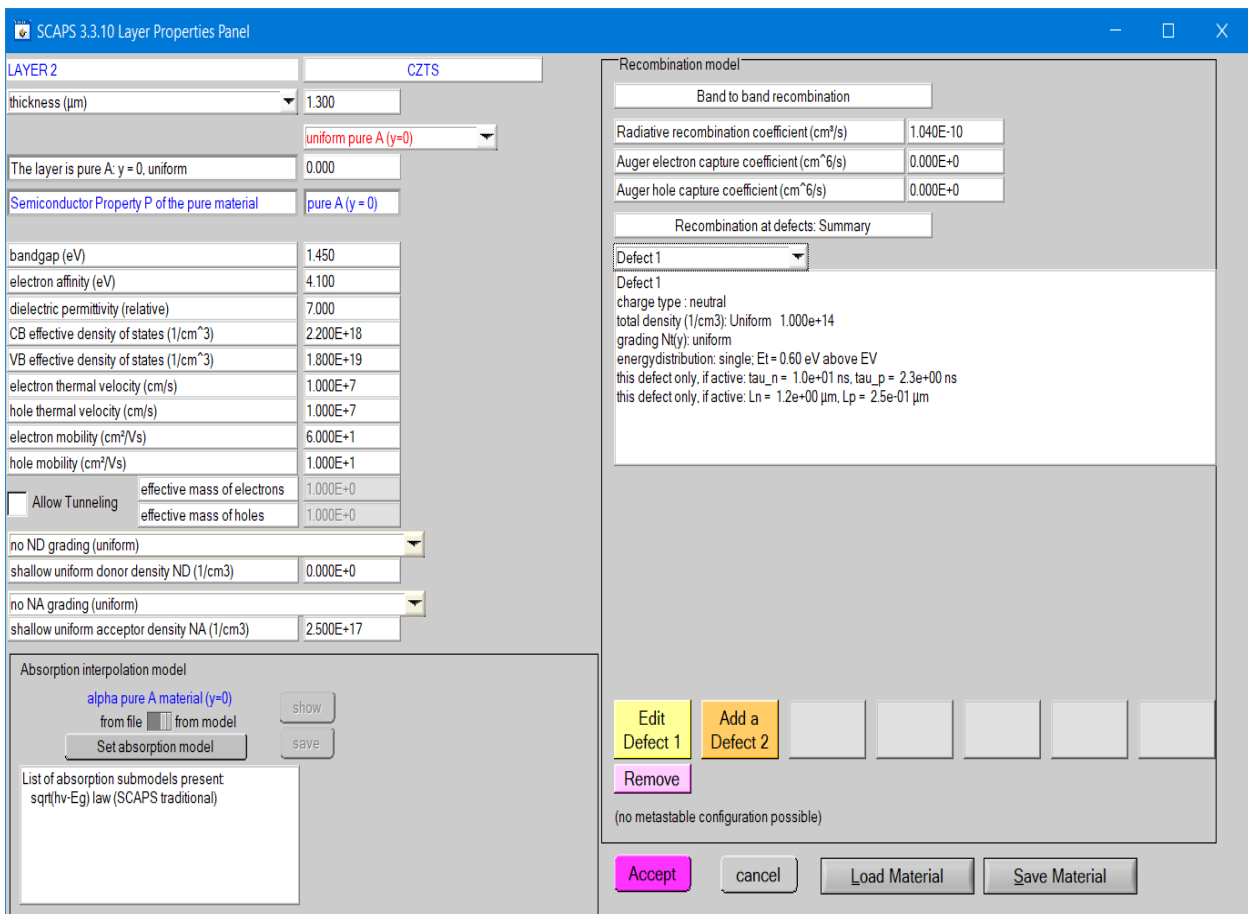


Figure 3.4: Layer properties panel.

Once the physical characteristics of each layer, including the absorber layer, buffer layer, and window layer, have been determined, the device structure is analyzed using numerical modeling in SCAPS 1D software. An investigation is conducted to examine the influence of different physical characteristics on the performance of photovoltaic devices. The physical parameters of the absorber and buffer layers include their thicknesses, doping concentrations, and operating temperature.

3.4.3. Contact

The contact properties can be configured by selecting either the front or back contact button on the cell definition panel, which will open the 'contact properties panel', as shown in Figure 3.5.

The user can input the metal work function Φ_m for majority carriers. Alternatively, the user has the option to select "flat bands". SCAPS calculates the metal work function Φ_m for each temperature, ensuring that flat band conditions are maintained. The panel allows for the modification of the 'thermionic emission/surface recombination velocity (cm/s)' values for both electrons and holes. Additionally, various electrical and optical properties of the cell can be incorporated using this panel.

Equation (3.20) is employed when the layer next to the contact is of n-type. Equation (3.21) is employed when the material is in the p-type. Equation (3.22) is utilized when it is deemed to be inherent. It is evident that the calculation of the flat band metal work function only considers the shallow doping density.

$$\Phi_m = \chi + k_B T \ln \left(\frac{N_c}{N_D - N_A} \right) \quad (3.20)$$

$$\Phi_m = \chi + E_g - k_B T \ln \left(\frac{N_c}{N_A - N_D} \right) \quad (3.21)$$

$$\Phi_m = \chi + k_B T \ln \left(\frac{N_c}{n_i} \right) \quad (3.22)$$

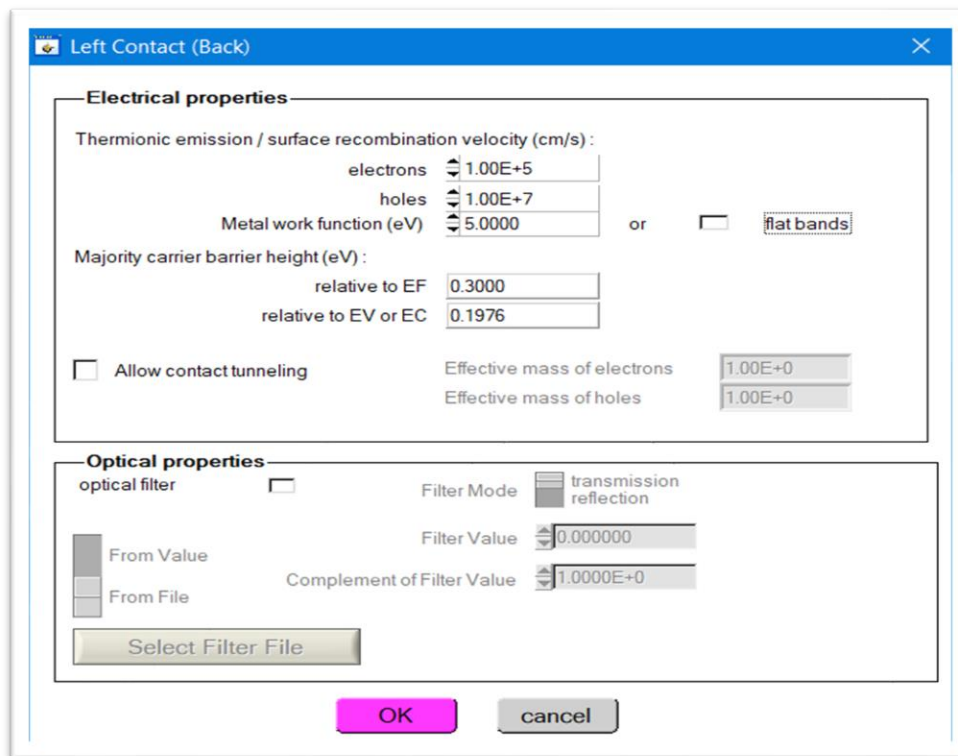


Figure 3.5: Contact properties panel.

3.4.4. Defects and Recombination

A diode is a device that converts current from hole current at the p-contact to electron current at the n-contact. Recombination must occur within the diode, even in an ideal device. Therefore, the user must specify recombination at least in one location (layer, contact, or interface). Failure to do so leads to convergence failure, resulting in non-equilibrium conditions (non-zero voltage and/or illumination). Recombination processes in semiconductor layers can be introduced as defects, radiative, and Auger.

Recombination model

Band to band recombination

Radiative recombination coefficient (cm ³ /s)	1.040E-10
Auger electron capture coefficient (cm ⁶ /s)	0.000E+0
Auger hole capture coefficient (cm ⁶ /s)	0.000E+0

Recombination at defects: Summary

Defect 1

Defect 1
charge type : neutral
total density (1/cm3): Uniform 1.000e+14
grading Nt(y): uniform
energydistribution: single; Et = 0.60 eV above EV
this defect only, if active: tau_n = 1.0e+01 ns, tau_p = 2.3e+00 ns
this defect only, if active: Ln = 1.2e+00 μm, Lp = 2.5e-01 μm

Edit Defect 1 Add a Defect 2

Remove

(no metastable configuration possible)

Figure 3.6: Recombination model and defects.

There is a possibility that a semiconductor layer could contain as many as seven defects. This depends on the type of cell, the type of semiconductor, and the defects that are related to each defect (Figure 3.7). The parameters that govern each defect can be edited by clicking the appropriate Add/Edit-button, which opens the 'defect properties panel' (Figure 3.6). In addition, everything that pertains to the defects that are present in a single layer, including the defect type, the electron thermal capture cross section, the hole thermal capture cross section, the energetic distribution, and other related factors.

It is also possible to right-click on one of the "defect summary text boxes," which will then open a panel that allows a defect to be removed, duplicated, or added. This process is very similar to the one that was used when removing, duplicating, and adding a layer.

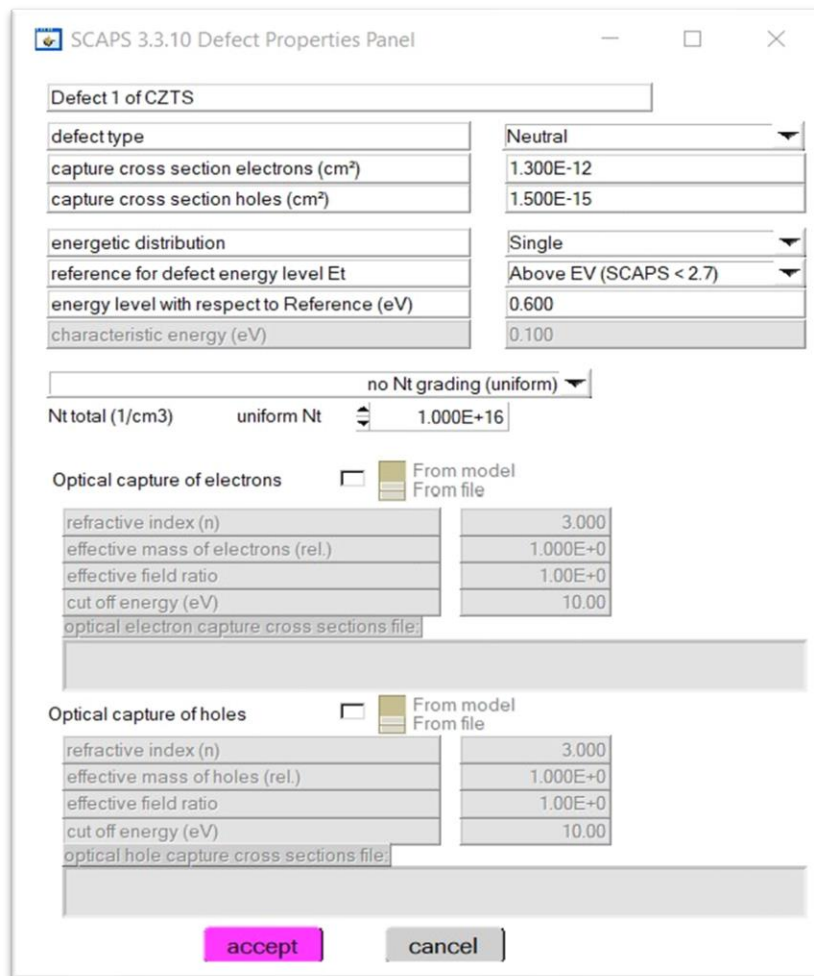


Figure 3.7: The defect properties panel.

3.4.5 Interfaces

In SCAPS, it's possible to define an interface between any two semiconductor layers. Interface transport is typically modeled using thermionic emission, which correlates the thermal velocity of interface transport with the smallest thermal velocity of the adjacent layers. Even in the absence of band offsets, this model implies a step in quasi-Fermi level energy values at the interface, albeit relatively small.

Recombination centers may also be present at interfaces, similar to bulk layers. Interface defects are defined similarly to bulk defects, with three potential defects and univalent charge types. Interface defect parameters can be modified by selecting the checkbox located on the interface, allowing for the addition of defect parameters.

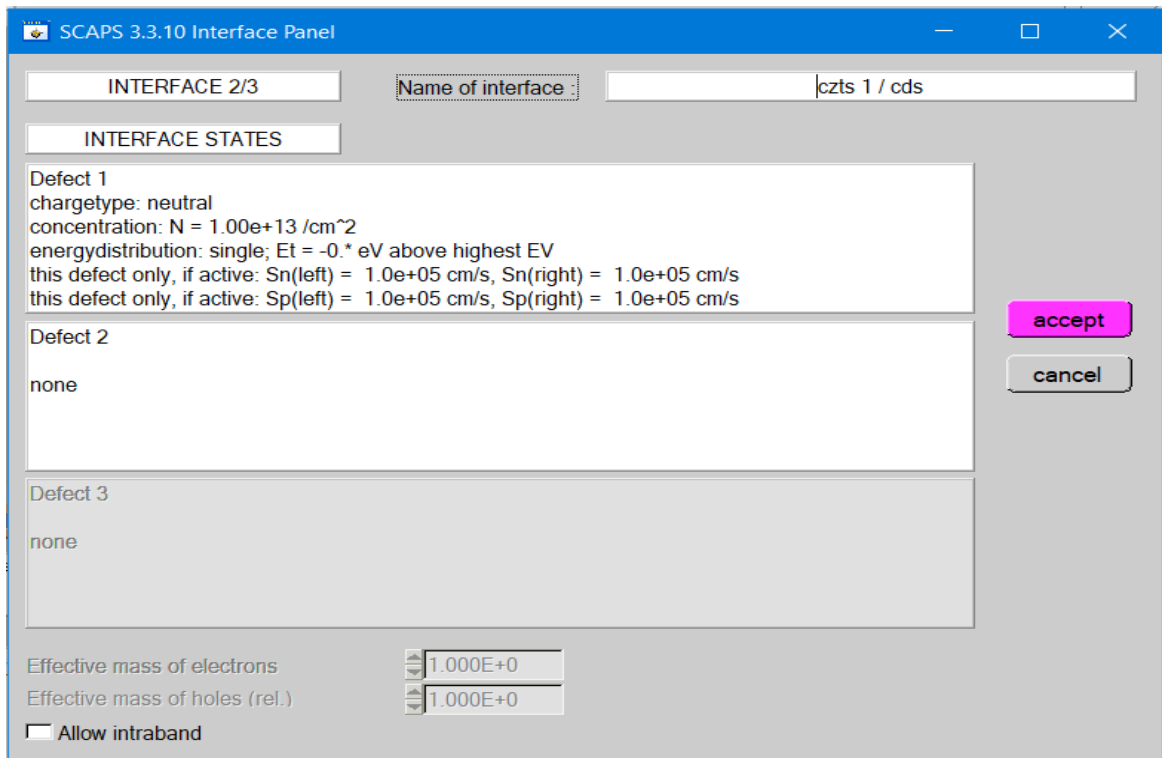


Figure 3.8: Interface defects panel.

3.5. Conclusion

This chapter provides an introduction to the SCAPS 1-D simulation program, including its operational methodology and the simulation units employed to replicate the technological processes and electrical characteristics of solar cell devices. In addition, we provided an overview of the different commands and physical principles governing the operation of the SCAPS simulation device.

References

- [1] C.A. Craig, S. Feng, *Exploring utility organization electricity generation, residential electricity consumption, and energy efficiency: A climatic approach*, Appl. Energy. 185 (2017) 779–790..
- [2] P. Mir-Artigues, E. Cerdá, P. del Río, *Analysing the economic impact of the new renewable electricity support scheme on solar PV plants in Spain*, Energy Policy. 114 (2018) 323–331.
- [3] E. Nuño, P. Maule, A. Hahmann, N. Cutululis, P. Sørensen, I. Karagali, *Simulation of transcontinental wind and solar PV generation time series*, Renew. Energy. 118 (2018) 425–436.
- [4] A. Honrubia-Escribano, F.J. Ramirez, E. Gómez-Lázaro, P.M. Garcia-Villaverde, M.J. Ruiz-Ortega, G. Parra-Requena, *Influence of solar technology in the economic performance of PV power plants in Europe. A comprehensive analysis*, Renew. Sustain. Energy Rev. 82 (2018) 488–501.
- [5] oecd-factbook-2015-2016, (n.d.). https://read.oecd-ilibrary.org/economics/oecd-factbook-2015-2016/world-electricity-generation-by-source-of-energy_factbook-2015-graph86-en#page1.
- [6] T. Novakov, M.O. Andreae, R. Gabriel, T.W. Kirchstetter, O.L. Mayol-Bracero, V. Ramanathan, *Origin of carbonaceous aerosols over the tropical Indian Ocean: Biomass burning or fossil fuels?*, Geophys. Res. Lett. 27 (2000) 4061–4064.
- [7] K. Caldeira, M.E. Wickett, *Anthropogenic carbon and ocean pH*, Nature. 425 (2003) 365–365.
- [8] W.B. Lyons, E. Saelens, K.A. Welch, *The impact of fossil fuel burning related to scientific activities in the McMurdo Dry Valleys, Antarctica: Revisited*, Elem Sci Anth. 6 (2018) 33.
- [9] L. Järup, A. Åkesson, *Current status of cadmium as an environmental health problem*, Toxicol. Appl. Pharmacol. 238 (2009) 201–208. doi:10.1016/j.taap.2009.04.020.
- [10] N. Espinosa, M. Hösel, D. Angmo, F.C. Krebs, *Solar cells with one-day energy payback for the factories of the future*, Energy Environ. Sci. 5 (2012) 5117–5132. doi:10.1039/C1EE02728J.
- [11] D. Wang, M. Wright, N.K. Elumalai, A. Uddin, *Stability of perovskite solar cells*, Sol. Energy Mater. Sol. Cells. 147 (2016) 255–275.
- [12] Y.H. Khattak, F. Baig, S. Ullah, B. Marí, S. Beg, H. Ullah, *Numerical modeling baseline for high efficiency (Cu_2FeSnS_4) CFTS based thin film kesterite solar cell*, Optik (Stuttg). 164 (2018) 547–555.
- [13] S.M. Sze, K. K. N., “Physics of semiconductor devices” (2007)
- [14] M. Burgelman, K. Decock, A. Niemegeers, J. Verschraegen, and S. Degraeve, "SCAPS manual," ed: 26-11-2021
- [15] A. Niemegeers, S. Gillis, and M. Burgelman, "A user program for realistic simulation of polycrystalline heterojunction solar cells: SCAPS-1D," in *Proceedings of the 2nd World Conference on Photovoltaic Energy Conversion, JRC, European Commission, juli, 1998*, pp. 672-675.
- [16] H. Pauwels and G. Vanhoute, "The influence of interface state and energy barriers on the efficiency of heterojunction solar cells," *Journal of Physics D: Applied Physics*, vol. 11, p. 649, 1978.

Chapter 4:

Performances of CZTS TFSC using different HTLs Layer

4.1. Introduction

The exponential growth of the global population coupled with the pervasive use of an ever-expanding array of technological devices has driven an unprecedented surge in our planet's energy demand [1,2]. To meet this soaring need, vast quantities of fossil fuels are being consumed, exerting profound and detrimental effects on our fragile ecological system. The overreliance on conventional energy sources is depleting finite resources, and the environmental consequences are becoming increasingly apparent. Fortunately, renewable energy sources offer a lifeline, promising sustainable and eco-friendly solutions to the world's energy crisis [3,4]. Among these renewable sources, solar energy stands out as a beacon of hope [5–7]. Its renewable, sustainable, and costfree nature presents an opportunity to mitigate the global energy challenge. However, the key to harnessing the full potential of solar energy lies in the development of efficient methods for its capture and storage. It is imperative to advance the technology surrounding solar cells to generate electricity with minimal environmental impact [8–12]. Recent strides in science and technology have bolstered the likelihood of harnessing cost-effective, non-toxic materials characterized by a high absorption capacity for use in semiconductor technology [13]. Historically, the photovoltaic (PV) sector has been dominated by crystalline silicon, which accounted for over 90% of the industry. A fundamental aspect of solar cell design and manufacturing revolves around achieving a high conversion efficiency while minimizing material usage [14]. Solar cells serve as the pivotal bridge between solar photons and electricity, necessitating materials with exceptional light absorption capabilities. Copper zinc tin sulfide (CZTS), a naturally occurring absorber material, boasts a compelling set of advantages, including a direct band gap ranging from 1.4 to 1.6 eV, a remarkably high light absorption coefficient exceeding 10^4 cm^{-1} , cost-effective manufacturing methods, and consistent operational effectiveness. These attributes make CZTS an attractive candidate for large-scale production of thin-film solar cells (TFSCs) [15–21]. In fact, experimental CZTS solar cells have achieved an efficiency of 6.7% [20], while another study reported an 8.4% efficiency for TFSCs with a CZTS absorber derived from naturally available materials [22]. Furthermore, the incorporation of a

Zn_{1-x}Cd_xS buffer layer in CZTS solar cells led to a noteworthy power conversion efficiency (*PCE*) of 9.2% in practical conditions [22]. Notably, a sophisticated heterojunction device design involving Mo/MoS₂/CZTS/CdS/ZnO/ITO/MgF₂ achieved an efficiency of approximately 11%, with an open-circuit voltage (*V_{oc}*) of 0.73 V [23]. Nevertheless, additional research remains imperative, as CZTS solar cells only marginally surpass the efficiency of existing TFSCs.

This study's primary objective is to uncover the most effective means of enhancing the photovoltaic conversion efficiency (*PCE*) of CZTS-based solar devices. To achieve this, scientists are exploring the potential of incorporating a hole transport layer (HTL) within CZTS based solar cells. This innovative approach seeks to enhance carrier collection efficiency by reducing recombination at the rear-contact surface, all while preventing electrons from accessing the solar cell's back contacts while permitting the smooth flow of holes [24,25]. The electrical properties of CZTS-based photovoltaic devices are meticulously examined both in the absence of an HTL and in the presence of various HTL candidates. Simulations typically employ structures featuring front contacts like Al:ZnO, ZnO, CdS, CZTS, MoS₂, and rear contacts of MoS₂. These simulations aim to identify the most efficacious HTL material among the diverse candidates, including CuI, MoO_x, and SnS. Photovoltaic devices with CuI/CZTS, MoO_x/CZTS, and SnS/CZTS architectures are rigorously simulated and assessed using SCAPS-1D to evaluate key electrical parameters such as *V_{oc}*, *J_{sc}*, fill factor (*FF*), and power conversion efficiency (*PCE*) [26–28]. This study fills a critical gap in CZTS solar cell research by optimizing cell parameters and evaluating the performance of specific hole transport layers, achieving exceptional efficiency exceeding theoretical limits.

The chapter is structured as follows: first, the introduction elucidates the significance of CZTS solar cells and articulates the objectives of their advancement, underscoring the imperative for heightened efficiency. Subsequently, the literature review contextualizes the discussion by surveying prior investigations into CZTS solar cell technology. Following this, the methodology section meticulously outlines the simulation methodology employing the Scaps 1D simulator. The results and discussion section then accurately presents and dissects simulation outcomes, with a specific focus on the impact of various HTL candidates and design parameters on device performance. Finally, the conclusion encapsulates the discoveries, deliberates on their implications, and outlines potential avenues for future exploration.

4.2. Modeling framework

4.2.1. Solar cell structure

For the scope of this study, we adopted a solar cell structure inspired by the research conducted by Shin et al., which serves as our reference cell (see **Figure 4.1a**). To explore avenues for enhancing the device's efficiency, we implemented a series of modifications to the cell structure [22]. In our proposed configuration (see **Figure 1b**), we have introduced an innovative addition—an HTL (hole transport layer) comprising CuI, MoOx, and SnS positioned between the rear contact and the CZTS absorber layer. This alteration forms the focal point of our investigation into performance improvement.

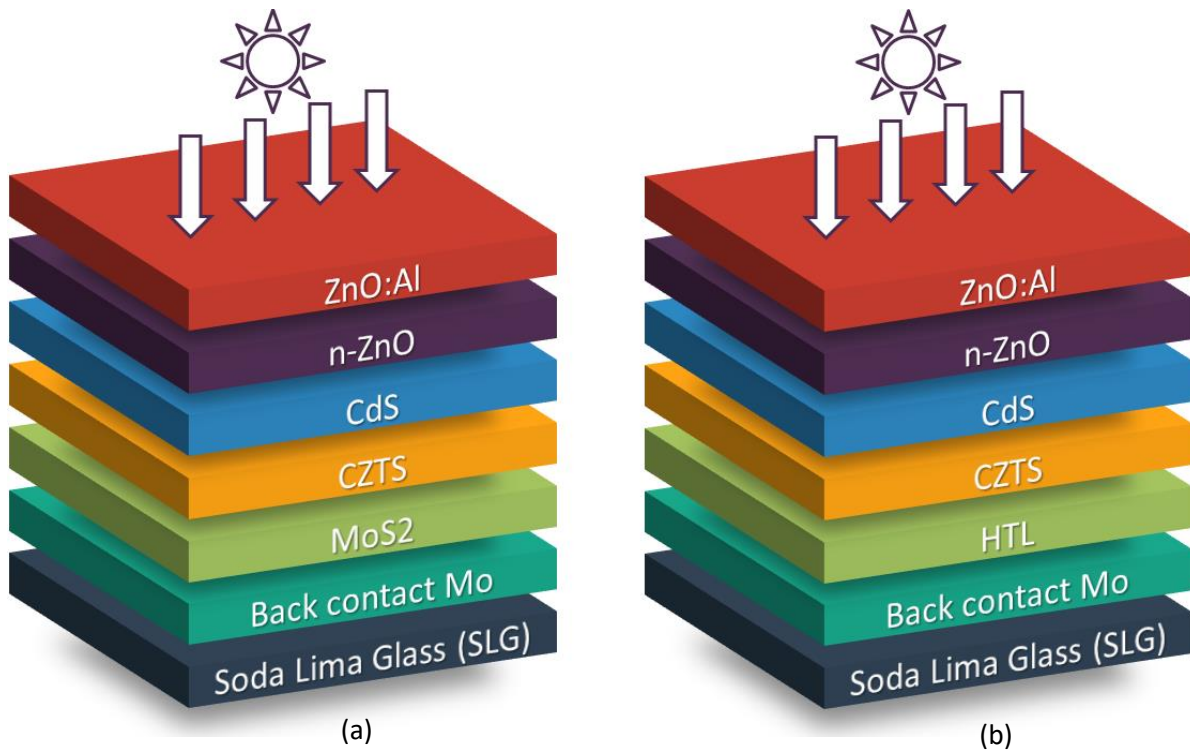


Figure 4.1: Schematic view of typical CZTS structures (a) conventional cell (b) proposed cell.

The experimental absorption coefficients of AZO, ZnO, CdS, and CZTS are shown in Figure 4.2. The extinction coefficient, which can be computed with the formula $\alpha = 4\pi k/\lambda$, is associated with these coefficients. Interference is not taken into account when complex optical constants are not present. It's crucial to remember that wavelength-dependent transmission and reflection can be implemented as optical filters at the front and rear contacts.

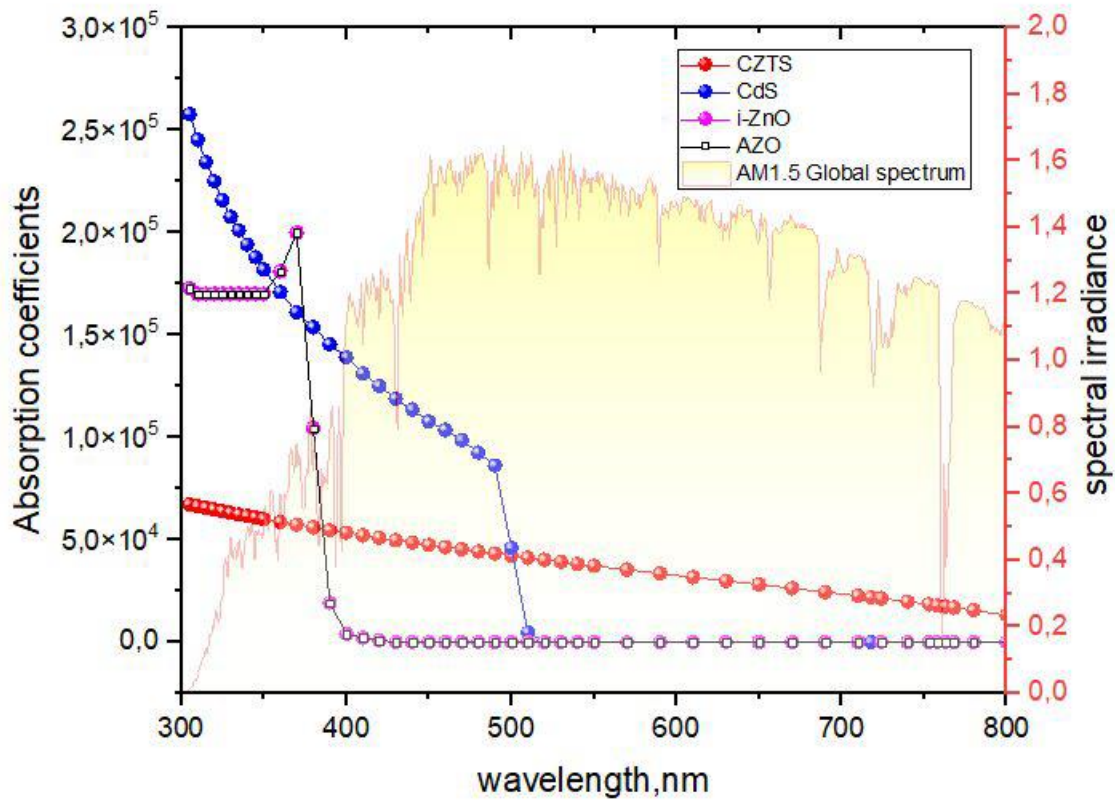


Figure 4.2: Absorption coefficients of different layers.

4.2.2. Modeling framework and Material Parameters

To develop a commercially viable device with enhanced conversion efficiencies and a deep understanding of its operational principles, it becomes imperative to establish a systematic numerical strategy that achieves several critical objectives: reducing manufacturing costs, shortening experimental timelines, and enhancing integration capabilities. In pursuit of these goals, computational simulations were performed using the freely available 1D Solar Cell Capacitance Simulator (SCAPS) software (version 3.3.10) developed by Gent University, Belgium, which is compatible with Windows [29–35].

SCAPS-1D stands out as a precision tool, taking into meticulous consideration a multitude of factors, including layer thickness, carrier concentration, defect density, buffer layers, metal work function, and the back Hole Transport Layer (HTL) [36–38]. It comprehensively addresses the complexities of semiconductor device behavior by solving the fundamental equations governing their operation, including the Poisson equation and continuity equations for both electrons and

holes, as depicted in Eqs (4.1)-(4.3) below [39]. This sophisticated software serves as a crucial tool in unraveling the intricate workings of our solar cell structure.

$$\frac{\delta}{\delta x} \left(\varepsilon_0 \varepsilon_R \frac{\delta \psi}{\delta x} \right) = -q \left(p - n + N_d^+ - N_A^- + \frac{\rho_{def}}{q} \right) \quad (4.1)$$

$$-\frac{\partial J_n}{\partial x} - R_n + G = \frac{\partial n}{\partial t} \quad (4.2)$$

$$-\frac{\partial J_p}{\partial x} - R_p + G = \frac{\partial p}{\partial t} \quad (4.3)$$

Here, we explore the complex physics of our solar cell through an analysis of important variables and formulas. Various physical quantities are represented by symbols in the context of these equations; the electrostatic potential is represented by ψ , and the relative permittivity of the semiconductor and vacuum permittivity are denoted by ε_0 . The symbols for the concentrations of free carriers are p and n . The densities of ionized acceptors and donors are denoted by N_A^- and N_d^+ . In addition, we introduce ρ_{def} , which stands for the defect charge density. G stands for the rate of photogeneration and R for the rate of net recombination in the cell.

The transport of charge carriers is elucidated through the interplay of diffusion and drift processes, encapsulated in the following equations:

$$J_n = -\frac{\mu_n n}{q} \frac{\partial E_{Fn}}{\partial x} \quad (4.4)$$

$$J_p = -\frac{\mu_p p}{q} \frac{\partial E_{Fp}}{\partial x} \quad (4.5)$$

Here, we investigate the details of our research using important parameters and notations, where the current density for holes and electrons is denoted by J_p and J_n , respectively. The mobility of electrons and holes is shown by μ_n and μ_p , respectively. The concentrations of free electrons and holes are denoted by the letters n and p , respectively.

The Fill Factor (FF) is a crucial parameter that determines how well solar cells operate. The formula for FF is a calculated comparison of the maximum power output (P_{max}) and the

theoretical power (P_t) that can be achieved under the conditions specified by the open-circuit voltage (V_{oc}) and the short-circuit current (J_{sc}). Equation (4.6) provides an explanation of this computation. In addition, a crucial parameter called Power Conversion Efficiency (PCE) measures the proportion of energy output produced by the solar cell to energy input from the sun. Eqs (4.7) provides a mathematical expression for this efficiency.

$$FF = \frac{P_{max}}{P_t} = \frac{V_{max}I_{max}}{V_{oc}J_{sc}} \quad (4.6)$$

$$PCE = \frac{V_{oc} J_{sc} FF}{P_{in}} \quad (4.7)$$

In this study, the physical parameters for various material layers were meticulously gathered from a combination of well-documented literature sources [23], theoretical considerations, and judicious estimation, as delineated in **Tables 4.1-4.4**.

We carried out the analysis for the CZTS solar cell simulation at an operational temperature of 300° K and a standard worldwide sun irradiance of 1.5AMG, or 1000 W/m².

Table 4.1: Back and front contact parameters. [16,22].

Cell Properties	Light	
Cell temperature	300 K	
Series resistance R_s	4.5 Ωcm^2	
Contacts	Front metal contact	Back metal contact
Metal work function (eV)	Flat band	Mo 5 eV
SRV of electron(cm/S)	10^7	10^5
SRV of hole (cm/S)	10^5	10^7

Table 4.2: Materials parameters used in the simulation [16,22, 40-43].

Parameters (units)	Al-ZnO	n-ZnO	n-CdS	p-CZTS	p-MoS ₂
Thickness (μm)	0.45	0.08	0.08	0.6	0.11
Bandgap (eV)	3.4	3.7	2.4	1.45	1.3
Electron affinity (eV)	4.51	4.5	4.11	4.1	4.5
Dielectric permittivity (relative)	9	9	10	7	10
Effective density of states N_c (cm^{-3})	$2.20 \times 10^{+18}$	$2.20 \times 10^{+18}$	$2.2 \times 10^{+19}$	$2.20 \times 10^{+18}$	$2.20 \times 10^{+18}$
Effective density of states N_v (cm^{-3})	$1.8 \times 10^{+19}$	$1.8 \times 10^{+19}$	$9.1 \times 10^{+18}$	$1.8 \times 10^{+19}$	$1.8 \times 10^{+19}$
Electron mobility (cm^2/Vs)	100	100	100	60	100
Hole mobility (cm^2/Vs)	25	25	25	10	25
Acceptor concentration, N_A (cm^{-3})	0	0	0	10^{+16}	$1.440 \times 10^{+18}$
Donor concentration, N_D (cm^{-3})	10^{+21}	10^{+18}	10^{+17}	0	0
Defect type at bulk/interface	-	-	-	Donor	-
Absorption coefficient (cm^{-1})	SCAPS data	SCAPS data	SCAPS data	5.10^4	SCAPS data

Table 4.3: Electrical properties of different HTL layers in solar cells [30, 44-46]

Parameters	CuI ⁴⁴	SnS ³⁰	MoOx ⁴⁶
Thickness (nm)	0.04-0.1	0.04-0.1	0.04-0.1
Bandgap (eV)	3.2	1.3	3
Electron affinity (eV)	2.1	4.2	2.5
Dielectric permittivity (relative)	6.5	12.5	12.5
Effective density of states N_c (cm^{-3})	1.92×10^{18}	1.0×10^{19}	2.2×10^{18}
Effective density of states N_v (cm^{-3})	2.24×10^{18}	4.13×10^{18}	1.8×10^{19}
Electron mobility (cm^2/Vs)	480	25	25
Hole mobility (cm^2/Vs)	43	100	100
Acceptor concentration, N_A (cm^{-3})	4.3×10^{16}	3×10^{18}	5×10^{18}
Donor concentration, N_D (cm^{-3})	0	0	0

Table 4.4: Defect parameters are used at different interfaces [16].

Parameters (unit)	CdS/CZTS	CZTS/CuI	CZTS/MoOx	CZTS/SnS
Defect type	Neutral	Neutral	Neutral	Neutral
Capture cross-section of electrons (cm^2)	10^{-15}	10^{-19}	10^{-19}	10^{-19}
Capture cross-section of holes (cm^2)	10^{-15}	10^{-19}	10^{-19}	10^{-19}
Reference for defect energy level E_t	above the highest E_v			
Energy with respect to reference (eV)	-0.120	0.6	0.6	0.6
Total density (cm^{-2})	10^{13}	10^{10}	10^{10}	10^{10}

4.3. Results and discussion

4.3.1. Prediction capabilities of the simulation setup

To facilitate a robust comparison and validation of our proposed technique, we conducted simulations mirroring the initial findings from an experimental solar cell, as reported in reference [22]. These simulations were carried out employing the SCAPS program, utilizing a curve-fitting approach to closely replicate the observed outcomes. The resulting J - V curve, illustrated in **Figure 4.3**, vividly demonstrates a noteworthy concurrence between the experimental and simulated results, underscoring the promise of the SCAPS software as a valuable tool for comprehending the behavior of CZTS-based photovoltaic devices. **Figure 4.3** vividly showcases the simulated and experimental current-voltage (J - V) characteristics. Notably, the CZTS defect density, measured at 10^{16} cm^{-3} , exhibits a compelling agreement between the experimental and simulated J - V curves, further attesting to the effectiveness of the SCAPS 1D program in modeling CZTS-based photovoltaic devices. The obtained values for J_{SC} , V_{OC} , FF , and PCE were found to be 20.18 mA/cm^2 , 0.674 V , 61.66% , and 8.4% , respectively. These results align closely with the experimental data presented by Shin in **Table 4.5**. It is worth acknowledging that the marginal differences between experimental [22] and our simulated results can be attributed to the inherent challenges in precisely determining real thickness, band gap (E_g), sheet resistance (R_s), and other physical parameters inherent to CZTS-based solar cells.

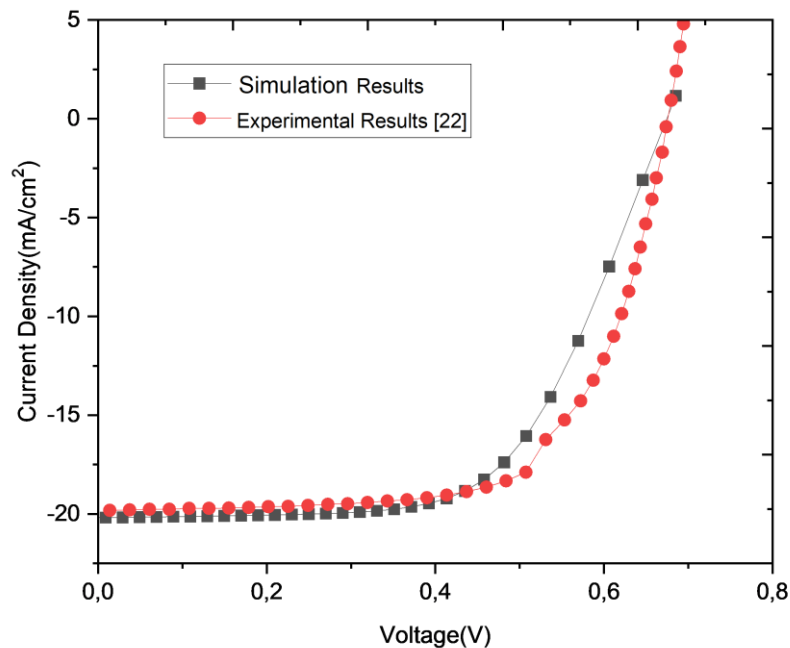


Figure 4.3: A comparison between simulated and real typical solar cells [22].

Table 4.5: Comparison of characteristics features between the experimental data [22] and our simulation results.

Solar cell parameters	V_{oc} (V)	J_{sc} (mA cm ⁻²)	FF (%)	Efficiency (%)
Experimental	0.661	19.5	65.8	8.4
Simulation	0.674	20.18	61.66	8.4

4.3.2. Optimization of conventional solar cell

4.3.2.1. Exploring the Impact of MoS₂ Thickness and CZTS on Conventional Solar Cell Properties

It is widely recognized that the characteristics of the absorber layer, particularly its thickness and carrier concentration, play a pivotal role in enhancing solar cell efficiency. This is primarily because an excessively thick absorber layer can trigger recombination currents within the bulk, whereas an overly thin one may lead to inadequate light absorption. Consequently, the absorber layer emerges as a critical determinant capable of either significantly enhancing or detrimentally affecting solar cell performance.

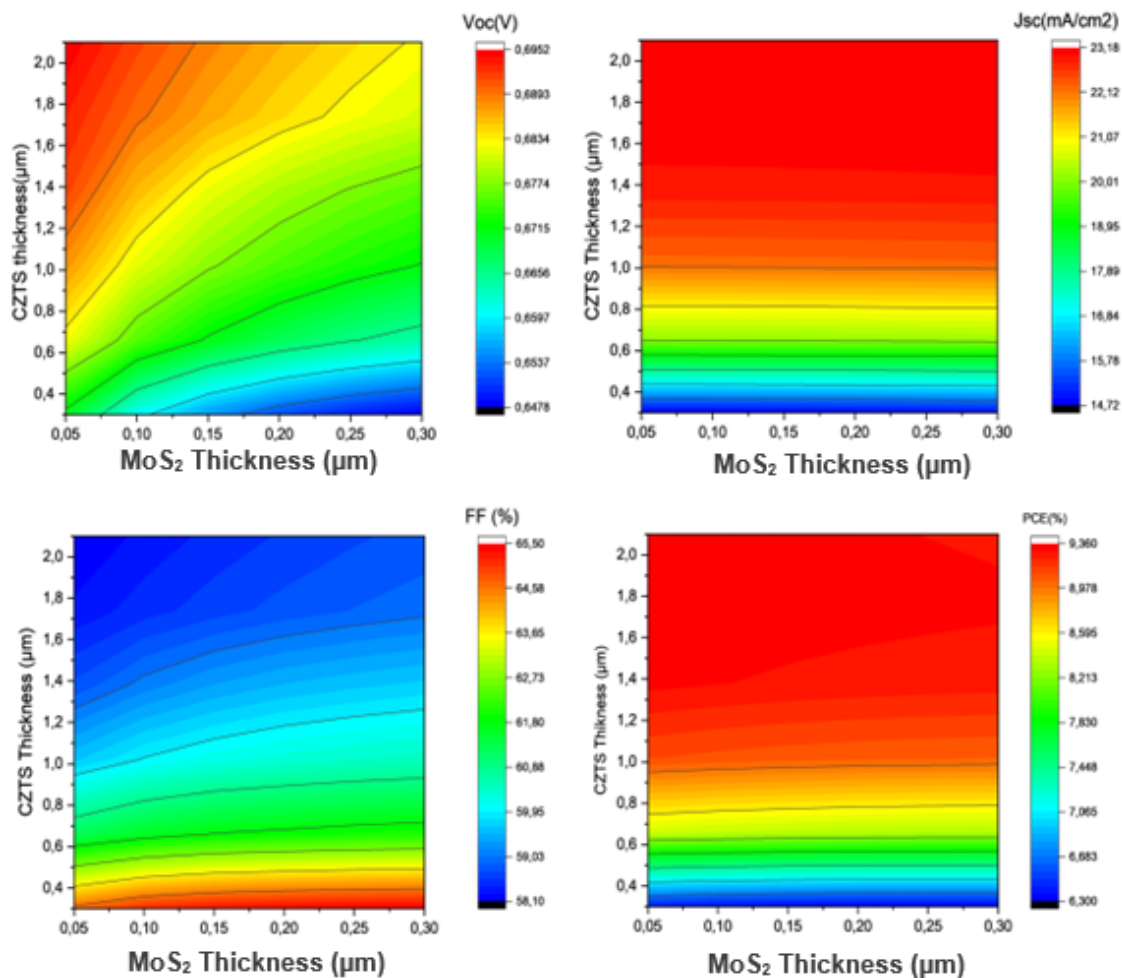


Figure 4.4: PV performance parameters depend on the thickness of MoS₂ and CZTS layers.

Illustrated in **Figure 4.4** is a contour plot showing the interplay between CZTS absorber thickness and MoS₂ layer thickness, and how these variables impact the device's performance metrics. Notably, the data reveals that within the absorber thickness range of 0.2 μm to 2.2 μm and MoS₂ thickness range of 0.05 μm to 0.3 μm, alterations in these dimensions had negligible effects on the device's overall performance.

4.3.2.2. Effect of CZTS and MoS₂ Acceptor density on the conventional solar cell characteristics

In this research, we delved into the impact of MoS₂ and CZTS carrier concentrations on the performance characteristics of CZTS solar cells employing sum modulation gating. Additionally, we accounted for the experimental parasitic resistance documented in prior studies [40]. As illustrated in Figure 4.5, we achieved a maximum efficiency of 10.55%, with corresponding values of V_{oc} at 0.774 V, J_{sc} at 20.1 mA/cm², and FF at 64.95%. Notably, these optimal performance metrics were attained at CZTS and MoS₂ carrier concentrations of 10¹⁸ cm³ and 10¹⁹ cm³, respectively. It's worth highlighting that our results closely mirror the highest efficiency achieved for CZTS in earlier investigations [24]. Slight variations can be attributed to disparities in bandgap energy (E_g), thickness, and defect concentration. However, two prominent factors emerge as key contributors to the reduced efficiency observed in CZTS-based solar cells. Firstly, the significant concentration of defects ($\sim 10^{16}$ cm³) within the carrier, and secondly, the type of contacts formed with the bottom metal work function (Mo), resulting in heightened resistance. To enhance the efficiency of CZTS solar cells, we advocate, in the subsequent section, the adoption of MoOx, SnS, and CuI hole transport layers as the back surface field, complemented by Au serving as the bottom contact. Furthermore, we will investigate how CZTS defect density and parasitic resistance affect CZTS solar cell performance.

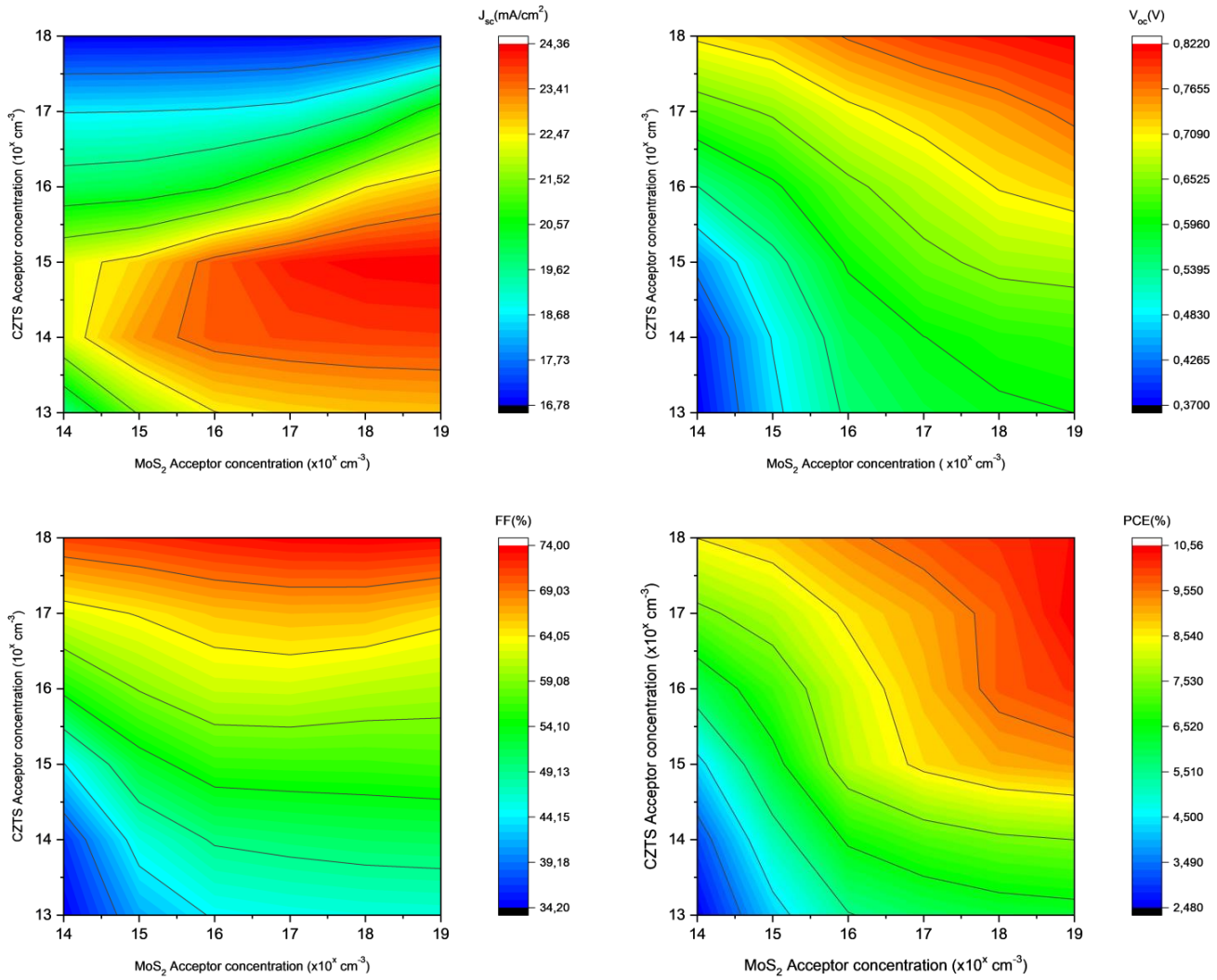


Figure 4.5: The acceptor density of the MoS₂ layer and CZTS absorber determines the PV performance characteristics.

4.3.2.3. Impacts of bulk defect density of absorber on PV performances

The presence of defects within the absorber layer constitutes a critical factor influencing the attainment of exceptional photovoltaic performance. In the realm of thin-film solar cells (TFSCs), the optoelectronic properties of the absorber material can undergo alterations due to the presence of these defect states. Consequently, achieving a highly efficient CZTS solar cell necessitates a thorough assessment of the quality of the absorber material. Within the scope of this study, we meticulously examine the influence of absorber defect density on key photovoltaic performance parameters, as showed in **Figure 4.6**. The absorber defect density is systematically varied across a range spanning from 10^{12} to 10^{17} cm⁻³ while maintaining other relevant parameters at their optimized values. The results reveal a consistent decline in efficiency as the

defect density increases from 10^{12} to 10^{17} cm^{-3} . Notably, a precipitous decline in efficiency becomes evident beyond a defect density of 10^{16} cm^{-3} . This observable degradation in photovoltaic output at higher defect densities can be attributed to the increased likelihood of carrier recombination losses occurring at localized energy centers within the heterojunction. As a result, it becomes apparent that the photovoltaic performance is notably compromised at higher absorber defect densities. To optimize device performance, we have identified the optimal defect density for the envisioned CZTS solar structure, combined with the Hole Transport Layer (HTL), to be 10^{12} cm^{-3} .

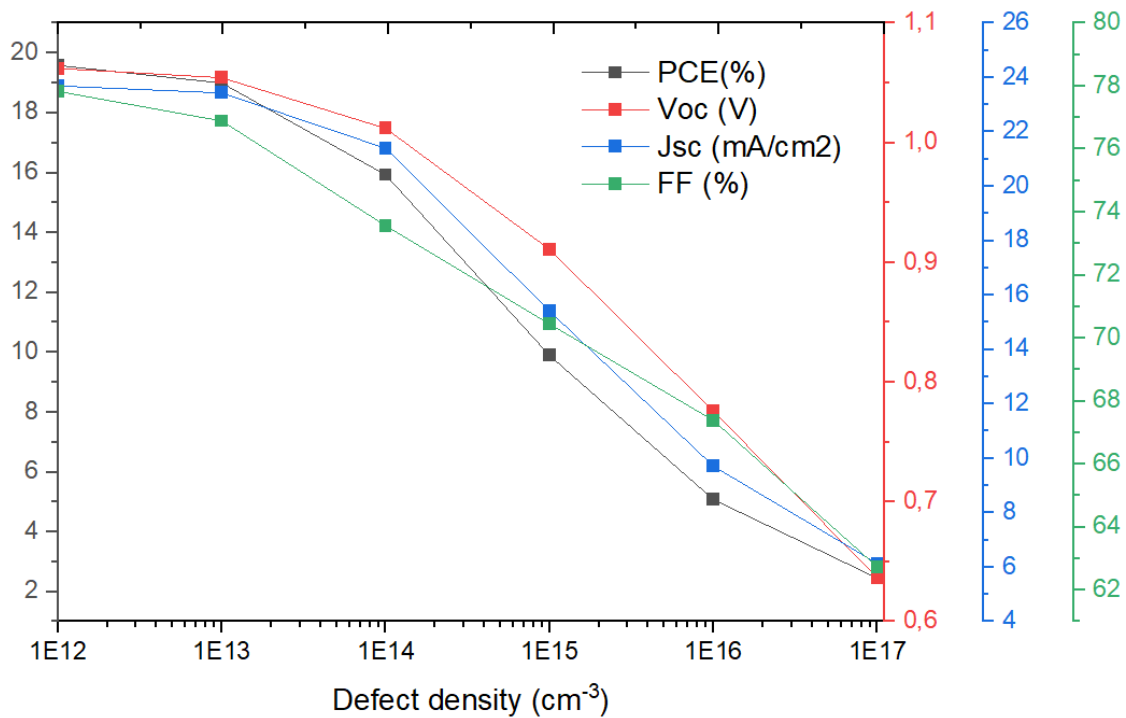


Figure 4.6: Impact of absorber defect density on the suggested CZTS solar cell's efficiency using HTL.

4.3.2.4. Impacts of Back contact work function and Temperature on solar cell performances

The work function of the back contact holds a pivotal role in shaping the photovoltaic (PV) performance of our solar cell. In our simulations, we explored the influence of the back contact work function, ranging from 4.6 to 5.6 eV, on the key parameters of the proposed PV structure. The outcomes, detailed in **Figure 4.7**, unveil an interesting trend: V_{oc} , FF , and efficiency exhibit a linear increase with the work function up to 5 eV, after which they reach a saturation point. Conversely, J_{sc} remains relatively constant as the back contact metal work function increases.

This behavior aligns with observations from previous studies on thin-film solar cells (TFSCs). The augmentation of the back metal contact's work function above 5.0 eV is shown to reduce the energy barrier height, facilitating the smoother transport of the majority of charge carriers (in this case, holes) from the absorber layer. Consequently, this enhancement substantially improves cell efficiency [47-49]. These results underscore the importance of a back electrode with a work function exceeding 5.0 eV to achieve high efficiency in CZTS TFSCs. Taking cost and material efficiency into account, we have chosen gold (Au) as the back metal contact, with a work function of 5.4 eV.

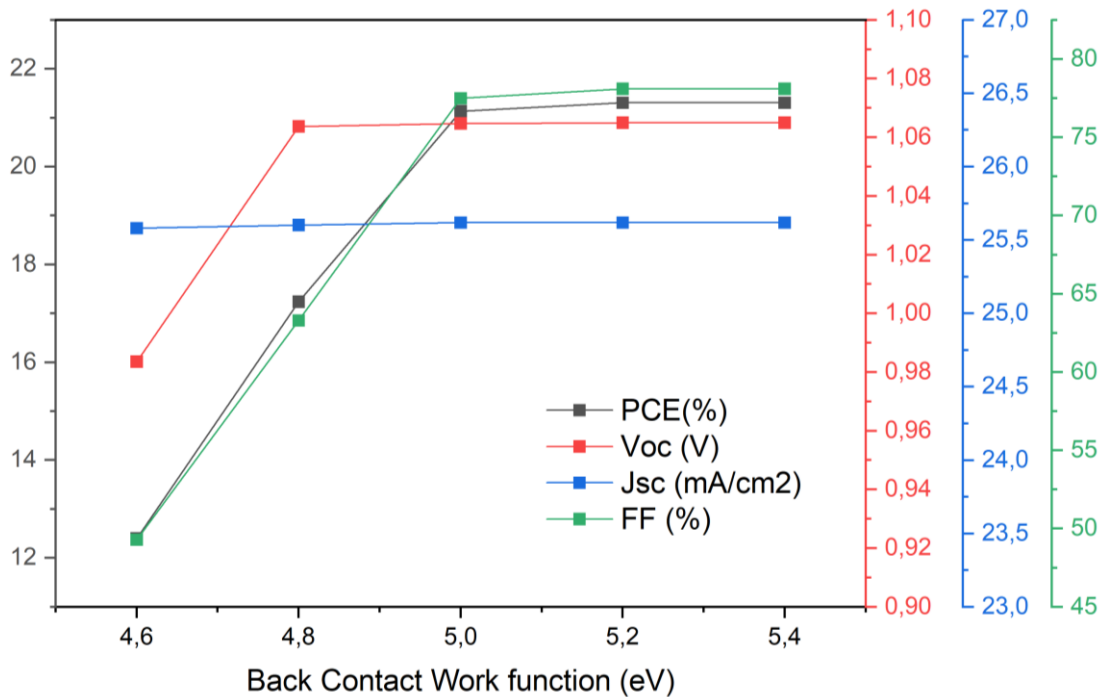


Figure 4.7: Influence of Back Contact Work Function on the Photovoltaic Performance Metrics of CZTS Solar Cells.

In a parallel simulation, we explored the impact of temperature across the range of 275 to 425 K to evaluate the thermal resilience of our proposed CZTS-based solar cell, maintaining the optimized physical parameters for various layers as discussed earlier.

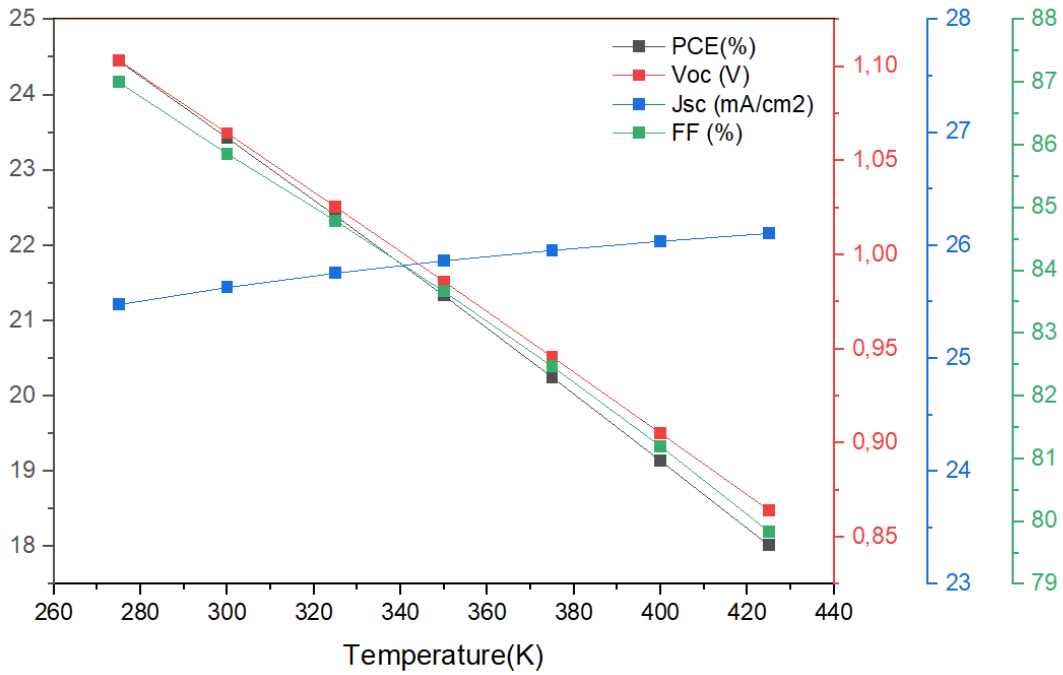


Figure 4.8: Impact of operation temperature on the suggested CZTS solar cell's PV performance characteristics.

Figure 4.8 illustrates the influence of temperature on V_{OC} , J_{SC} , FF , and efficiency. It becomes evident that V_{OC} , FF , and efficiency experience a steady decline as the operating temperature increases. The elevated temperature results in a higher generation of electron-hole pairs, which, in turn, amplifies recombination rates between energy bands [50][51]. This surge in the internal recombination rates elevates the reverse saturation current, consequently diminishing V_{OC} . However, there is a slight increase in J_{SC} with rising temperature, a behavior consistent with previous research findings [48-51]. This phenomenon can be attributed to the reduction in the energy band gap of semiconductors within the heterojunction TFSC as the temperature increases. The combined effects of V_{OC} and J_{SC} translate to a decline in PCE and FF . Specifically, FF decreases from 87% at 275 K to 78% at 425 K. Consequently, cell efficiency is calculated at 24.65% and 18.27% at 275 K and 425 K, respectively.

4.3.2.5. Impacts of series resistance on cell performances

The series resistance (R_s) stands as a pivotal factor in shaping the photovoltaic characteristics of solar cells. Hence, in our quest to optimize cell performance, it becomes imperative to assess the influence of R_s . In this context, we conducted simulations on the proposed CZTS solar cell with a MoOx HTL, while keeping the previously optimized parameters fixed. We systematically

varied R_s across a range spanning from 0 to 5 $\Omega\cdot\text{cm}^2$ to scrutinize its impact on key PV performance parameters, as illustrated in **Figure 4.9**.

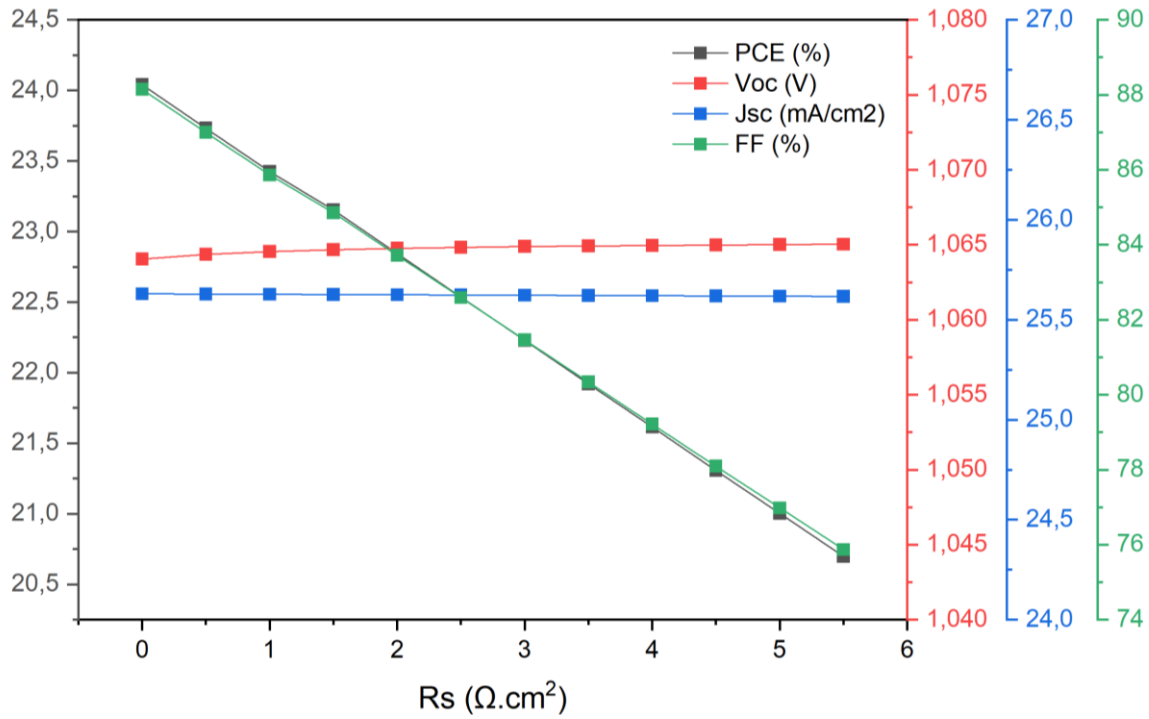


Figure 4.9: Impact of series resistance on the suggested CZTS solar cell's PV performance metrics.

It's evident from this Figure that Voc (open-circuit voltage) and Jsc (short-circuit current) exhibit minimal sensitivity to changes in R_s . However, there is a noticeable decline in efficiency, dropping from 24.04% to 20.69%, as R_s increases. The most significant impact is observed in the fill factor (FF), which experiences a substantial decrease, plummeting from 88.15% to 75.56% with higher R_s values. This reduction in FF plays a dominant role in the overall decrease in efficiency [51]. In conclusion, both the R_s and its associated impact on the FF are fundamental determinants of photovoltaic performance in solar cells. Therefore, it is essential to maintain R_s at lower values to optimize the cell's efficiency.

4.3.3. HTL candidates' examination

In order to show the importance of the HTL layer in improving the solar cell performance in terms of separation and collection mechanisms. **Figure 4.10** shows the electric field variation for both investigated structures with and without HTL.

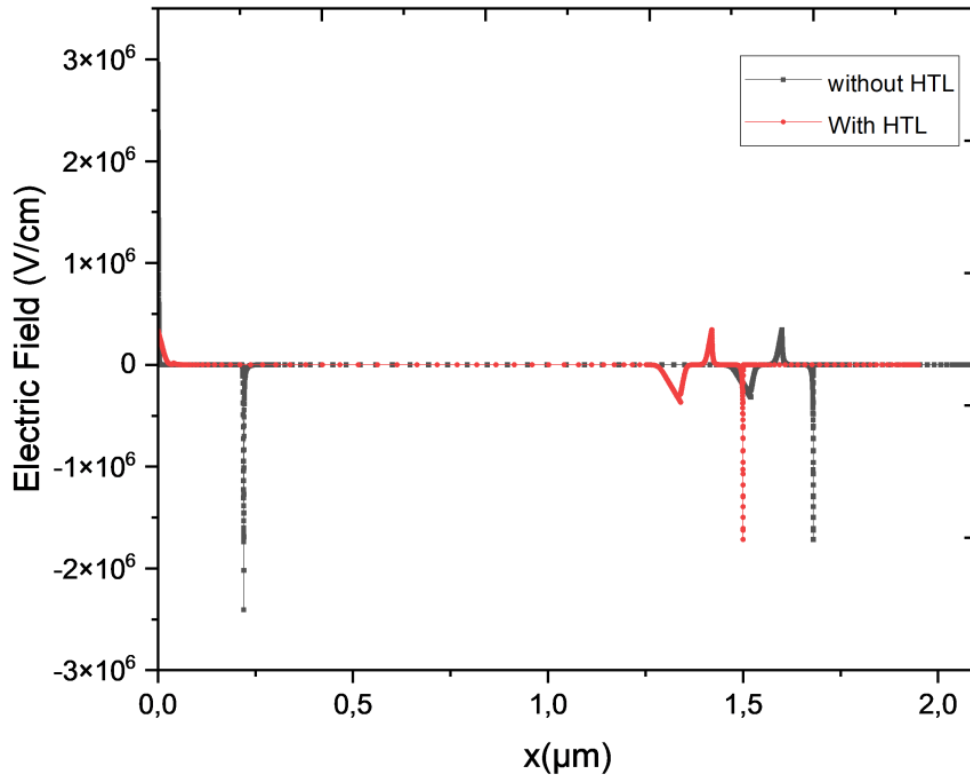


Figure 4.10: Electric field variation throughout the structure with and without HTL.

The influence of MoOx/Au, CuI/Au, and SnS/Au on the light (J-V) characteristics of CZTS thin film solar cells is illustrated in **Figure 4.11**. Notably, we observe a significant improvement in the power conversion efficiency (PCE), escalating from 10.55% in the CZTS solar cell with MoS₂ [24] to 16.03%, 15.37%, and 13.9% respectively, for the same solar cell but incorporating different hole transport layers (HTLs) (refer to Table 4.6). This observation suggests that the HTL reflector layer enhances the open-circuit voltage (V_{OC}) and overall efficiency of CZTS-based solar cells. Besides, high V_{OC} is remarked for structures with HTLs when compared to the HTL-less device. This fact is due mainly to the reduction of charge carrier recombination rates and the facilitation of efficient carrier extraction at the rear-contact surface, thus minimizing electron loss while permitting smooth hole flow, resulting in a pronounced boost in V_{OC} .

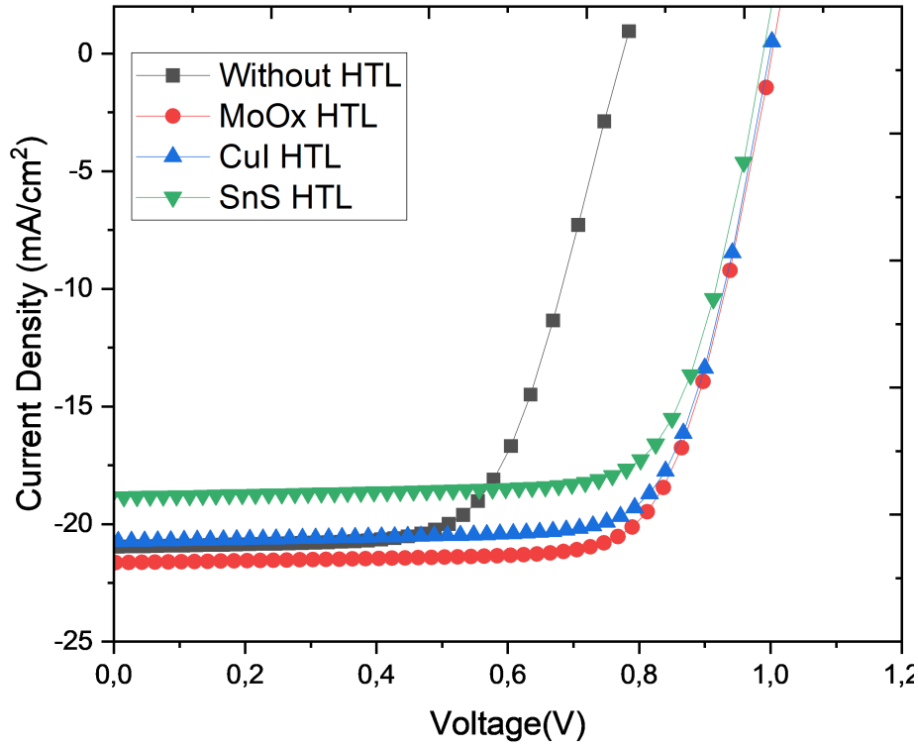


Figure 4.11: Simulated J-V characteristics of CZTS solar cells with different HTL candidates.

The investigated CZTS solar cells using MoOx and CuI as HTL materials achieve an efficiency of 16% and 15% respectively. This fact is due mainly to the electronic properties of these materials. This later enhances the V_{OC} of both devices compared to conventional [52-56]. Besides, **Figure 4.12** presented the good alignment of both materials where a high electron barrier is established CZTS/MoOx and CZTS/CuI at interfaces and reduces the interfacial recombination effect. It can be seen from this figure that the CZTS/MoOx and CZTS/CuI interface show a spike-like configuration that creates a barrier for electrons and ensures a smooth passage of holes to the HTL layers. On the other hand, SnS and MoS₂ establish a cliff-like configuration and show a reduced barrier against electrons which boosts the recombination phenomenon at the interface.

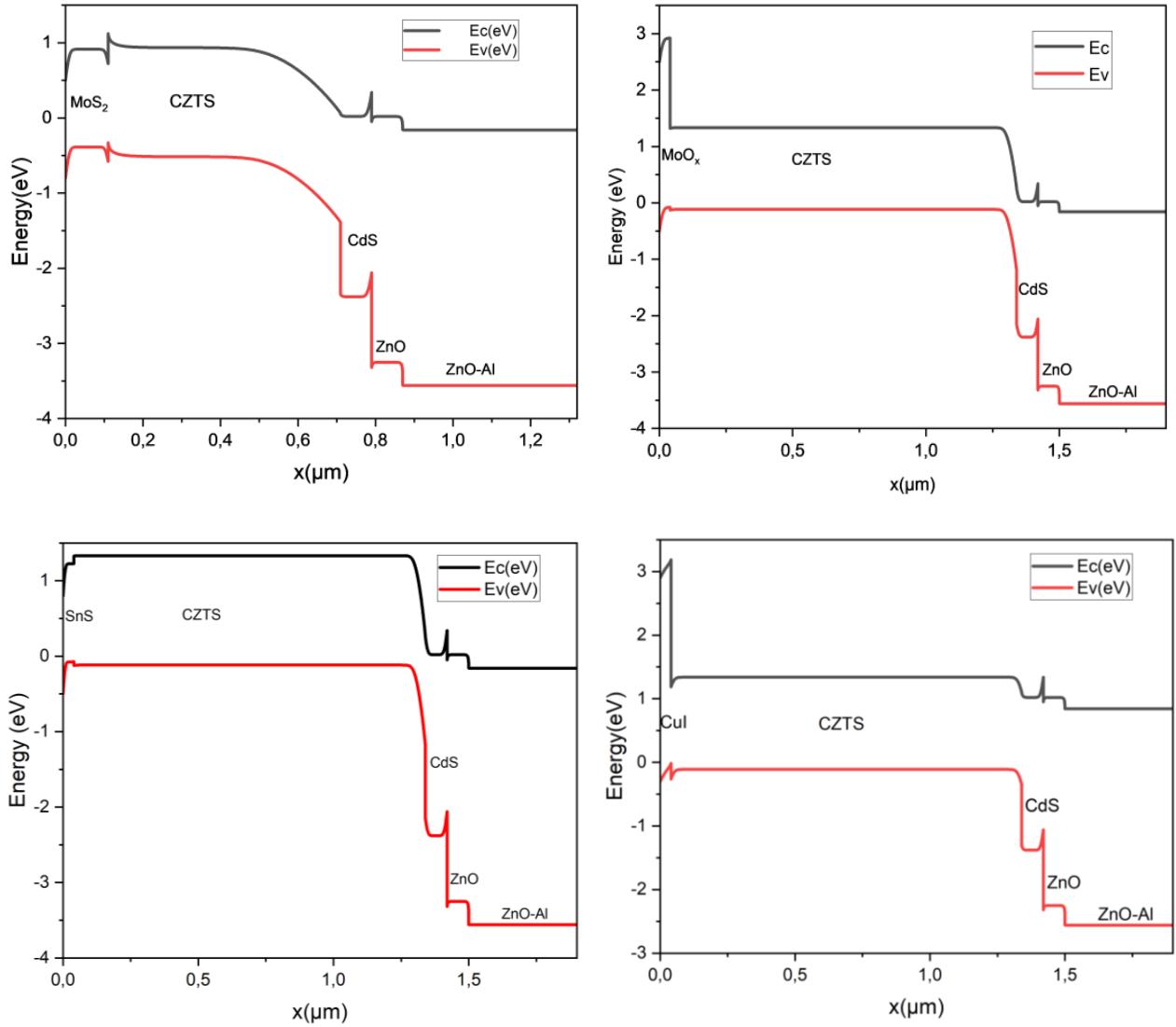


Figure 4.12: Band diagram energy of CZTS solar cells of conventional and proposed cells.

Table 4.6: Output parameters of various CZTS solar cell structures.

Device architectures	V_{oc} (V)	J_{sc} (mA/cm ²)	FF (%)	Efficiency (%)
Mo/MoS ₂ /CZTS/CdS/ZnO/ZnO-Al	0.774	20.1	69.27	10.55 [24]
Zn _{1-x} Cd _x S/ CZTS	0.747	19.5	63.2	9.2 [57]
Zn _{1-x} Sn _x O _y /CZTS	0.679	21.6	61.4	9.0 [58]
CdS/CZTS	0.582	27.72	69.7	11.23 [59]
CZTS/(Cd,Zn)S	0.39	35.4	61.5	8.7 [60]
Mo/MoO _x /CZTS/CdS/ZnO/ZnO-Al	1.01	21.39	74.00	16,03 (this work)
Mo/CuI/CZTS/CdS/ZnO/ZnO-Al	1.00	20.82	73.87	15.37 (this work)
Mo/SnS/CZTS/CdS/ZnO/ZnO-Al	0.99	18.85	74.32	13.9 (this work)

4.4. Conclusion

In summary, our investigation has explored the captivating potential of employing hole transport layers (HTLs), specifically MoOx and CuI, in conjunction with SnS, to significantly enhance the performance of CZTS-based solar cells. Our study extended beyond the conventional boundaries by intricately fine-tuning critical cell parameters, encompassing CZTS absorber layer thickness, defect density, and acceptor concentration. The introduction of these HTLs yielded a dual advantage: augmentation in photon energy absorption and a notable reduction in recombination rates. Notably, MoOx and CuI exhibited exceptional prowess as HTLs, surpassing SnS by a considerable margin. This superiority manifested in an impressive power conversion efficiency of 23.73% and an exceptional fill factor of 88%. These remarkable outcomes align remarkably closely with the theoretical limits laid out by Shockley-Queisser, adding to the intrigue of our findings. This revelation not only signals the possibility of enhancing the efficiency of CZTS hetero-junction based solar cells but also ushers in the prospect of a more sustainable and efficient era in solar energy conversion. This breakthrough holds promise for real-world applications in renewable energy technology, paving the way for a brighter and greener future.

References

- [1] Pervez, M. F.; Mia, M. N. H.; Hossain, S.; Saha, S. M. K.; Ali, M. H.; Sarker, P.; Hossain, M. K.; Matin, M. A.; Hoq, M.; Chowdhury, M. A. M. Influence of Total Absorbed Dose of Gamma Radiation on Optical Bandgap and Structural Properties of Mg-Doped Zinc Oxide. *Optik (Stuttg)*. **2018**, *162*, 140–150.
- [2] Bencherif, H.; Khalid Hossain, M. Design and Numerical Investigation of Efficient (FAPbI₃)_{1-x}(CsSnI₃)_x Perovskite Solar Cell with Optimized Performances. *Sol. Energy* **2022**, *248*, 137–148.
- [3] Lenferna, G. A. Can We Equitably Manage the End of the Fossil Fuel Era? *Energy Res. Soc. Sci.* **2018**, *35*, 217–223.
- [4] Hassan, Q.; Viktor, P.; J. Al-Musawi, T.; Mahmood Ali, B.; Algburi, S.; Alzoubi, H. M.; Khudhair Al-Jiboory, A.; Zuhair Sameen, A.; Salman, H. M.; Jaszczur, M. The Renewable Energy Role in the Global Energy Transformations. *Renew. Energy Focus* **2024**, *48*, 100545.
- [5] Hossain, M. K.; Rahman, M. T.; Basher, M. K.; Afzal, M. J.; Bashar, M. S. Impact of Ionizing Radiation Doses on Nanocrystalline TiO₂ Layer in DSSC's Photoanode Film. *Results Phys.* **2018**, *11* (September), 1172–1181.
- [6] Hossain, M. K.; Mortuza, A. A.; Sen, S. K.; Basher, M. K.; Ashraf, M. W.; Tayyaba, S.; Mia, M. N. H.; Uddin, M. J. A Comparative Study on the Influence of Pure Anatase and Degussa-P25 TiO₂ Nanomaterials on the Structural and Optical Properties of Dye Sensitized Solar Cell (DSSC) Photoanode. *Optik (Stuttg)*. **2018**, *171* (March), 507–516.
- [7] Khalid Hossain, M.; Pervez, M. F.; Jalal Uddin, M.; Tayyaba, S.; Mia, M. N. H.; Bashar, M. S.; Jewel, M. K. H.; Haque, M. A. S.; Hakim, M. A.; Khan, M. A.; Hossain, M. K.; Pervez, M. F.; Uddin, M. J.; Tayyaba, S.; Mia, M. N. H.; Bashar, M. S.; Jewel, M. K. H.; Haque, M. A. S.; Hakim, M. A.; Khan, M. A. Influence of Natural Dye Adsorption on the Structural, Morphological and Optical Properties of TiO₂ Based Photoanode of Dye Sensitized Solar Cell. *Mater. Sci. Pol.* **2018**, *36* (1), 93–101.
- [8] Basher, M. K.; Hossain, M. K.; Uddin, M. J.; Akand, M. A. R.; Shorowordi, K. M. Effect of Pyramidal Texturization on the Optical Surface Reflectance of Monocrystalline Photovoltaic Silicon Wafers. *Optik (Stuttg)*. **2018**, *172*, 801–811.
- [9] Hossain, M. K.; Pervez, M. F.; Mia, M. N. H.; Mortuza, A. A.; Rahaman, M. S.; Karim, M. R.; Islam, J. M. M.; Ahmed, F.; Khan, M. A. Effect of Dye Extracting Solvents and Sensitization Time on Photovoltaic Performance of Natural Dye Sensitized Solar Cells. *Results Phys.* **2017**, *7*, 1516–1523.
- [10] Basher, M. K.; Hossain, M. K.; Akand, M. A. R. Effect of Surface Texturization on Minority Carrier Lifetime and Photovoltaic Performance of Monocrystalline Silicon Solar Cell. *Optik (Stuttg)*. **2019**, *176* (September 2018), 93–101.
- [11] Hossain, M. I.; Qarony, W.; Hossain, M. K.; Debnath, M. K.; Uddin, M. J.; Tsang, Y. H. Effect of Back Reflectors on Photon Absorption in Thin-Film Amorphous Silicon Solar Cells. *Appl. Nanosci.* **2017**, *7* (7), 489–497

- [12] Hossain, M. K.; Samajdar, D. P.; Das, R. C.; Arnab, A. A.; Rahman, M. F.; Rubel, M. H. K.; Islam, M. R.; Bencherif, H.; Pandey, R.; Madan, J.; Mohammed, M. K. A. Design and Simulation of Cs₂BiAgI₆ Double Perovskite Solar Cells with Different Electron Transport Layers for Efficiency Enhancement. *Energy & Fuels* **2023**, *37* (5), 3957–3979.
- [13] Basher, M. K.; Nur-E-Alam, M.; Rahman, M. M.; Alameh, K.; Hinckley, S. Aesthetically Appealing Building Integrated Photovoltaic Systems for Net-Zero Energy Buildings. Current Status, Challenges, and Future Developments—A Review. *Buildings* **2023**, *13* (4), 863.
- [14] Kumar Dakua, P.; Kumar Panda, D. Influence of Dopants in the Buffer Layer on CZTS Solar Cell Performance. *Emerg. Mater. Res.* **2022**, *11* (4), 478–485.
- [15] Li, Y.; Ru, X.; Yang, M.; Zheng, Y.; Yin, S.; Hong, C.; Peng, F.; Qu, M.; Xue, C.; Lu, J.; Fang, L.; Su, C.; Chen, D.; Xu, J.; Yan, C.; Li, Z.; Xu, X.; Shao, Z. Flexible Silicon Solar Cells with High Power-to-Weight Ratios. *Nature* **2024**, *626* (7997), 105–110.
- [16] Haddout, A.; Fahoume, M.; Qachaou, A.; Raidou, A.; Lharch, M.; Elharfaoui, N. Influence of Composition Ratio on the Performances of Kesterite Solar Cell with Double CZTS Layers—A Numerical Approach. *Sol. Energy* **2019**, *189*, 491–502.
- [17] Qiu, L.; Xu, J.; Cai, W.; Xie, Z.; Yang, Y. Fabrication of Cu₂ZnSnS₄ Thin Films by Microwave Assisted Sol-Gel Method. *Superlattices Microstruct.* **2019**, *126*, 83–88.
- [18] Chamekh, S.; Khemiri, N.; Kanzari, M. Effect of Annealing under Different Atmospheres of CZTS Thin Films as Absorber Layer for Solar Cell Application. *SN Appl. Sci.* **2020**, *2* (9), 1507.
- [19] Gunavathy, K. V.; Tamilarasan, K.; Rangasami, C.; Arulanantham, A. M. S. Effect of Solvent on the Characteristic Properties of Nebulizer Spray Pyrolyzed Cu₂ZnSnS₄ Absorber Thin Films for Photovoltaic Application. *Thin Solid Films* **2020**, *697*, 137841.
- [20] Bade, B. R.; Rondiya, S. R.; Jadhav, Y. A.; Kamble, M. M.; Barma, S. V.; Jathar, S. B.; Nasane, M. P.; Jadkar, S. R.; Funde, A. M.; Dzade, N. Y. Investigations of the Structural, Optoelectronic and Band Alignment Properties of Cu₂ZnSnS₄ Prepared by Hot-Injection Method towards Low-Cost Photovoltaic Applications. *J. Alloys Compd.* **2021**, *854*, 157093.
- [21] Camara, S. M.; Wang, L.; Zhang, X. Easy Hydrothermal Preparation of Cu₂ZnSnS₄ (CZTS) Nanoparticles for Solar Cell Application. *Nanotechnology* **2013**, *24* (49), 495401.
- [22] Shin, B.; Gunawan, O.; Zhu, Y.; Bojarczuk, N. A.; Chey, S. J.; Guha, S. Thin Film Solar Cell with 8.4% Power Conversion Efficiency Using an Earth-abundant Cu₂ZnSnS₄ Absorber. *Prog. Photovoltaics Res. Appl.* **2013**, *21* (1), 72–76.
- [23] Sun, K.; Yan, C.; Liu, F.; Huang, J.; Zhou, F.; Stride, J. A.; Green, M.; Hao, X. Over 9% Efficient Kesterite Cu₂ZnSnS₄ Solar Cell Fabricated by Using Zn_{1-x}Cd_xS Buffer Layer. *Adv. Energy Mater.* **2016**, *6* (12).
- [24] Yan, C.; Huang, J.; Sun, K.; Johnston, S.; Zhang, Y.; Sun, H.; Pu, A.; He, M.; Liu, F.; Eder, K.; Yang, L.; Cairney, J. M.; Ekins-Daukes, N. J.; Hameiri, Z.; Stride, J. A.; Chen, S.; Green, M. A.; Hao, X. Cu₂ZnSnS₄ Solar Cells with over 10% Power Conversion Efficiency Enabled by Heterojunction Heat Treatment. *Nat. Energy* **2018**, *3* (9), 764–772.

- [25] Kumar, A.; Ranjan, P. Computational Analysis of Chalcogenides as an Inorganic Hole Transport Layer in Perovskite Solar Cells. *Opt. Quantum Electron.* **2021**, *53* (9), 511.
- [26] Hossain, M. K.; Ishraque Toki, G. F.; Samajdar, D. P.; Rubel, M. H. K.; Mushtaq, M.; Islam, M. R.; Rahman, M. F.; Bhattarai, S.; Bencherif, H.; Mohammed, M. K. A.; Pandey, R.; Madan, J. Photovoltaic Performance Investigation of Cs₃Bi₂I₉-Based Perovskite Solar Cells with Various Charge Transport Channels Using DFT and SCAPS-1D Frameworks. *Energy & Fuels* **2023**, *37* (10), 7380–7400.
- [27] Hossain, M. K.; Toki, G. F. I.; Kuddus, A.; Mohammed, M. K. A.; Pandey, R.; Madan, J.; Bhattarai, S.; Rahman, M. F.; Dwivedi, D. K.; Amami, M.; Bencherif, H.; Samajdar, D. P. Optimization of the Architecture of Lead-Free CsSnCl₃-Perovskite Solar Cells for Enhancement of Efficiency: A Combination of SCAPS-1D and WxAMPS Study. *Mater. Chem. Phys.* **2023**, *308*, 128281.
- [28] Hossain, M. K.; Bhattarai, S.; Arnab, A. A.; Mohammed, M. K. A.; Pandey, R.; Ali, M. H.; Rahman, M. F.; Islam, M. R.; Samajdar, D. P.; Madan, J.; Bencherif, H.; Dwivedi, D. K.; Amami, M. Harnessing the Potential of CsPbBr₃-Based Perovskite Solar Cells Using Efficient Charge Transport Materials and Global Optimization. *RSC Adv.* **2023**, *13* (30), 21044–21062.
- [29] Cherouana, A.; Labbani, R. Numerical Simulation of CZTS Solar Cell with Silicon Back Surface Field. *Mater. Today Proc.* **2018**, *5* (5), 13795–13799.
- [30] Omrani, M. K.; Minbashi, M.; Memarian, N.; Kim, D.-H. Improve the Performance of CZTSSe Solar Cells by Applying a SnS BSF Layer. *Solid. State. Electron.* **2018**, *141*, 50–57.
- [31] Yan, C.; Sun, K.; Liu, F.; Huang, J.; Zhou, F.; Hao, X. Boost Voc of Pure Sulfide Kesterite Solar Cell via a Double CZTS Layer Stacks. *Sol. Energy Mater. Sol. Cells* **2017**, *160*, 7–11.
- [32] Polman, A.; Knight, M.; Garnett, E. C.; Ehrler, B.; Sinke, W. C. Photovoltaic Materials: Present Efficiencies and Future Challenges. *Science* (80-.). **2016**, *352* (6283).
- [33] Amin, N.; Hossain, M. I.; Chelvanathan, P.; Mukter Uzzaman, A. S. M.; Sopian, K. Prospects of Cu₂ZnSnS₄ (CZTS) Solar Cells from Numerical Analysis. In *International Conference on Electrical & Computer Engineering (ICECE 2010)*; IEEE, 2010; pp 730–733.
- [34] Jhuma, F. A.; Shaily, M. Z.; Rashid, M. J. Towards High-Efficiency CZTS Solar Cell through Buffer Layer Optimization. *Mater. Renew. Sustain. Energy* **2019**, *8* (1), 6.
- [35] Khattak, Y. H.; Baig, F.; Toura, H.; Ullah, S.; Marí, B.; Beg, S.; Ullah, H. Effect of CZTSe BSF and Minority Carrier Life Time on the Efficiency Enhancement of CZTS Kesterite Solar Cell. *Curr. Appl. Phys.* **2018**, *18* (6), 633–641.
- [36] Hossain, M. K.; Arnab, A. A.; Toki, G. F. I.; Bhattarai, S.; Tawfeek, A. M.; Bencherif, H.; Dwivedi, D. K.; Madan, J.; Pandey, R. High-Efficiency Lead-Free La₂NiMnO₆-Based Double Perovskite Solar Cell by Incorporating Charge Transport Layers Composed of WS₂, ZnO, and Cu₂FeSnS₄. *Energy & Fuels* **2023**, *37* (24), 19898–19914.
- [37] Hossain, M. K.; Uddin, M. S.; Toki, G. F. I.; Mohammed, M. K. A.; Pandey, R.; Madan, J.; Rahman, M. F.; Islam, M. R.; Bhattarai, S.; Bencherif, H.; Samajdar, D. P.; Amami, M.; Dwivedi, D. K. Achieving above 24% Efficiency with Non-Toxic CsSnI₃ Perovskite Solar Cells

by Harnessing the Potential of the Absorber and Charge Transport Layers. *RSC Adv.* **2023**, *13* (34), 23514–23537.

[38] Uddin, M. S.; Hossain, M. K.; Uddin, M. B.; Toki, G. F. I.; Ouladsmame, M.; Rubel, M. H. K.; Tishkevich, D. I.; Sasikumar, P.; Haldhar, R.; Pandey, R. An In-Depth Investigation of the Combined Optoelectronic and Photovoltaic Properties of Lead-Free Cs₂AgBiBr₆ Double Perovskite Solar Cells Using DFT and SCAPS-1D Frameworks. *Adv. Electron. Mater.* **2024**.

[39] Adewoyin, A. D.; Olopade, M. A.; Chendo, M. Enhancement of the Conversion Efficiency of Cu₂ZnSnS₄ Thin Film Solar Cell through the Optimization of Some Device Parameters. *Optik (Stuttg.)* **2017**, *133*, 122–131.

[40] Frisk, C.; Ericson, T.; Li, S.-Y.; Szaniawski, P.; Olsson, J.; Platzer-Björkman, C. Combining Strong Interface Recombination with Bandgap Narrowing and Short Diffusion Length in Cu₂ZnSnS₄ Device Modeling. *Sol. Energy Mater. Sol. Cells* **2016**, *144*, 364–370.

[41] Ferdaous, M. T. T.; Shahahmadi, S. A. A.; Chelvanathan, P.; Akhtaruzzaman, M.; Alharbi, F. H. H.; Sopian, K.; Tiong, S. K. K.; Amin, N. Elucidating the Role of Interfacial MoS₂ Layer in Cu₂ZnSnS₄ Thin Film Solar Cells by Numerical Analysis. *Sol. Energy* **2019**, *178* (November 2018), 162–172.

[42] Dakua, P. K.; Panda, D. K. Improving the Efficiency of ZnO/WS₂/CZTS₁ Solar Cells Using CZTS₂ as BSF Layer by SCAPS-1D Numerical Simulation. *Phys. Scr.* **2023**, *98* (8), 085402.

[43] Chaves, M.; Ramos, R.; Martins, E.; Rangel, E. C.; Cruz, N. C. da; Durrant, S. F. Bortoleto, J. R. R. Al-Doping and Properties of AZO Thin Films Grown at Room Temperature: Sputtering Pressure Effect. *Mater. Res.* **2019**, *22* (2).

[44] Li, W.; Li, W.; Feng, Y.; Yang, C. Numerical Analysis of the Back Interface for High Efficiency Wide Band Gap Chalcopyrite Solar Cells. *Sol. Energy* **2019**, *180*, 207–215.

[45] Mansouri, E.; Abderrezek, M.; Benzetta, A. E. Thin-Film CZTSSe Solar Cells Efficiency Improvement through BSF SnS Layer and Concentrator Applications. *Energy Sources, Part A Recover. Util. Environ. Eff.* **2024**, *46* (1), 2024–2039.

[46] Hosen, A.; Ahmed, S. R. Al. Performance Analysis of SnS Solar Cell with a Hole Transport Layer Based on Experimentally Extracted Device Parameters. *J. Alloys Compd.* **2022**, *909*, 164823.

[47] Burgelman, M.; Nollet, P.; Degraeve, S. Modelling Polycrystalline Semiconductor Solar Cells. *Thin Solid Films* **2000**, *361–362*, 527–532.

[48] Wu, C.; Zhang, L.; Ding, H.; Ju, H.; Jin, X.; Wang, X.; Zhu, C.; Chen, T. Direct Solution Deposition of Device Quality Sb₂S₃-XSex Films for High Efficiency Solar Cells. *Sol. Energy Mater. Sol. Cells* **2018**, *183*, 52–58.

[49] Hosen, A.; Mian, M. S.; Ahmed, S. R. Al. Simulating the Performance of a Highly Efficient CuBi₂O₄-Based Thin-Film Solar Cell. *SN Appl. Sci.* **2021**, *3* (5), 544.

- [50] Hosen, A.; Rahman, S.; Brella, M.; Ahmed, S. R. Al. Impact of Hole Transport Layers in Inorganic Lead-Free B- γ -CsSnI₃ Perovskite Solar Cells: A Numerical Analysis. In *ECP 2022*; MDPI: Basel Switzerland, 2022; p 41.
- [51] Xiao, Y.; Wang, H.; Kuang, H. Numerical Simulation and Performance Optimization of Sb₂S₃ Solar Cell with a Hole Transport Layer. *Opt. Mater. (Amst)*. **2020**, *108*, 110414.
- [52] Bencherif, H. Towards a High Efficient Cd-Free Double CZTS Layers Kesterite Solar Cell Using an Optimized Interface Band Alignment. *Sol. Energy* **2022**, *238*, 114–125.
- [53] Bencherif, H.; Dehimi, L.; Mahsar, N.; Kouriche, E.; Pezzimenti, F. Modeling and Optimization of CZTS Kesterite Solar Cells Using TiO₂ as Efficient Electron Transport Layer. *Mater. Sci. Eng. B* **2022**, *276*, 115574.
- [54] Khaouani, M.; Bencherif, H.; Kourdi, Z. An Improved Perovskite Solar Cell Employing In_xGa_{1-x}As as an Efficient Hole Transport Layer. *J. Comput. Electron.* **2022**.
- [55] Kherrat, F.; Dehimi, L.; Bencherif, H.; Moon, M. M. A.; Hossain, M. K.; Sonmez, N. A.; Ataser, T.; Messai, Z.; Özçelik, S. Performance Enhancement of Eco-Friendly Cs₃Sb₂I₉-Based Perovskite Solar Cell Employing Nb₂O₅ and CuI as Efficient Charge Transport Layers. *Micro and Nanostructures* **2023**, *183* (September).
- [56] Bencherif, H.; Meddour, F.; Elshorbagy, M. H.; Khalid Hossain, M.; Cuadrado, A.; Abdi, M. A.; Bendib, T.; Kouda, S.; Alda, J. Performance Enhancement of (FAPbI₃)_{1-x}(MAPbBr₃)_x Perovskite Solar Cell with an Optimized Design. *Micro and Nanostructures* **2022**, *171*, 207403.
- [57] Sun, K.; Liu, F.; Yan, C.; Zhou, F.; Huang, J.; Shen, Y.; Liu, R.; Hao, X. Influence of Sodium Incorporation on Kesterite Cu₂ZnSnS₄ Solar Cells Fabricated on Stainless Steel Substrates. *Sol. Energy Mater. Sol. Cells* **2016**, *157*, 565–571.
- [58] Ericson, T.; Larsson, F.; Törndahl, T.; Frisk, C.; Larsen, J.; Kosyak, V.; Hägglund, C.; Li, S.; Platzer-Björkman, C. Zinc-Tin-Oxide Buffer Layer and Low Temperature Post Annealing Resulting in a 9.0% Efficient Cd-Free Cu₂ZnSnS₄ Solar Cell. *Sol. RRL* **2017**, *1*(5).
- (59) Erkan, M. E.; Chawla, V.; Scarpulla, M. A. Reduced Defect Density at the CZTSSe/CdS Interface by Atomic Layer Deposition of Al₂O₃. *J. Appl. Phys.* **2016**, *119* (19).
- [60] Messaoud, K. Ben; Buffière, M.; Brammertz, G.; Lenaers, N.; Boyen, H.-G.; Sahayaraj, S.; Meuris, M.; Amlouk, M.; Poortmans, J. Synthesis and Characterization of (Cd,Zn)S Buffer Layer for Cu₂ZnSnSe₄ Solar Cells. *J. Phys. D. Appl. Phys.* **2017**, *50* (28), 285501.

Chapter 5:

Structural and Electrical Features: A Comparative Parameter Extraction Study of Al/p-CZTS Thin Film Schottky Diodes.

5.1. Introduction

Metal–semiconductor junctions play a pivotal role in the operation of various electronic devices, including field-effect transistors, light detectors, and solar cells, due to their significant influence on device functionality. Consequently, they are extensively employed as rectifying contacts within the semiconductor industry. Achieving superior performance in these devices necessitates the fabrication of high-quality Schottky contacts. Beyond their practical applications, Schottky diode structures hold immense importance in both electronic and photovoltaic realms. They provide a platform for investigating crucial metal–semiconductor parameters such as barrier formation, transport conduction mechanisms, and phenomena elucidated through the analysis of current–voltage characteristics [1].

Given the paramount importance of photovoltaic applications, Kesterite copper zinc tin sulfide ($\text{Cu}_2\text{ZnSnS}_4$, CZTS) thin films emerge as a compelling alternative to existing technologies, boasting outstanding photovoltaic properties and promising performance metrics. Notably, CZTS thin films exhibit an absorption coefficient surpassing 10^4 cm^{-1} and a direct energy band gap ranging from 1.4 to 1.5 eV [2–5].

In this realm, pivotal steps include delineating the physical parameters of the resulting Schottky barrier diode (SBD) and establishing Schottky connections to CZTS thin films. Among these parameters, the ideality factor, series resistance, and Schottky-barrier height (SBH) stand out as fundamental factors crucial for accurately modeling and simulating the characteristics of these devices. Such categorization significantly aids in understanding their behavior across diverse operating conditions.

However, the identification of these critical quantities poses unresolved technical challenges due to inherent discrepancies from measured data, necessitating continuous examination. Recent times have seen the emergence of various approaches aimed at estimating the parameters of SBDs, broadly classified into two groups: analytical methods and numerical methods [6–8].

These advancements mark ongoing efforts to refine the characterization and performance prediction of Schottky barrier diodes in CZTS thin film applications.

Numerical approaches, leveraging curve-fitting algorithms to ascertain the optimal alignment between actual properties and theoretical models, exhibit higher reliability and reduced error susceptibility compared to analytical methods [9–12]. The accuracy of fitting algorithms is intricately tied to several factors, including the algorithm type, the objective function earmarked for minimization, and the initial parameter values pre-configured before algorithm execution. The meticulous adjustment of these elements significantly influences the precision of the fitting algorithms.

In this study, we provide a comprehensive outline of the fabrication process for the Schottky junction Al/p-CZTS/ Mo and the synthesis of Cu₂ZnSnS₄ thin films using the sol–gel method. Structural characterization of the (CZTS)/ Mo thin film was conducted using X-ray diffraction. To glean insights into the device’s performance, current–voltage characteristics (I–V) were analyzed, extracting crucial parameters such as ideality factor, current of saturation, and series resistance, while also considering the impact of parallel conductance. To accurately determine the SBD model parameters from experimental I–V data, we explore two methods: the Newton–Raphson Method (NRM) and genetic algorithm (GA). Our aim is to assess the precision and computational efficiency of these methods, providing valuable insights into their applicability for parameter extraction in SBD modeling. Our work progresses as follows: we begin with a detailed exposition of the experimental fabrication setup. Next, we investigate both the structural and electrical properties. Moving forward, we introduce the Modeling framework of SBD. Finally, we present our findings and engage in discussion, drawing to a close with a comprehensive conclusion and relevant remarks.

5.2. Experimental setup

Schottky diodes comprising Al/p-CZTS/Mo were fabricated through a series of steps. Initially, Cu, Zn, and Sn metallic layers were deposited sequentially onto a Mo-coated soda lime glass (SLG) substrate using a spin-coating process. The precursor solution for this deposition was prepared by dissolving copper (II) chloride (0.6 M), zinc (II) chloride (0.42 M), tin (II) chloride dehydrate (0.39 M), and thiourea (2.4 M) in de-ionized water, supplemented with 70% vol of ethanol, to form a sol–gel solution. The sol–gel solution was gently stirred at room temperature for thirty minutes before undergoing the spin-coating process. Spin-coating was carried out for 30 s at a speed of 3000 rpm. Subsequently, circular electrodes of aluminum (Al) with a 2 mm diameter were deposited onto the CZTS thin film, which had been previously deposited on

molybdenum (Mo)- coated substrates. The electrodes underwent annealing for one hour at 500 °C within an argon environment to finalize the creation of Schottky barrier type diodes. Further details on the diode manufacturing procedure can be found in [13]. Surface morphologies were meticulously examined using scanning electron microscopy (SEM), while the crystallographic structures of the CZTS thin films were thoroughly analyzed via X-ray diffraction (XRD).

The current–voltage (I–V) characteristics of the structure were measured at room temperature utilizing a Keithley 410 programmable ammeter and voltmeter, along with a Keithley LCZ3000 meter. Figure 5.1 illustrates a schematic cross-sectional image of the Schottky diodes under investigation in this study.

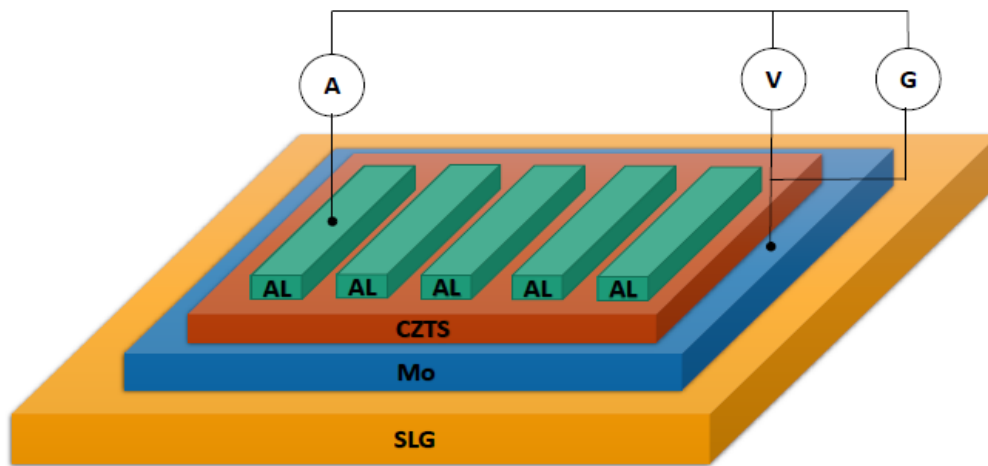


Figure 5.1: Al/p-CZTS/Mo Schottky barrier diode schematic cross section.

It is noted, that band alignment at the metal/CZTS interface is pivotal for CZTS solar cell efficacy. Achieving optimal alignment enables efficient charge extraction and transport. Challenges, such as interfacial defects and Fermi level pinning, complicate this alignment. Strategies like surface passivation and interface layer deposition offer avenues for improvement, enhancing overall device performance.

5.3. Structural and electrical properties

5.3.1. Analysis of CZTS thin film surface morphology

Figure 5.2 presents scanning electron micrographs (SEM) depicting the precursor-deposited Mo-coated SLG. The images were captured at magnifications of 46.64 KX and 23 KX. Notably, the

SEM images reveal that the entire surface morphology of the precursor films exhibits uniform coating with spherical granules.

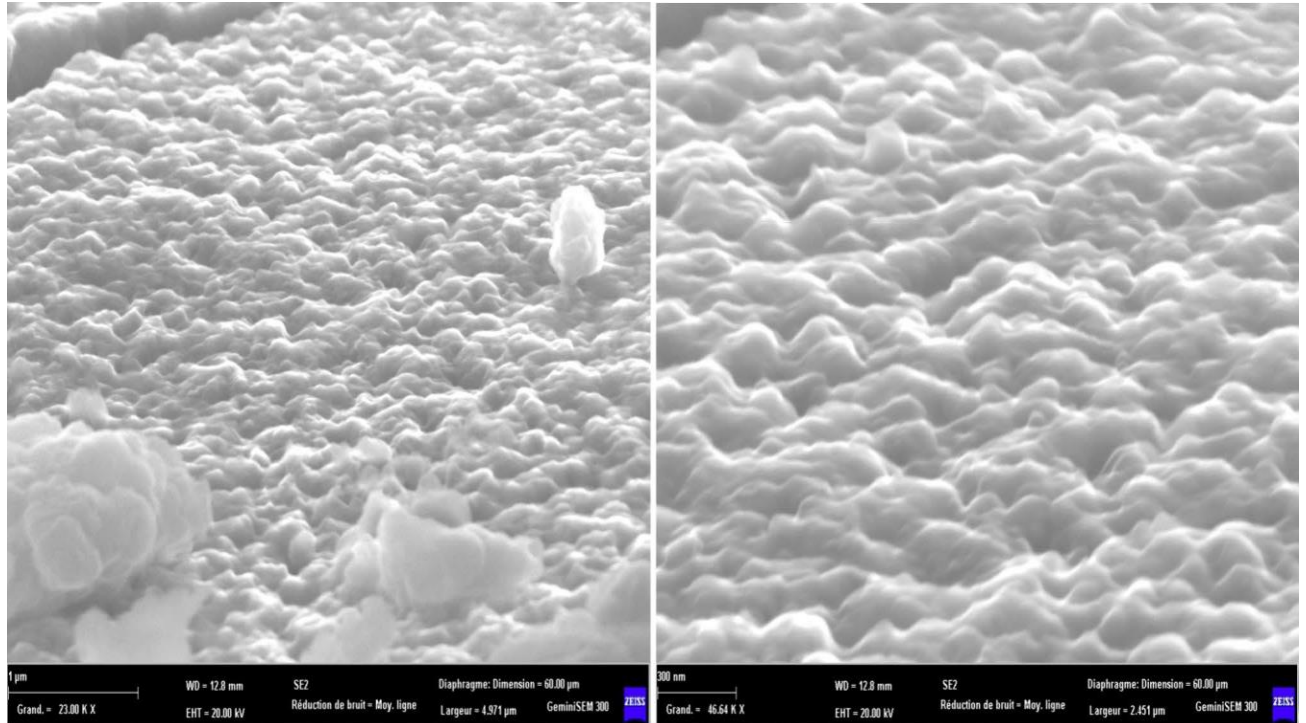


Figure 5.2: SEM surface images of precursor CZTS film.

5.3.2. Elemental analysis of CZTS thin film

The elemental composition of the stacked precursor was analyzed using the Energy-Dispersive X-ray (EDX) method to ascertain the distribution of elements present. Figure 5.3 showcases the EDX spectrum of the CZTS film. Analysis reveals the presence of copper, zinc, tin, and sulfur elements in the prepared sample. Table 5.1 provides a comparison of the original weight, final weight, and atomic percentage. Notably, the beginning and end weights and atomic percentages are nearly identical, affirming the phase development of the $\text{Cu}_2\text{ZnSnS}_4$ film.

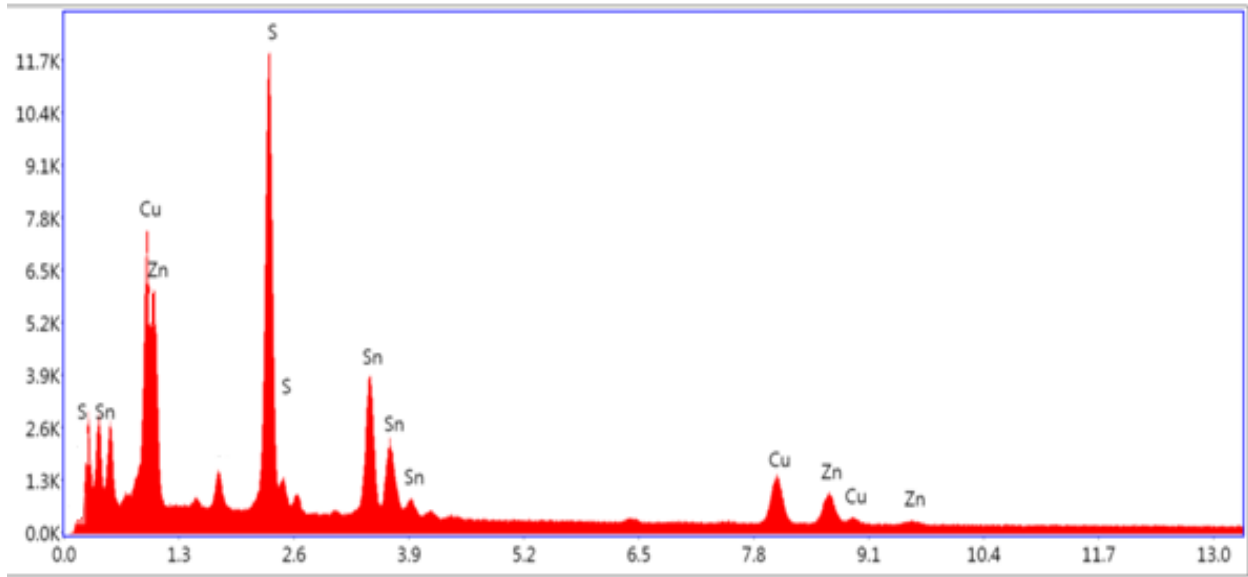


Figure 5.3: Energy-Dispersive X-ray Spectra of precursor CZTS film.

Table 5.1: Weight and atomic composition of CZTS thin film

Element compositions	Initial measurements		Final measurements	
	wt. %	at. %	wt. %	at. %
S K	29,76	51,36	29,06	51,26
SnL	29,93	13,97	33,83	16,10
CuK	22,48	19,59	20,35	18,12
ZnK	17,83	15,08	16,76	14,52

5.3.3. Current–voltage (I–V) characteristics

As depicted in Figure 5.4, experimental forward and reverse bias current–voltage (I–V) characteristics of the Al/p- CZTS/Mo junction was conducted at room temperature. Notably, the junction exhibits a Schottky barrier at the Al/p-CZTS/Mo interface, evident from its nonlinear, asymmetric, and rectifying behavior. At a reverse bias voltage of 0.9 V, a modest leakage current of 1×10^{-6} A is observed. Additionally, the rectification ratio, calculated as $I(+2V)/I(-2V) = 8$, underscores the junction’s rectifying property. Interestingly, the absence of saturation in the reverse voltage characteristics suggests the occurrence of tunneling or defect-assisted generation mechanisms.

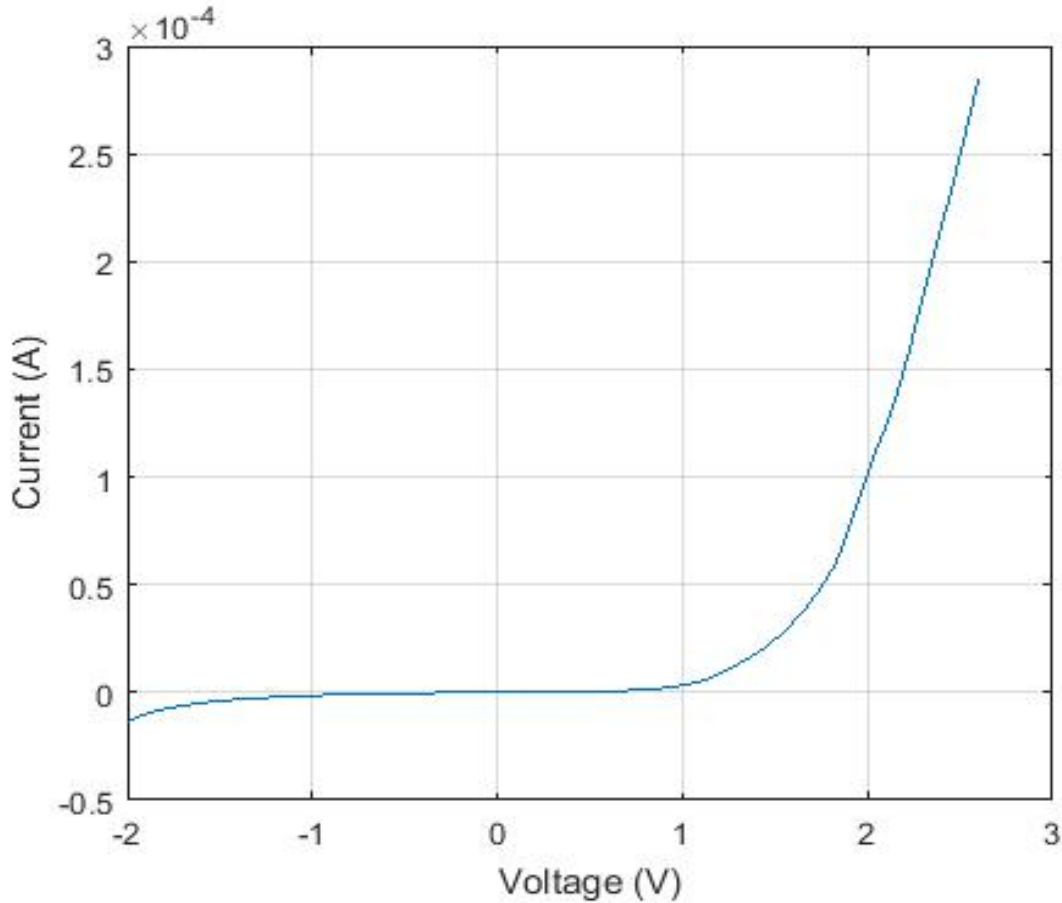


Figure 5.4 : Room-temperature current–voltage characteristics in forward and reverse bias of the fabricated Al/p-CZTS/Mo Schottky junctions

5.4. Modeling framework

Figure 5.5 illustrates the detailed framework for parameter extraction using optimization algorithms in our proposed approach.

The extraction system relies on inputs from the optimizer section, which incorporates the Schottky barrier diode model equation, measured experimental data, and optimization techniques. Crucial parameter values for characterization are obtained through optimization algorithms aimed at minimizing the disparity between measured data and the model's response. Subsequently the model generates data using these extracted parameters, refining and calibrating its predictive accuracy through an iterative process.

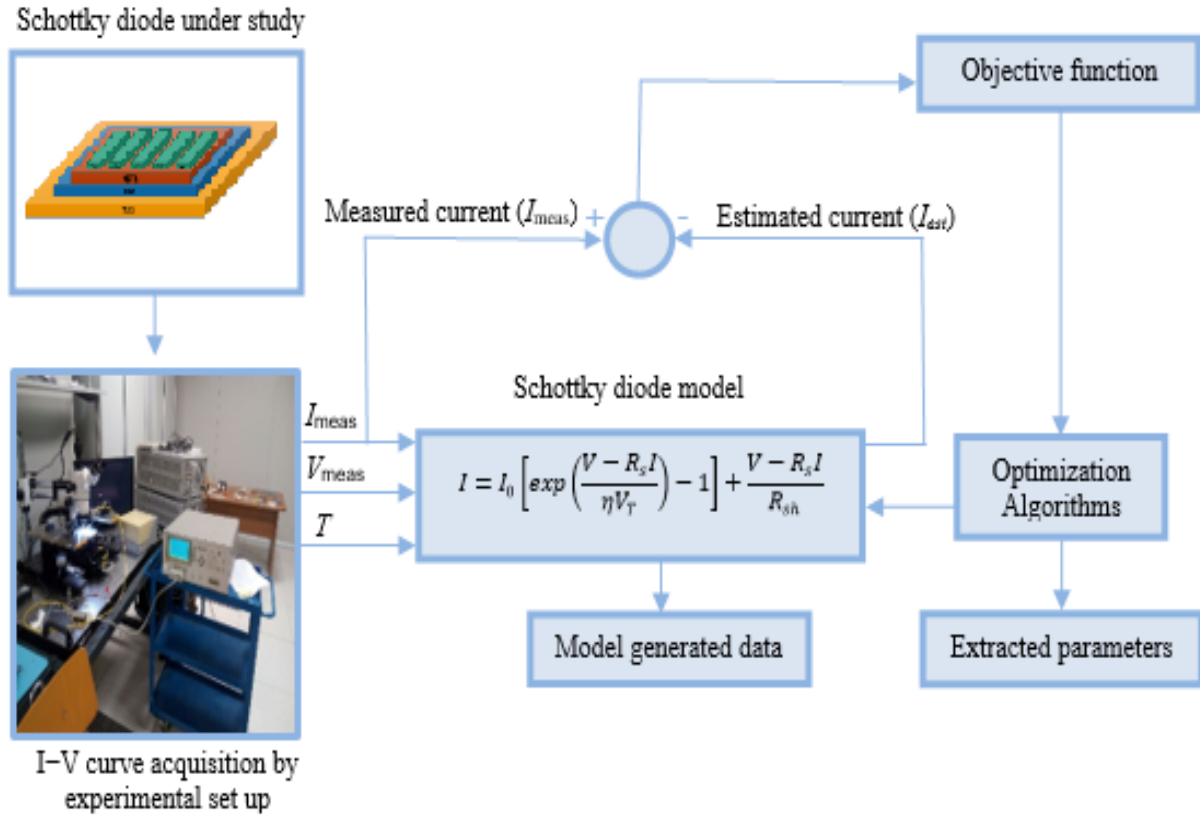


Figure 5.5: Schottky barrier diode parameters extraction architecture.

5.4.1. Mathematical model of SBD

The forward bias current-voltage I-V characteristics of SBDs due to thermionic emission (TE) model, which includes the resistive voltage drop, can be expressed as [14,15]:

$$I = I_s \left[\exp\left(\frac{q(V - R_s I)}{\eta k T}\right) - 1 \right], \quad (5.1)$$

where: η is the ideality factor, V is the diode bias voltage, q is the electronic charge, k is the Boltzmann constant, T is the absolute temperature, R_s is the series resistance

where I denotes the current, V represents the applied diode bias voltage, and other symbols (I_s , q , R_s , η , k , T) stand for the saturation current, electronic charge, series resistance, ideality factor, Boltzmann constant, and absolute temperature, respectively.

The formula for calculating saturation current is:

$$I_s = AA^*T^2 e^{\left(-\frac{q\phi_B}{kT}\right)}, \quad (5.2)$$

in this context, ϕ_B is the barrier potential, A is the diode's surface area, A^* denotes the Richardson constant. Its value is theoretically in the order of $A^* = 63.6 \text{ Acm}^{-2}\text{K}^{-2}$ for P-type CZTS [16].

In diodes that deviate from ideal behavior, the observed characteristics typically display more complexity due to the influence of shunt resistance R_{sh} . This resistance primarily affects the current-voltage (I-V) characteristics at lower forward voltages and is especially significant in altering the reverse characteristics in diodes with a high Schottky barrier height (SBH).

The SBD model can be expressed as Equation (5.3) to incorporate the effects of side-wall leakage and other leakage routes. This equation describes the correlation between the terminal current, terminal voltage, and the extraction parameters. Hence, it is evident that this model requires the identification of four unknown parameters (I_s , η , R_s , R_{sh}) [17,18].

The equation can be expressed as

$$I = I_s \left[\exp\left(\frac{q(V-R_s I)}{\eta kT}\right) - 1 \right] + \frac{V-R_s I}{R_{sh}}. \quad (5.3)$$

5.4.2. Objective function of parameter extraction problem

To apply optimisation approaches for solving the parameter identification problem of the SBD model, it is necessary to first establish the objective function. The purpose of this function is to minimise the discrepancy between the measured and estimated current values. The error function $F(V_e, I_e, X)$ is determined for each pair of measured and calculated current data points using Equation (5.4). In this equation, V_e and I_e represent the voltage and current of data points in experimental I-V curves, while the solution vector X represents the vector of unknown parameters that need to be retrieved [19].

$$F(V_e, I_e, X) = I_e - \left[I_s \left(\exp\left(\frac{V_e - R_s I_e}{\eta V_T}\right) - 1 \right) + \frac{V_e - R_s I_e}{R_{sh}} \right], \quad (5.4)$$

$$X = [I_s, \eta, R_s, R_{sh}]. \quad (5.5)$$

Based on the simplified error function, the root mean square error (*RMSE*) is defined as the objective function, formulated by Equation (5.6), where N is the total number of measurements in the dataset

$$RMSE = \sqrt{\frac{1}{N} \sum_{i=1}^N F(V_e^i, I_e^i, X)^2} \quad (5.6)$$

Finding the SBD parameter values that minimize the RMSE value as much as feasible is the primary goal of this optimization.

5.4.3. Determining the initial parameters values

Selecting the optimal initial parameters could potentially have a significant impact on accelerating the convergence process. Contrary, wrong choice of the initial parameters can affect the optimization algorithm and increase the iterations number. In this study, the initial parameters $(I_s^0, \eta^0, R_s^0, R_{sh}^0)$ will be determined using the method suggested by Lee et al. [20].

Through this procedure, an auxiliary function $F_L(I)$ is established utilizing the measured values of the current–voltage (I–V) characteristics and an arbitrary voltage V_a .

$$F_L(I) = V(I) - V_a \ln I \quad (5.7)$$

From Equation (1) we can write:

$$V(I) = R_s^0 I + \frac{\eta^0 kT}{q} \ln I + \eta^0 \frac{kT}{q} \ln I_s^0. \quad (5.8)$$

Each $F_L(I)$ function is approximated by

$$F_L(I) = aI + b \ln I + c. \quad (5.9)$$

The plot of V vs I is fitted by Equation (5.9) and

$$R_s^0 = a \quad (5.10)$$

$$\eta^0 = \frac{bq}{kT} \quad (5.11)$$

$$I_s^0 = \exp \frac{cq}{\eta^0 kT}. \quad (5.12)$$

The initial estimation of R_{sh}^0 , can be calculated by graphical method [21]. In the small voltage values, the $I = f(V)$ curve is linear:

$$I = \frac{V}{R_{sh}^0 + R_s^0}. \quad (5.13)$$

This equation can be written:

$$I = aV \quad (5.14)$$

where

$$R_{sh}^0 = \left(\frac{1}{a} - R_s^0 \right). \quad (5.15)$$

The shunt resistance R_{sh}^0 can be determined by adjusting the $I=f(V)$ curve by the curve fitting.

5.5. Results and discussion

Over the years, several methods have been used to solve the problem of SBD parameters extraction. In this work, the estimation problem is formulated as a nonlinear optimization problem. The Newton–Raphson Method (NRM) and GA algorithms are implemented to obtain parameters of SBD model.

5.5.1. Newton–Raphson method

The Newton-Raphson method (*NRM*) is an efficient method for solving nonlinear equations relying on the principle of linear approximation.

The process begins with a randomly selected starting estimate and thereafter achieves faster convergence for the majority of the function, regardless of the beginning estimate [11]. The Newton-Raphson method (*NRM*) iteratively approaches the root $f(x)$ using the first-order polynomial of the Taylor Series. This polynomial is represented as:

$$x_{n+1} = x_n - \frac{f(x_n)}{f'(x_n)} \quad (5.16)$$

In Equation (5.16), n represents the n^{th} iteration and $f'(x)$ denotes the derivative of $f(x)$. Applied to solve Equation (5.3), the method allows for the calculation of the output current (I) for a specific voltage by iterating:

$$I_{n+1} = I_n - \frac{f(I_n)}{f'(I_n)} \quad (5.17)$$

Where

$$f(I_n) = I_n - I_0 \left[\exp \left(\frac{V - R_s I_n}{\eta V_T} \right) - 1 \right] - \frac{V - R_s I_n}{R_{sh}} \quad (5.18)$$

and

$$f'(I_n) = 1 + \frac{I_0 R_s}{\eta V_T} \left[\exp\left(\frac{V - R_s I_n}{\eta V_T}\right) - 1 \right] - \frac{V - R_s I_n}{R_{sh}} \quad (5.19)$$

The iterative update of the value of I continues until $f(I)$ converges to a predetermined error threshold ε when estimating the value of II using NRM. This process commences with an initial value of I .

Figure 5.6 shows the primary steps of the computational technique for determining the SBD parameters, which is based on Newton Raphson's methodology.

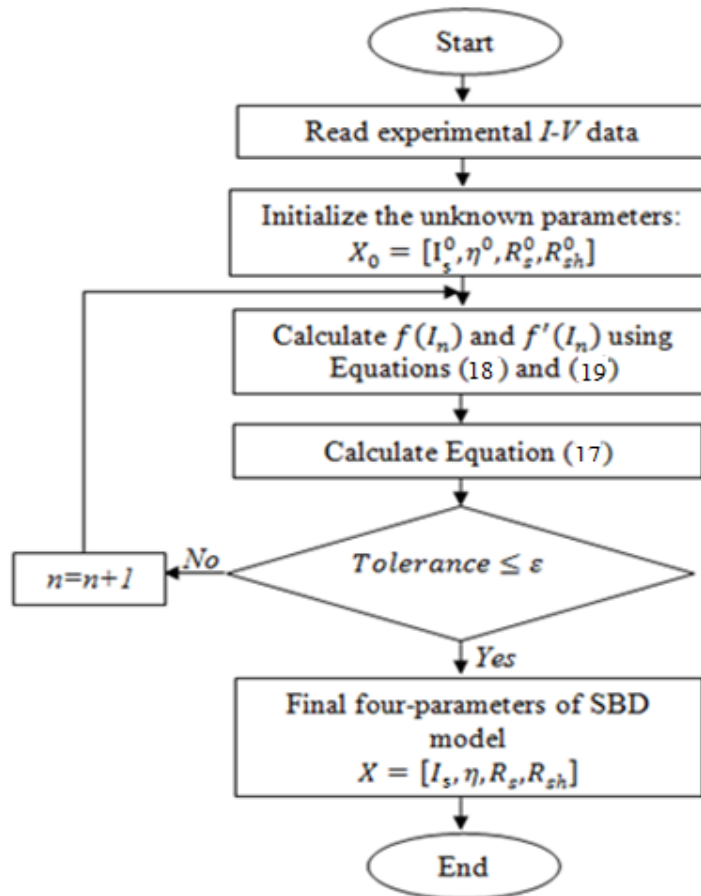


Figure 5.6: Flowchart of proposed algorithm for *SBD* Parameters estimation.

5.5.2. Curve fitting models of solar cell characteristics

We propose a simple fitting technique that utilizes a single dark current–voltage (I – V) curve to forecast the characteristics of a solar cell. This method simplifies parameter extraction as the adjustment process is unidimensional. For example, once parameters like η , R_s , I_s , and R_{sh} are

extracted; only a few lines of code are required within a MATLAB environment to complete the process efficiently.

5.5.2.1. Determination of the initials value of η , R_s and I_s

This technique includes the presentation of the standard function $I = f(V)$ as $V = f(I)$ which provides the calculation of the parameters of the solar cell.

To evaluate the ideality factor, the series resistance and the saturation current of the diode, we use I instead of V as an independent variable in simplified Equation (5.20) (valid in the direct polarization region $0.2 \text{ V} - 1 \text{ V}$):

$$I = I_s \left[\exp\left(\frac{V - R_s I}{\eta V_T}\right) - 1 \right] \quad (5.20)$$

we obtain:

$$V = \eta V_T \ln I + R_s I - \eta V_T \ln I_s \quad (5.21)$$

Eq. (5.21) can be presented in the form:

$$V = a \ln I + b I + c$$

$$\text{where } \begin{cases} a = \eta V_T \\ b = R_s \\ c = -\eta V_T \ln I_s \end{cases}$$

$$\text{i.e. } \begin{cases} \eta = \frac{V_T}{a} \\ R_s = b \\ I_s = \exp\left(\frac{-c}{\eta V_T}\right) \end{cases}$$

Hence, the constants a , b , and c remain fixed for a solar cell or PV module at a given temperature. Employing non-linear least squares fit allows determination of these constants. Subsequently, parameters such as η , R_s , and I_s are deduced from a set of values for a , b , and c .

By utilizing Equation (5.21), this process results in a highly accurate alignment with the observed voltage-current ($V-I$) characteristic. This alignment is visually demonstrated through a fitted curve juxtaposed with an experimental solar cell $V-I$ characteristic, as depicted in Figure 7a.

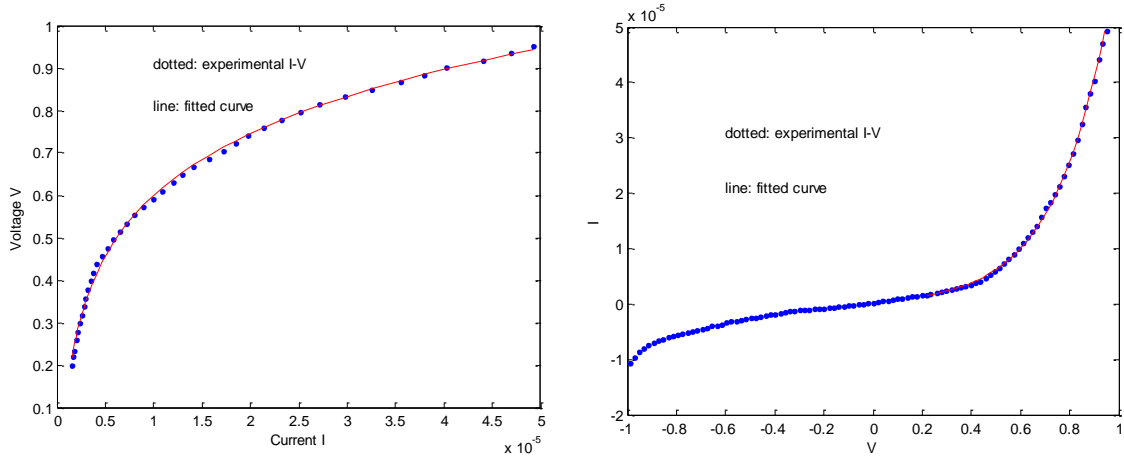


Figure 5.7: (a) Characteristic $V = f(I)$, equation (5.22), (b) experimental solar cell $I-V$ characteristic and fitted curve in the direct polarization region 0.2 V – 1 V.

The obtained η , R_s , I_s are respectively : $\eta = 9,9467$, $R_s = 1.7554k\Omega$ and $I_s = 82,77nA$.

5.5.2.2. Determination of R_{sh}

For the determination of R_{sh} we take the linear region (-0.2 V – 0.2 V) of the curve $I = f(V)$ whose function is:

$$I = \frac{V}{R_{sh} + R_s} \quad (5.22)$$

Equation (5.22) can be presented in the form:

$$I = a \cdot V \quad \text{where} \quad a = \frac{1}{R_{sh} + R_s}$$

$$\text{i.e.} \quad R_{sh} = \left(\frac{1}{a} - R_s \right)$$

The shunt resistance R_{sh} can be determined by adjusting the $I = f(V)$ curve by the curve fitting.

Figure 7b illustrates this result and shows both an experimental solar cell $I-V$ characteristic and fitted curve.

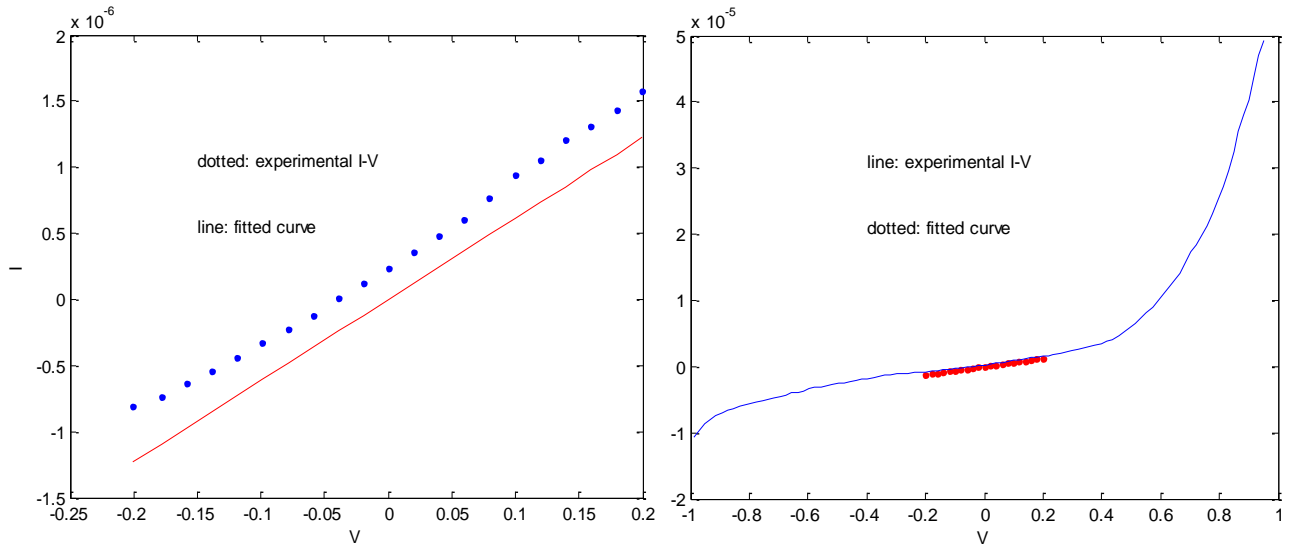


Figure 5.8: (a) $I = f(V)$, equation. (5.22),

(b) $I = f(V)$ of Figure 5.4.

Figures 5.8 a and b show both experimental solar cell $I-V$ characteristic and fitted curve in the linear region $-0.2 \text{ V} - 0.2 \text{ V}$ and the obtained $R_{sh} = 0,70857 \text{ M}\Omega$.

In order to check the obtained CZTS solar cell parameters values, we simulate the $I-V$ characteristic (Equation (5.3)) using the extracted parameters η , R_s , I_s and R_{sh} (Sect. 5.4.1) and compare it to the experimental one. We use Newton–Raphson’s method to solve Equation (5.1), V is chosen between -1 and 1 V by a linear discretization. Figure 5.9 presents the simulated $I-V$ characteristic using the extracted parameters η , R_s , I_s and R_{sh} , alongside the experimental $I-V$ characteristic. It turns out that, the modeled $I-V$ curve line up quite rigorously with the experimental one.

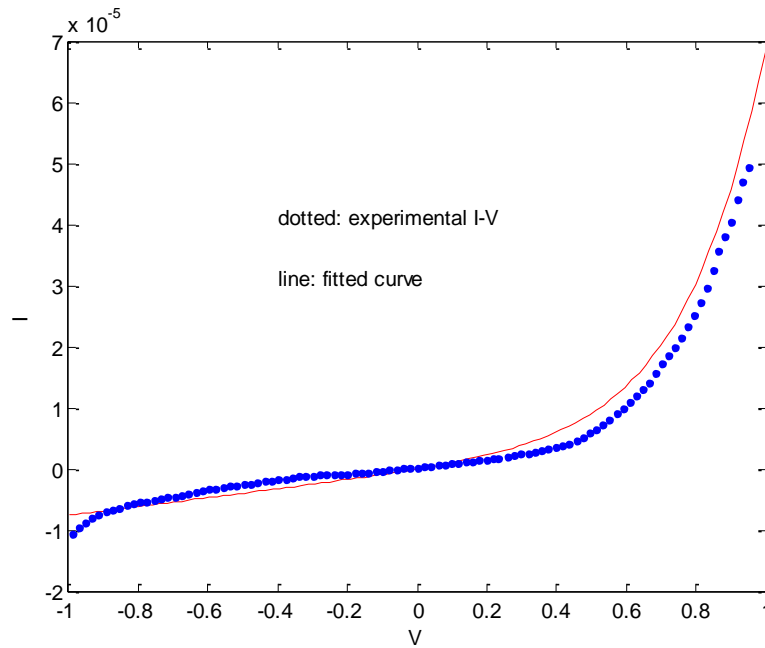


Figure 5.9: $I = f(V)$, equation 5.3

5.5.3. Genetic algorithm

The working principle of genetic algorithm depends mainly on the theory of biological evolution, where in each step the algorithm uses, from the current solutions, a random group of individuals often called “parents” [22–26]. In our case the solutions denote the vectors of I_s , R_s , R_{sh} , η . The production of children by parents is usually through introducing changes in some actual solutions (mutation) or by joining two existing solutions to obtain significant improvements (crossover).

The main idea revolves around the development of the primary population over successive generations to achieve the optimum solution. The main factors that contribute to the development process are the selection, reproduction and the mutation.

The GA-based approach is utilized as an alternative in this part to extract the key Schottky diode figures of merit in terms of reverse saturation current, series and shunt resistance, and ideality factor. In broad sense, the root mean square (RMSE) of the difference between the experimental

and the predicted currents, determined via the model of double-diode employing measured voltages (V_{mes}) at all points on the I–V curves, is described as objective function.

The objective function is utilized to fit the complete I–V curve, and the RMSE achieved is often depends on the quantity of points N , that must be appropriately selected.

The region of interest and calculation time must be given particular consideration. X denotes the four retrieved schottky diode parameters, which are as follows:

$$X = [\eta, I_s, R_s, R_{sh}].$$

The GA implementation process for extracting schottky diode parameters is described in full hereunder. The following phases are keys in the GA algorithm: initialization, selection, crossover, mutation, and replacement. To begin, a population of 100 individuals is chosen randomly to serve as initial solution space inside the specified search areas. The entire objective function is then analyzed in order to choose the finest people for being parents for the future generation based on tournament selection. Following that, these parents are randomly merged based on the crossover and mutation procedures to generate the offspring. The two operators enable for the diversity of future offspring containing the best solutions. In this study, scattered crossover and adaptive feasible mutation are used to improve efficiency. Afterwards, the existing population is substituted by the newly updated population. The algorithm repeats across the generations until the termination requirements are met, which is generally a satisfying objective function value, or until the highest number of generations designated is achieved.

The flowchart in Figure 5.10 summarizes the optimization process used to retrieve the four parameters.

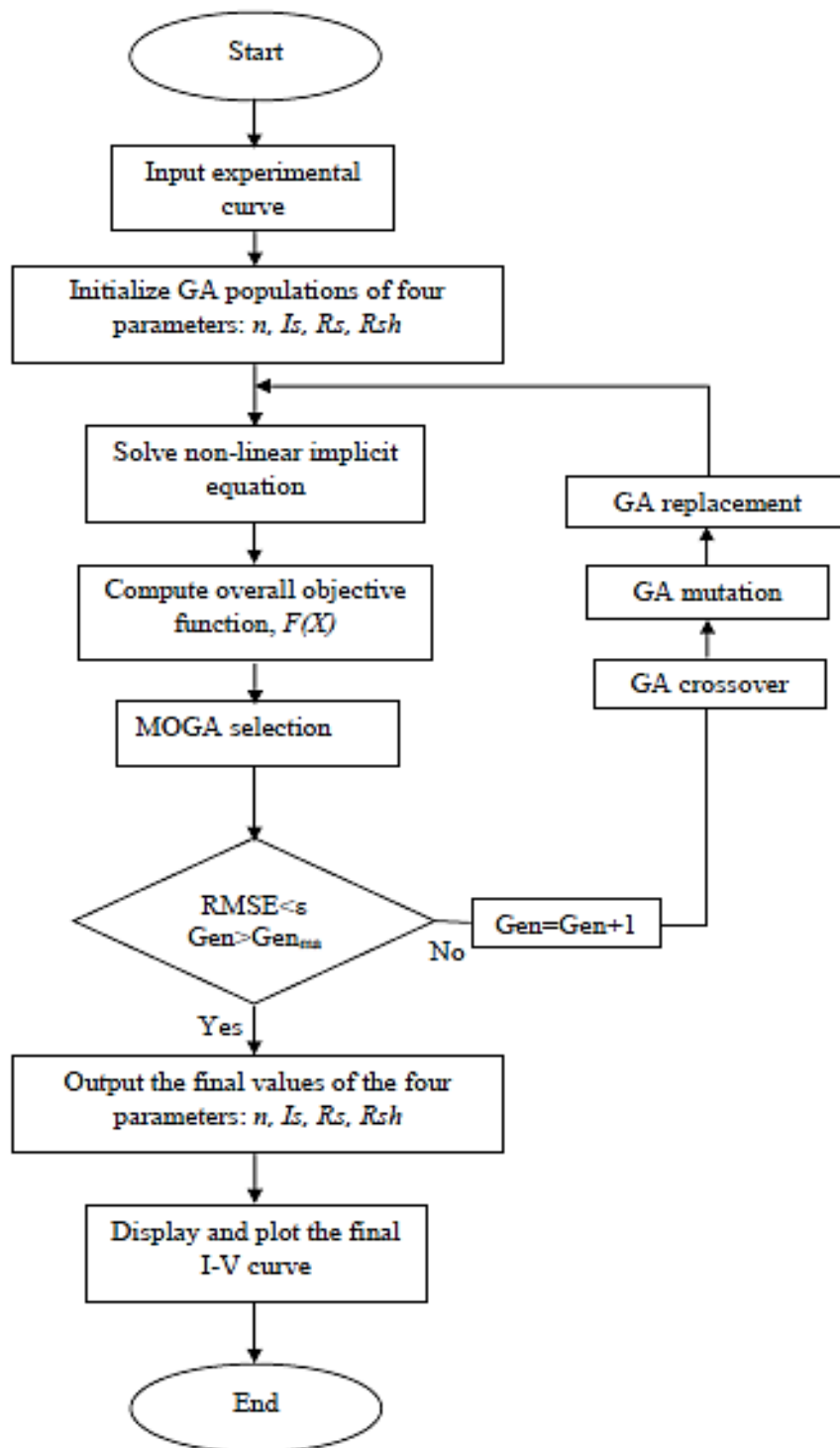


Figure 5.10: Flowchart of GA approach.

To summarize, the GA based extraction technique is focused on reducing the objective function, as described in Equation (5.6), in order to match the estimated and experimental currents at the same time.

Table 5.2 provides a summary of all setup parameters used in this investigation for the GA-based optimization [27, 28].

Table 5.2: Configuration parameters used for GA approach.

Number of variables	4
Population size	1000
Maximum number of generations	500
Selection	Tournament
Crossover	Scattered
Mutation	Adaptive Feasible Migration
Crossover fraction	0.8
Migration fraction	0.2

5.6. Comparison between Newton–Raphson method (NRM) and genetic algorithm (GA) method

The primary Schottky diode parameters (n , I_s , R_s , R_{sh}) have been extracted from the experimental I–V characteristics of the diode. Several techniques, including the genetic algorithm (GA) and the Newton–Raphson Method (NRM), were used to accomplish the extraction. Ultimately, a comparative analysis was conducted to assess those methodologies' accuracy. Table 5.3 summarizes the parameters extracted using the GA method with experimental data.

Table 5.3: Parameters extracted using the GA method with experimental data.

<i>Parameter</i>	<i>RMSE</i>	<i>I_s</i>	<i>R_s</i>	<i>R_{sh}</i>	<i>η</i>
<i>Value</i>	2.4684×10^{-06}	2.5213236512730 3×10^{-08} A	1810.31888212 277 Ω	337186.020887 277 Ω	8.61814964343 631

The starting values of SBD parameters are specified in Table 5.4 and are placed into the NRM and GA. The suggested approach was used to determine the initial parameters (I , η , R). Table 5.5 summarizes the parameters that were extracted using the three different approaches.

Table 5.4: Initial parameters value for the Newton–Raphson and GA.

R_s^0	R_{sh}^0	I_s^0	η^0
1,7554 k Ω	0,70501M Ω	82,077nA	9,9467

Figure 5.11 depicts the fitness value progression as function of generation of the population, besides this figure shows the I-V curve for both fitted and experimental results. It can be seen that a good coincidence is achieved.

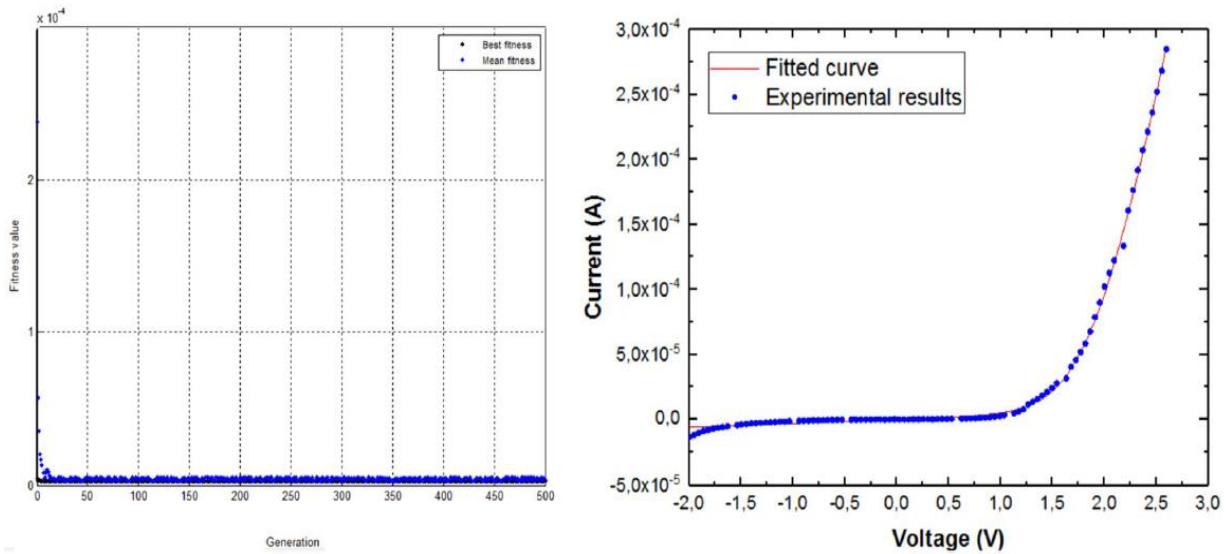


Figure 5.11: (a) Evolution of the objective function as function of the evolving generations, (b) Comparison of experimental and fitted I - V characteristics.

Figure 5.12 clearly illustrates that the current–voltage (I - V) characteristics generated by both the genetic algorithm (GA) and Newton–Raphson Method (NRM) approaches exhibit excellent agreement with experimental data across their entire range. This robust alignment underscores the suitability of both methods for accurately determining the parameters of the Schottky barrier diode (SBD) model.

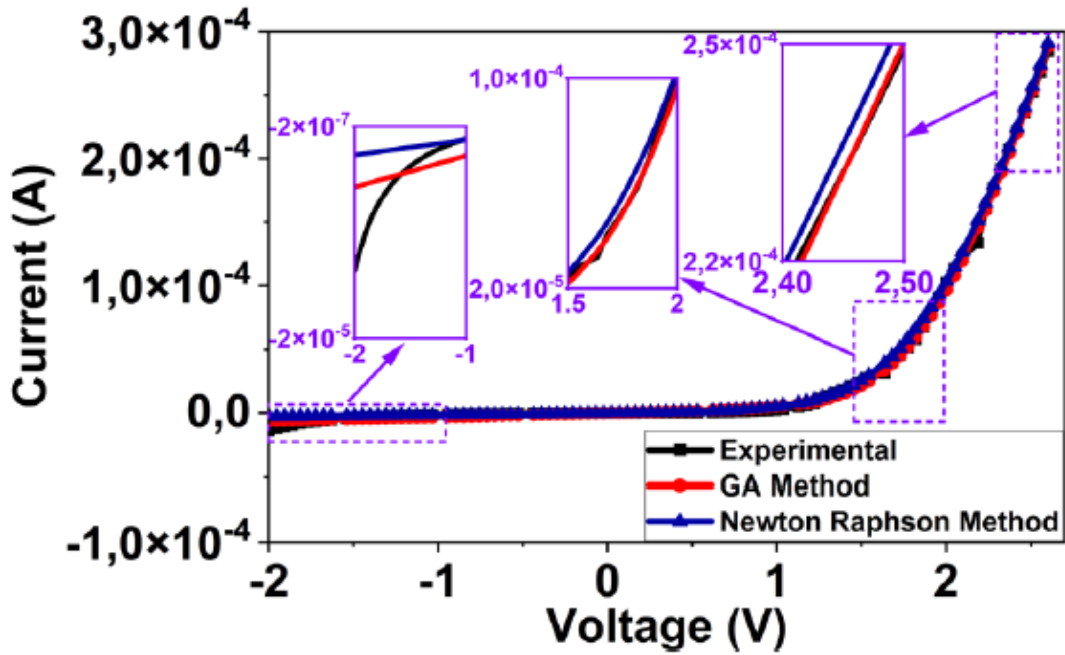


Figure 5.12: I-V characteristics comparisons between the experimental data and the predicted by *NRM* and *GA*.

Table 5.5 compares the *NRM* and *GA* techniques yields.

Table 5.5: Results of Schottky diode parameters obtained by Newton–Raphson and *GA* techniques.

Parameters	<i>NRM</i>	<i>GA</i>
I_s	1.4666×10^{-7} A	2.52×10^{-8} A
η	10,6592	8.6181
R_s	1,8613 K Ω	1.8103 K Ω
R_{sh}	$3.9111 \times 10^5 \Omega$	$3.3718 \times 10^5 \Omega$
RMSE	3.6355×10^{-6}	2.4684×10^{-6}

Table 5.6 shed light on the performance of the proposed extraction technique against other competitive techniques and summarize the limitation of each technique. Each optimization method mentioned—Newton–Raphson, Levenberg–Marquardt, Lambert-W function, and Genetic Algorithm—has distinct strengths and weaknesses that influence their suitability for different types of problems.

Table 5.6: Advantages and limitations of different competitive extraction methods [29].

Method	Advantages	Limitations
Newton–Raphson	Accurate when the optimization problem is high-dimensional and multi-model	Prolonged execution time
Levenberg–Marquardt	High degree of stability	Control precision and effectiveness cannot be guaranteed
Lambert-W function	High accuracy, strong robustness, and a fast convergence rate	Weak stability
Genetic algorithm	More efficient, and provide much faster convergence	Computationally expensive

Newton–Raphson excels in accuracy for complex, multidimensional optimization tasks but can be computationally intensive, resulting in prolonged execution times.

Levenberg–Marquardt offers high stability, making it reliable for many optimization scenarios, yet it lacks robust control over precision and effectiveness. The Lambert-W function is praised for its high accuracy, robustness, and rapid convergence rate, though it may struggle with stability in certain contexts. Genetic Algorithms are efficient in navigating complex search spaces and often converge faster than other methods but come at the cost of significant computational resources. Therefore, the choice among these methods should be guided by the specific requirements of the optimization problem, balancing considerations of accuracy, stability, convergence speed, and computational efficiency.

5.7. Conclusion

In overview, we employed the spin coating technique to deposit the CZTS thin film, bypassing the need for subsequent sulfurization. Rigorous structural analysis unequivocally verified the presence of the distinctive Kesterite CZTS phase. Noteworthy in our exploration, the SEM micrograph of the CZTS sample revealed a surface characterized by both density and compactness. Turning our focus to electronic properties, the I – V characteristic analysis of the Al/p-CZTS/Mo junction unveiled the establishment of a Schottky diode. Within the realm of electronic characterization, we delved into the extraction of critical parameters; ideality factor, saturation current, series, and shunt resistance, employing two distinct methods.

Impressively, the parameters derived from these disparate approaches exhibited a remarkable concordance, affirming the robustness and reliability of our findings.

References

- [1] S. Ahmadi, A. Hannachi, N. Khemiri, A. Cantarero, M. Kanzari, Structural and optical properties of sulfurized $\text{Cu}_2\text{ZnSnS}_4$ films grown by one step method using calcined powders for electrical properties study of Al/p- $\text{Cu}_2\text{ZnSnS}_4$ Schottky diode. *MRS Adv.* (2024).
- [2] S.T. Yussuf, K.C. Nwambaekwe, M.E.E.I. Ramoroka, Iwuoha, "Photovoltaic efficiencies of microwave and $\text{Cu}_2\text{ZnSnS}_4$ (CZTS) superstrate solar cells." *Mater. Today Sustain.* **21**, 100287 (2023).
- [3] Y. Zhang, J. Guo, J. Ao, A critical review on the rational composition engineering in kesterite photovoltaic devices: selfregulation and mutual synergy. *J. Mater. Chem. A* (2023).
- [4] H. Bencherif, Towards a high efficient Cd-free double CZTS layers kesterite solar cell using an optimized interface band alignment. *Sol. Energy* **238**, 114–125 (2022).
- [5] H. Bencherif, L. Dehimi, N. Mahsar, E. Kouriche, F. Pezzimenti, Modeling and optimization of CZTS kesterite solar cells using TiO_2 as efficient electron transport layer. *Mater. Sci. Eng. B* **276**, 115574 (2022).
- [6] R. Rai, K.G. Dhal, Recent developments in equilibrium optimizer algorithm: its variants and applications. *Arch. Computat. Methods Eng.* (2023).
- [7] R. Ndegwa, J. Simiyu, E. Ayieta, N. Odero, A fast and accurate analytical method for parameter determination of a photovoltaic system based on manufacturer's data. *J. Renew. Energy* (2020).
- [8] H. Doğan, S. Kockanat, Next-generation application-based artificial intelligence in modeling and estimation for Ni/n-GaAs/ In schottky barrier diode. *Physica status solidi(a)* (2023).
- [9] E. Garoudja, W. Filali, S. Oussalah, N. Sengouga, M. Henini, Comparative study of various methods for extraction of multiquantum wells schottky diode parameters. *J. Semicond.* **41(10)**, 102401 (2020).
- [10] J. Liang, K. Qiao, M. Yuan, K. Yu, B. Qu, S. Ge, G. Chen, Evolutionary multi-task optimization for parameters extraction of photovoltaic models. *Energy Convers. Manage.* **207**, 112509 (2020).
- [11] A. Niccolai, A. Dolara, E. Ogliari, Hybrid PV power forecasting methods: a comparison of different approaches. *Energies* **14(2)**, 451 (2021).
- [12] R. Luo, B. Sun, X. Hou, W. Shi, G. Zhang, J. Fan, Optimal design of 100–2000 V 4H-SiC power MOSFETs using multi-objective particle swarm optimization algorithms. *IEEE Electron Device Lett.* (2024).
- [13] A. El Kissani, L. Nkhaili, A. Ammar, K. Ellassali, A. Outzourhit, Synthesis, annealing, characterization, and electronic properties of thin films of a quaternary semiconductor; copper zinc tin sulfide. *Spectrosc. Lett.* **49(5)**, 343–347 (2016).

- [14] L. Kong, R. Wu, Y. Chen, Y. Huangfu, L. Liu, W. Li, Y. Liu, Wafer-scale and universal van der Waals metal semiconductor contact. *Nat. Commun.* 14(1), 1014 (2023).
- [15] K. Zeghdar, L. Dehimi, F. Pezzimenti, M.L. Megherbi, F.G. Della Corte, Analysis of the electrical characteristics of Mo/4H-SiC schottky barrier diodes for temperature-sensing applications. *J. Electron. Mater.* 49(2), 1322–1329 (2020).
- [16] Y. Qi, N. Wei, Y. Li, D. Kou, W. Zhou, Z. Zhou, S. Wu, Passivating SnZn defect and optimizing energy level alignment via organic silicon salt incorporation toward efficient solution processed CZTSSe solar cells. *Adv. Func. Mater.* 34(12), 2308333 (2024).
- [17] K. Zeghdar, L. Dehimi, F. Pezzimenti, S. Rao, F.G. Della Corte, Simulation and analysis of the current–voltage–temperature characteristics of Al/Ti/4H-SiC Schottky barrier diodes. *Japanese J. Appl. Phys.* 58(1), 014002 (2019).
- [18] H. Bencherif, L. Dehimi, F. Pezzimenti, F.G. Della Corte, Improving the efficiency of a-Si:H/c-Si thin heterojunction solar cells by using both antireflection coating engineering and diffraction grating. *Optik* 182, 682–693 (2019).
- [19] A. Abbassi, R. Abbassi, A.A. Heidari, D. Oliva, H. Chen, A. Habib, M. Wang, Parameters identification of photovoltaic cell models using enhanced exploratory salp chains-based approach. *Energy* 198, 117333 (2020).
- [20] T.C. Lee, S. Fung, C.D. Beling, H.L. Au, A systematic approach to the measurement of ideality factor, series resistance, and barrier height for schottky diodes. *J. Appl. Phys.* 72(10), 4739–4742 (1992).
- [21] K. Karimi, R. Teimouri, A. Mahjoory, M. Kolahdouz, S. Mehrvarz, R. Mohammadpour, Z. Sanaee, Stability assessment of a planar perovskite solar cell: estimating parasitic resistances using a new method. *Sol. Energy* 271, 112335 (2024).
- [22] M.A. Abdi, H. Bencherif, T. Bendib, F. Meddour, M. Chahdi, Significant improvement of infrared graphene nanoribbon phototransistor performance: a quantum simulation study. *Sens. Actuators A* 317, 112446 (2021).
- [23] M. Gen, L. Lin, Genetic algorithms and their applications, in *Springer handbook of engineering statistics*. (Springer, London, London, 2023), pp.635–674.
- [24] M.A. Navarro, D. Oliva, A. Ramos-Michel, E.H. Haro, An analysis on the performance of metaheuristic algorithms for the estimation of parameters in solar cell models. *Energy Convers. Manage.* 276, 116523 (2023).
- [25] F. Pezzimenti, H. Bencherif, A. Yousfi, L. Dehimi, Current voltage analytical model and multiobjective optimization of design of a short channel gate-all-around-junctionless MOSFET. *Solid State Electron.* 161, 107642 (2019).
- [26] H. Bencherif, A. Yousfi, M. Khouani, A. Meddour, Z. Kourdi, (2021) “Boosted Graphene/SiC MSM Photodetector Performance Using Genetic Algorithm Approach and Embedded Plasmonic Nanoparticles”, In *International Conference on Artificial Intelligence in Renewable Energetic Systems*, Springer, Cham, 753–762.

- [27] K. Yang, J. Zheng, J. Zou, F. Yu, S. Yang, A dual-population evolutionary algorithm based on adaptive constraint strength for constrained multi-objective optimization. *Swarm Evol. Comput.* 77, 101247 (2023).
- [28] Q. Long, C. Wu, T. Huang, X. Wang, A genetic algorithm for unconstrained multi-objective optimization. *Swarm Evol. Comput.* 22, 1-14 (2015).
- [29] J. Appelbaum, A. Peled, Parameters extraction of solar cells – A comparative examination of three methods, *Solar Energy Materials and Solar Cells*, Volume 122,164-173 (2014)

General Conclusion

The kesterite-based solar cell is an emerging and promising photovoltaic technology that could potentially enable the production of low-cost, high-volume thin-film solar cells. Having undergone rapid development over the past few decades, this technology has garnered increasing attention and demonstrated significant potential for high efficiency. CZTS possesses a narrowly stable region concerning chemical potential, making the formation of secondary phases quite easy. The formation of these secondary phases can lead to significantly increased resistance; shunt resistance depends on the bandgap of the phase, which will also limit device performance. Additionally, the heterojunction interface could contribute to performance losses due to unfavorable band alignment or detrimental reactions during high-temperature annealing.

In our work, we focused on two aspects: a purely theoretical aspect based on numerical calculations using the SCAPS-1D software for proposed standard solar structure devices, and an experimental aspect concerning the development of the Al/p-CZTS Thin Film Schottky Diodes the spin-coating technique on soda lime glass substrates, followed by appropriate structural, electrical characterization and parameter extraction of the $\text{Cu}_2\text{ZnSnS}_4$ (CZTS) Thin film.

Initially, our work focused on simulating the use of hole transport layers (HTLs), specifically MoO_x and CuI , in combination with SnS , to greatly improve the efficiency of CZTS-based solar cells. In our investigation, we went beyond the usual limits by carefully adjusting important cell characteristics, including the thickness of the CZTS absorber layer, the density of defects, and the concentration of acceptors. The implementation of these hole transport layers (HTLs) resulted in two distinct benefits: an increase in the absorption of photon energy and a significant decrease in recombination rates. MoO_x and CuI demonstrated superior performance as hole transport layers (HTLs), surpassing SnS by a significant margin. The superiority was demonstrated by achieving an amazing power conversion efficiency of 23.73% and an exceptional fill factor of 88%. These impressive results precisely correspond to the theoretical limits established by Shockley-Queisser, which further enhances the fascination of our discoveries. This discovery not only indicates the potential to improve the effectiveness of CZTS hetero-junction based solar cells, but also introduces the possibility of a more environmentally friendly and efficient age in converting solar energy. This significant

advancement shows potential for practical implementation in renewable energy technology, leading to a more optimistic and environmentally friendly future.

In the second phase of our experimental work, we employed the spin coating technique to deposit the CZTS thin film, thereby eliminating the need for subsequent sulfurization. Comprehensive structural analysis clearly confirmed the presence of the characteristic Kesterite CZTS phase. Notably, the SEM micrograph of the CZTS sample revealed a surface that was both dense and compact. Shifting our focus to electronic properties, the I–V characteristic analysis of the Al/p-CZTS/Mo junction indicated the formation of a Schottky diode. In the realm of electronic characterization, we extracted key parameters such as the ideality factor, saturation current, series resistance, and shunt resistance using two distinct methods. The parameters obtained through these different approaches showed impressive agreement, further validating the robustness and reliability of our results.

The results obtained through this dissertation also encourage us to carry out additional investigations in the field of CZTS solar cells. For example, we aim to explore other phenomena that may impact the performance of these devices, necessitating the development of alternative models and approaches.

A.1 Genetic algorithms

Genetic algorithms are one of the most used optimization methods. They represent a branch of the field of research called evolutionary computation [1]. They make it possible to determine the maximum or minimum values of a given function. They mimic the biological processes of reproduction and natural selection to find solutions to a given problem [1]. Many processes of a genetic algorithm are random. However, this optimization technique makes it possible to set the level of probability and the level of control [1]. These algorithms are much more powerful and efficient than random search and exhaustive search algorithms [1], but do not require additional information about the given problem. This feature allows them to find solutions to problems that other optimization methods cannot handle due to lack of continuity, derivatives, linearity, or other features.

In what follows, we will give the basic elements of a genetic algorithm. The specific parts of the genetic algorithm that have a particular function are called operators. In its simplest form, a genetic algorithm is composed of three basic operators:

- Selection
- Crossover
- Mutation

In addition to these basic operators, the generation operator creates the chromosome population. In addition, the elitism operator is used to prevent the loss of successful individual chromosomes. These operators are applied to the current generation to form the next generation. The genetic algorithm continues to evolve until the design criteria are met. These criteria are defined by the user at the very beginning of the optimization.

Figure 1 presents the basic fundamentals of the genetic algorithm. In the beginning, the population is evaluated and their physical condition is determined. Then successful individuals are selected and they replace those who fail. The next step is to train the next population using elitism, crossover and mutation. These processes continue until the predefined population number is reached [1].

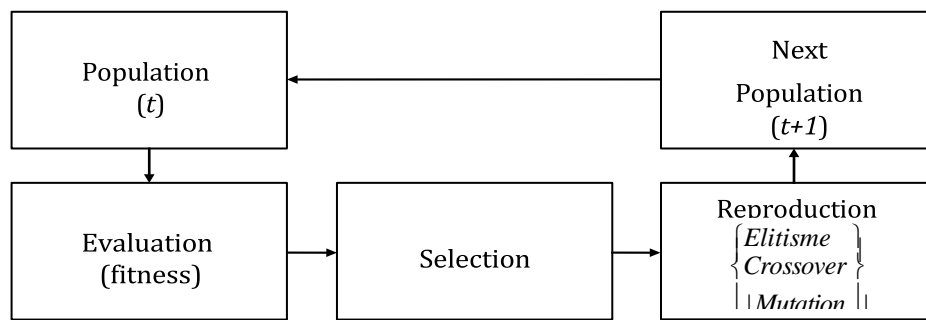


Figure A.1. Simple flow chart of the genetic algorithm

A.1.1. Chromosome concept

The genetic algorithm uses the concept of chromosome to define the variables. Each decision variable is defined in genes to form chromosomes. The common means of coding is a binary string..

A.1.2. Generation

Based on the data we have, the genetic algorithm will generate an initial population. Each population is composed of chromosomes. Each solution (chromosome) will contain decision variables generated randomly. The random number generator assigns a 1 or a 0 to each bit position in the chromosome where the defined number of bits represents specific decision variables. This operator is called the "Generation" operator.

Once the initial population is generated, the genetic algorithm will translate each gene into the corresponding variable and calculate the objective function. Once the objective function is reached, an analysis must be carried out for each chromosome of the population [2].

A.1.3. Selection

This operator is used to eliminate the worst chromosomes because of their low fitness. Once their objective functions are determined at an earlier stage, a number of chromosomes with the worst fitness are replaced by the same number of better chromosomes [2].

A.1.4. Elitism

Elitism is used to protect the most suitable chromosomes of crossbreeding and mutation. The goal is to have some of the best chromosomes best suited in the next generation and not lose them. Elitism can quickly increase the performance of the genetic algorithm [2].

A.1.5. Crossover

The crossing operator is applied to initiate a partial exchange of bits (information) between the parent strings to form two descendants. The genetic algorithm will randomly choose two solutions for crossing.

The crossover rate is defined by the user at the beginning of the study. The most popular crossover types are single-point, two-point and multi-point crossings as shown in Figure 2. Note that all crosspoints are randomly selected [2].

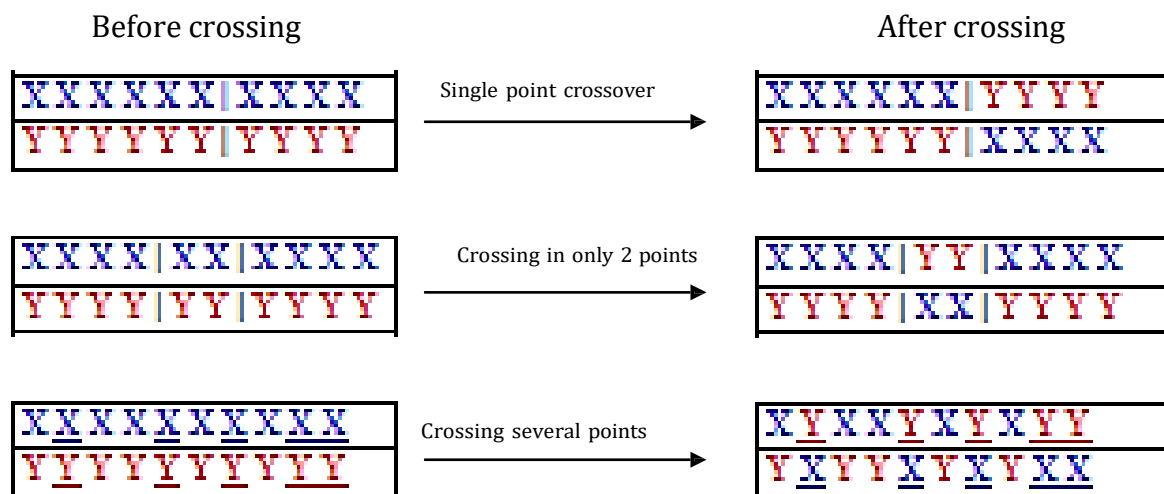


Figure A.2. Crossover Operator

A.1.6. Mutation

Once the moment of application of the mutation is known, the mutation operator simply randomly changes the value of a gene. For real genes, this change could be done by selecting a number evenly across the range of possible values. Another possibility is to use a zero mean Gaussian distribution with a given variance where the number generated by this distribution is added to the value of the gene. This could be adjusted so that the variance decreases as the algorithm iterates [2].

A.2 Implementation of a genetic algorithm

Genetic algorithm follows the following steps [2]:

- Step 1 :** Define the number of chromosomes, generation, mutation and crossover rates.
- Step 2 :** Generate a number of population and initialize the value of the genes with a random number.
- Step 3 :** Done steps 4 to 7 until the generation number is reached.
- Step 4 :** Evaluation of the fitness value of chromosomes by calculating the objective function.
- Step 5 :** Evaluation of the fitness value of chromosomes by calculating the objective function.
- Step 6 :** Crossover
- Step 7 :** Mutation
- Step 8 :** Solution (best chromosome)

The flowchart of a genetic algorithm is shown below.

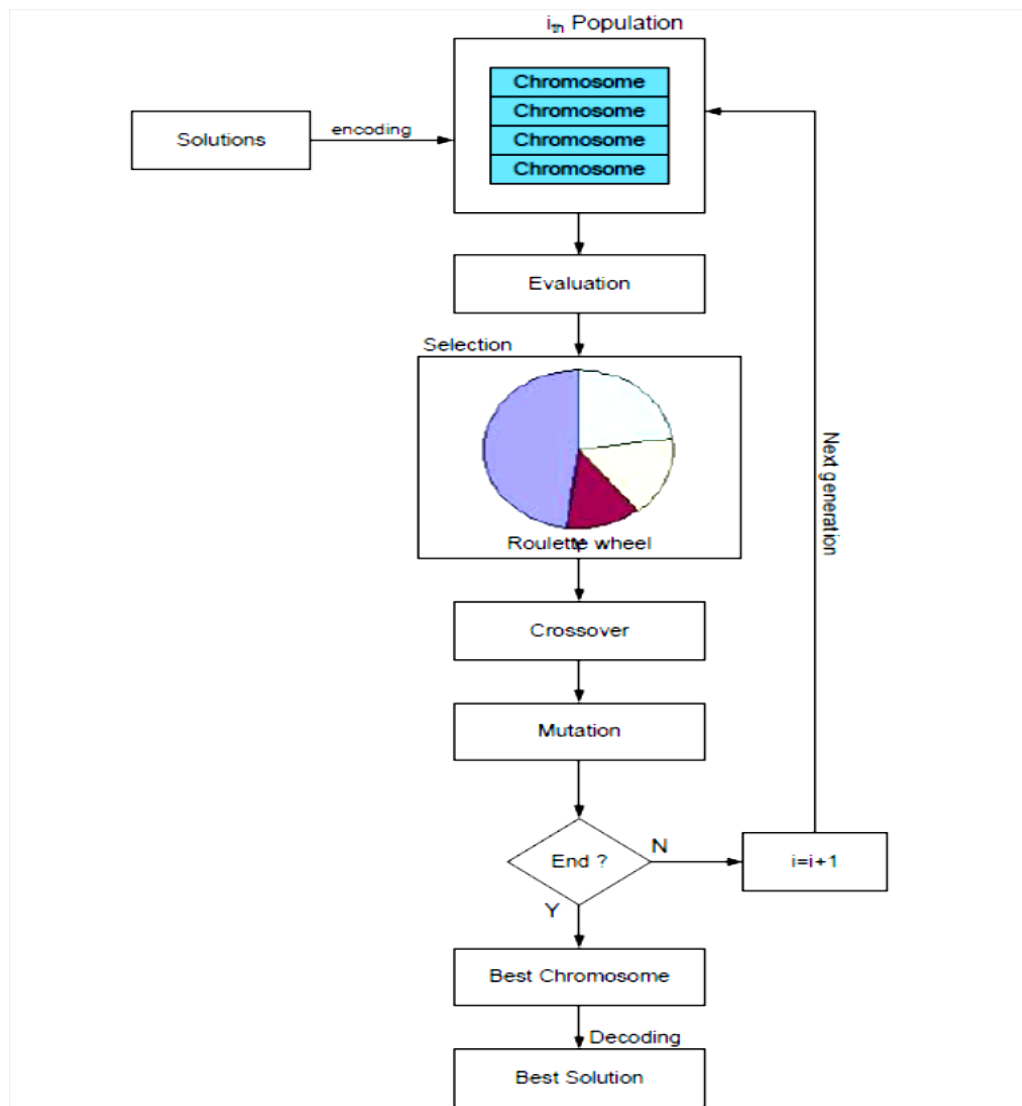


Figure A.3. Flowchart of a genetic algorithm

A.3.2 Conclusion

Genetic algorithms provide solutions close to the optimal solution using selection, hybridization and mutation mechanisms. A genetic algorithm gives us great freedom in the setting and implementation of different treatments. We are then free to modify a particular parameter if the solutions obtained do not suit us.

References

- [1] M. Gen, R. Cheng, "Genetic Algorithms And Engineering Design", John Wiley & Sons, 1997.
- [2] M. Gen, R. Cheng, L. Lin "Network Models and Optimization: Multiobjective Genetic Algorithm Approach", Springer-Verlag London editions, 2008.

Newton-Raphson Method of Solving a Nonlinear Equation

B.1 Introduction

Methods such as the bisection method and the false position method of finding roots of a nonlinear equation $f(x) = 0$ require bracketing of the root by two guesses. Such methods are called bracketing methods. These methods are always convergent since they are based on reducing the interval between the two guesses so as to zero in on the root of the equation.

In the Newton-Raphson method, the root is not bracketed. In fact, only one initial guess of the root is needed to get the iterative process started to find the root of an equation. The method hence falls in the category of open methods. Convergence in open methods is not guaranteed but if the method does converge, it does so much faster than the bracketing methods.

B.2 Derivation

The Newton-Raphson method is based on the principle that if the initial guess of the root of $f(x)=0$ is at x_i , then if one draws the tangent to the curve at $f(x_i)$, the point x_{i+1} where the tangent crosses the x -axis is an improved estimate of the root (Figure 1).

Using the definition of the slope of a function, at $x = x_i$.

$$f'(x_i) = \tan \theta$$

$$= \frac{f(x_i) - 0}{x_i - x_{i-1}}$$

Which gives
$$x_{i+1} = x_i - \frac{f(x_i)}{f'(x_i)} \quad (1)$$

Equation (1) is called the Newton-Raphson formula for solving nonlinear equations of the form $f(x)=0$. So starting with an initial guess, x_i , one can find the next guess, x_{i+1} , by using Equation (1). One can repeat this process until one finds the root within a desirable tolerance.

Algorithm

The steps of the Newton-Raphson method to find the root of an equation $f(x) = 0$ are

1. Evaluate $f'(x) = 0$ symbolically
2. Use an initial guess of the root, x_i , to estimate the new value of the root, x_{i+1} , as

$$x_{i+1} = x_i - \frac{f(x_i)}{f'(x_i)}$$

3. Find the absolute relative approximate error $|\epsilon_a|$ as

$$|\epsilon_a| = \left| \frac{x_{i+1} - x_i}{x_{i+1}} \right| \times 100$$

4. Compare the absolute relative approximate error with the pre-specified relative error tolerance, ϵ_s . If $|\epsilon_a| > \epsilon_s$, then go to Step 2, else stop the algorithm. Also, check if the number of iterations has exceeded the maximum number of iterations allowed. If so, one needs to terminate the algorithm and notify the user.

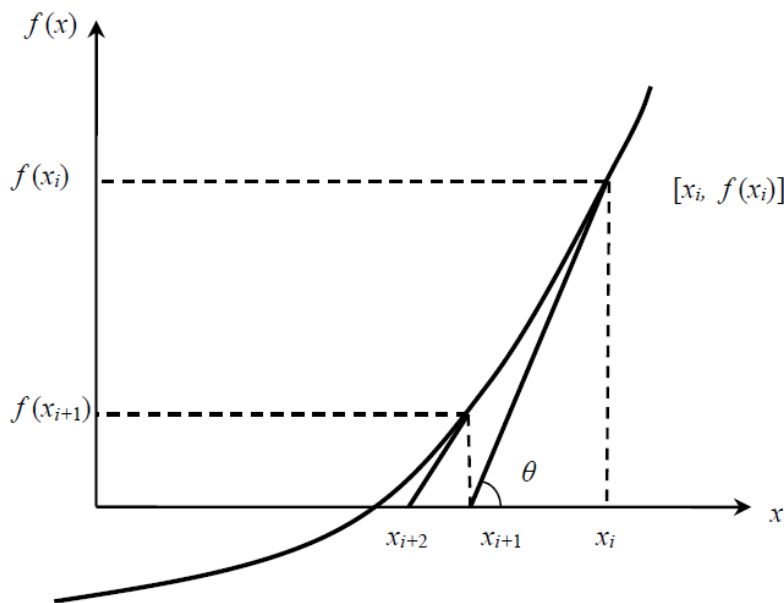


Figure 1 Geometrical illustration of the Newton-Raphson method.

Publication and conferences

- Mansouri, Siham, Lakhdar Dehimi, Hichem Bencherif, et al . Theoretical Simulation on Enhancing the Thin-Film Copper Zinc Tin Sulfide Solar Cell Performance Using MoS₂, MoO_x, and CuI as Efficient Hole Transport Layers. *Energy & Fuels* 38, n° 9 (2 mai 2024): 8187-98.
- Mansouri, S., Belgacem, H., Dehimi, L. *et al.* Unveiling the structural and electrical features of Al/p-CZTS thin film schottky structure for photovoltaic application: a comparative parameter extraction study. *Appl. Phys. A* **130**, 670 (2024).
- Siham Mansouri, Hocine Belgacem, Lakhder Dehimi. Kesterite thin film solar cell parameters extraction from dark I-V characteristic, Second International Conference on Electrical Engineering ICEEB'2018, December 2-3 2018, Biskra, Algeria.
- Siham Mansouri, Lakhder Dehimi, Zeghdar Kamal. Enhancing Efficiency in CZTS Solar Cells: A Study on Material Integration and Layer Optimization. *1st* International Conference on Technological Applications of Materials (ICTAM'24), October 30-31 2024, Sétif, Algeria.